AN ABSTRACT OF THE DISSERTATION OF

Tristan DeBorde for the degree of Doctor of Philosophy in Physics presented on January 23, 2014.

Title: Scanning Photocurrent Microscopy Study of Photovoltaic and Thermoelectric Effects in Individual Single-Walled Carbon Nanotubes

Abstract approved: ______________________________

Ethan D. Minot

Carbon Nanotubes are a unique family of nanostructures that have shown remarkable promise for mechanical, electrical, and optical applications. Fundamentally similar to the earlier discovered Buckminsterfullerene (C_{60}), carbon nanotubes are hollow cylinders formed from a single sheet of carbon atoms. The research presented in this dissertation investigates several carbon nanotube properties, with an emphasis on the interactions between light and electrons within the nanotube. Better understanding of these optoelectronic properties is of great interest for future advancement in solar energy conversion.

Carbon nanotubes are a quintessential material for researchers studying nanoscience. Small changes in nanotube structure can lead to striking differences in electrical and optical properties. In addition to this rich variety of properties, nanotubes can be concentrically inset within one another resulting in single-walled, double-walled, and multi-walled versions. Single-walled carbon nanotubes are desirable for optoelectronic study as complicated interactions between shells are avoided; which, while an interesting topic, is beyond the scope of this work. In the past, determination of carbon nanotube wall number was achieved via transmission electron microscopy, a technique requiring difficult sample preparation, making it impractical for most working devices. This thesis

presents an alternative technique based on the compressibility of nanotube sidewalls as measured by atomic force microscopy. This technique is readily applicable to common device designs and can distinguish single and double-walled carbon nanotubes. This technique has been applied to characterizing the output of our growth process, resulting in recipes that highly favor single-walled growth.

The optical properties of single-walled carbon nanotubes have been studied intensely. Each single-walled nanotube has an optical fingerprint based on its unique atomic structure. Specific single-walled nanotube structures can be selected for a wide range of optical applications. Again, however, most techniques previously used to study these optical properties are not easily transferable to common device designs. In this research, the measurement of nanotube fingerprints is achieved by optoelectronic means through the use of a newly constructed scanning photocurrent microscope. This instrument measures changes in electrical transport as the device is locally illuminated by a spectrally-tunable light source, making it a versatile tool for studying nanostructures implemented in a variety device designs.

Early work on nanotube optoelectronic properties attributed photocurrent generation to a photovoltaic mechanism. This thesis, however, shows that strong photothermoelectric effects can also be present in nanotube optoelectronic devices. Light absorbed by a nanostructure can locally raise the temperature, resulting in thermoelectric currents. If a carbon nanotube is being employed as the absorbing element of a solar cell, it is possible for thermoelectric currents to reduce or enhance the efficiency of energy conversion. The last portion of this work investigates the nature of optically generated thermoelectric effects in carbon nanotubes. With a better understanding of these thermoelectric effects, future nanostructure solar cell design can efficiently utilize thermoelectric currents.

Scanning Photocurrent Microscopy Study of Photovoltaic and Thermoelectric Effects in Individual Single-Walled Carbon Nanotubes

by
Tristan DeBorde

A DISSERTATION

submitted to

Oregon State University

in partial fulfillment of
the requirements for the
degree of

Doctor of Philosophy

Presented January 23, 2014
Commencement June 2014

Doctor of Philosophy dissertation of Tristan DeBorde presented on January 23, 2014

APPROVED:

Major Professor, representing Physics

Chair of the Department of Physics

Dean of the Graduate School

I understand that my dissertation will become part of the permanent collection of Oregon State University libraries. My signature below authorizes release of my dissertation to any reader upon request.

Tristan DeBorde, Author

ACKNOWLEDGEMENTS

The fact that I'm even able to write this document is due to the incredible people I've had the good fortune to call my colleagues, friends, and family. I would like to acknowledge my research advisor Ethan Minot, whose unfaltering support and scientific insight have inspired and guided me all these years. My lab mates have been steadfast friends; Matt, Landon, Josh, Tal and all the other Minot group members I've been lucky enough to work with, thank you for all the good times. Nic, Whitney, Mark and all my other friends in the department, thank you for always having time to help me over the years. To Oksana, thank you for being an incredible teacher and a source of inspiration. The physics department as a whole, Henri, Paula, Jim, Janice, and everyone else, thank you.

I would like to acknowledge the people I've met through the Owen clean room. John Wager who lets us use his equipment, Chris Tasker and Rick Presley who keep all the equipment running smoothly and safely, and all the graduate students who always have time to help and talk about fabrication, Ram, Bill, Sean, Nasir, Wei Wang, and Weiyang.

I would like thank the nurses and doctors who helped me through the last few years. Dr. K, Holly, Jeanette, Paula, Diana, and everyone else. Looking back it seems impossible I should have met so many wonderful people who showed me such kindness when I needed it most.

Finally, thank you to all the family members who have always been supportive of me; my family in Rhode Island, my family in Missoula, and Bob and DeeDee who have always looked out for me and believed in me. Thank you to my parents, Dan and Kala, and my sister, Jillian; everything I've been able to accomplish is due to your love and support. Thank you for dropping everything and coming to my rescue, I wouldn't be here without you.

CONTRIBUTION OF AUTHORS

Matthew Leyden assisted with atomic force microscopy measurements in Chapter 2. Caleb Joiner helped with Mat Lab modeling of carbon nanotube compression in Chapter 2. Josh Kevek and Tal Sharf fabricated devices for the research in Chapters 3, 4 and 5. Jenna Wardini assisted with the data analysis of photocurrent images in Chapter 3. Lee Aspitarte assisted with photocurrent measurements in Chapters 4 and 5. Ethan Minot contributed to all aspects of this work

TABLE OF CONTENTS

TABLE OF CONTENTS (Continued)

TABLE OF CONTENTS (Continued)

LIST OF FIGURES

LIST OF FIGURES (Continued)

LIST OF FIGURES (Continued)

LIST OF TABLES

PREFACE

I had the good fortune to start my graduate research in the summer before my first year of classes here at Oregon State University. Being part of a brand new lab has been a unique experience in which my research has grown hand-in-hand with the lab itself. The work presented in this dissertation is focused on carbon nanotubes (CNTs) and is divided into two primary methods of investigation, atomic force microscopy (AFM) and scanning photocurrent microscopy (SPCM). Between these two projects is a break in my graduate career stemming from being diagnosed with Acute Lymphoblastic Leukemia during my second year. With a phenomenal amount of luck combined with the support from friends, family, and the Physics department, I'm able to look back on that time and casually describe it here as an intermission between research projects.

In my first research project I studied the radial compression of CNTs as a function of the force applied by an AFM tip. The experimental method in this work allowed us to distinguish single-walled and double-walled CNTs for the first time with an AFM. The main results of this work were published in the journal *Nano Letters*. During this time I was also learning chemical vapor deposition (CVD) growth of CNTs and photolithography fabrication techniques to make CNT based nanoelectronic devices. It was at this point in time, when I was about to begin working on the SPCM project, that I was diagnosed with Leukemia.

After almost a year of treatment I was able to return to school and continue researching while completing two more years of chemotherapy. The research in this second segment switched focus to the optoelectronic properties of CNTs. As a result of the one-dimensional nature of CNTs, electrons undergo strong coulomb interactions with one another. This leads to unique electron-electron interactions including efficient multiple electron-hole pair generation which could be beneficial for future CNT based solar cell applications. My project was to study CNT optoelectronic devices with a recently developed technique known as scanning photocurrent microscopy (SPCM). The construction of this instrument and basic operation was the first milestone for the project and was published as a conference proceeding for the 11th IEEE International Conference on Nanotechnology.

One specific goal of the project was to measure the unique absorption resonances of individual CNTs using SPCM. This proved to be a difficult measurement that required very clean and stable CNT devices. The fabrication of these devices was carried at the Cornell NanoScale Science & Technology Facility by Josh Kevek and Tal Sharf. From these devices, SPCM is able to identify multiple photoconductivity resonances from a device making it possible to match the CNT to a known chirality. The results of this work are in the process of being submitted to be published.

Photo-responses measured with the SPCM are not limited to direct absorption by the nanostructure in a device. A prime example of this type of extraneous photo-response originates from laser-heating of the metal contacting the CNTs in our devices. Using polarization dependent imaging we were able to isolate photocurrents caused by metal heating from those due to CNT absorption. We were also able for the first time to identify a regime where an individual CNT photo-response was dominated by thermoelectric effects rather than photovoltaic effects. These results were published in the journal *ACS Nano*.

The SPCM research reported in this dissertation has all been done in ambient conditions however I have worked on upgrading the scanning photocurrent microscope to take measurements in vacuum at cryogenic temperatures. The research being done with the microscope now by Lee Aspitarte is moving in a very exciting direction, probing the strong electron-electron interactions in individual CNTs and how those interactions change when the CNT is placed in a dielectric environment.

Tristan DeBorde
January 23th, 2014
Corvallis, Oregon

Scanning Photocurrent Microscopy Study of Photovoltaic and Thermoelectric Effects in Individual Single-Walled Carbon Nanotubes

CHAPTER 1

Introduction

1.1 Introduction

Nanotechnology is a diverse field of research with an inspirational foundation that dates back to 1959 when Richard Feynman gave his famous lecture, “There’s Plenty of Room at the Bottom.” The diversity of the field stems from the fascinating rules that govern nature “at the bottom,” which impact all scientific disciplines. From biology to electronics, learning how materials behave and interact at the nanoscale is reshaping our approaches to solving everyday problems.

Carbon-based nanomaterials have been at the forefront of nanotechnology in multiple different forms. Buckminster fullerenes, nanotubes, and graphene have been the subjects of intense scientific study due to their unique properties and potential for future applications. Carbon nanotubes (CNTs) are a family of structures where slightly different arrangements of the carbon atoms can lead to stark differences in resulting properties.[1] One such difference is how the CNT conducts electricity. Based upon their structure, one-third of all CNTs will be metallic while the rest will be semiconducting.[2] Nanometer-sized CNTs with a tunable conductance have drawn interest for applications as transistors, single-molecule sensors, and photovoltaic devices.[3,4]

The work presented here is the first part of an ongoing project with the goal of furthering our understanding of CNT optoelectronic properties to the point of enabling design of high-efficiency CNT based photovoltaic cells. Conventional solar cells made from bulk semiconductors are limited to a one-to-one electron per photon conversion.[5] In CNTs, energy relaxation pathways can increase the number of free carriers created per single photon, breaking the efficiency limits imposed on bulk semiconductors.[6-8] The research in the following chapters represents some of the necessary steps along the path toward this goal: mechanical identification of single-walled CNTs, creation of a tool for the optoelectronic study of CNTs, characterization of the spectral dependence of pristine CNTs, and a deeper understanding of CNT photo-response mechanisms.

1.2 Atomic Force Microscopy

Studying CNTs is inherently challenging as they are too small to be directly imaged with traditional optical microscopy. One alternative is atomic force microscopy (AFM), a mechanically based imaging technique. In AFM, a sharp tip attached to a cantilever is raster scanned across a sample, feeling the surface. The tip can be dragged across it as in “contact mode imaging,” or oscillated at a high frequency in “tapping mode,” which is used in chapter 1. Figure 1.1 shows a schematic of tapping mode AFM. To track how the tip interacts with the surface, a laser reflected from the top of the cantilever is monitored in a four quadrant photodetector which can detect small movements in the laser’s position and hence the deflection of the cantilever. The changing deflection information, is used to maintain a constant amplitude of oscillation by raising or lowering the cantilever with a precise z-piezo. Combined with the raster scanning of the sample by an underlying x-y piezo stage, the AFM can generate an image of the sample topography.

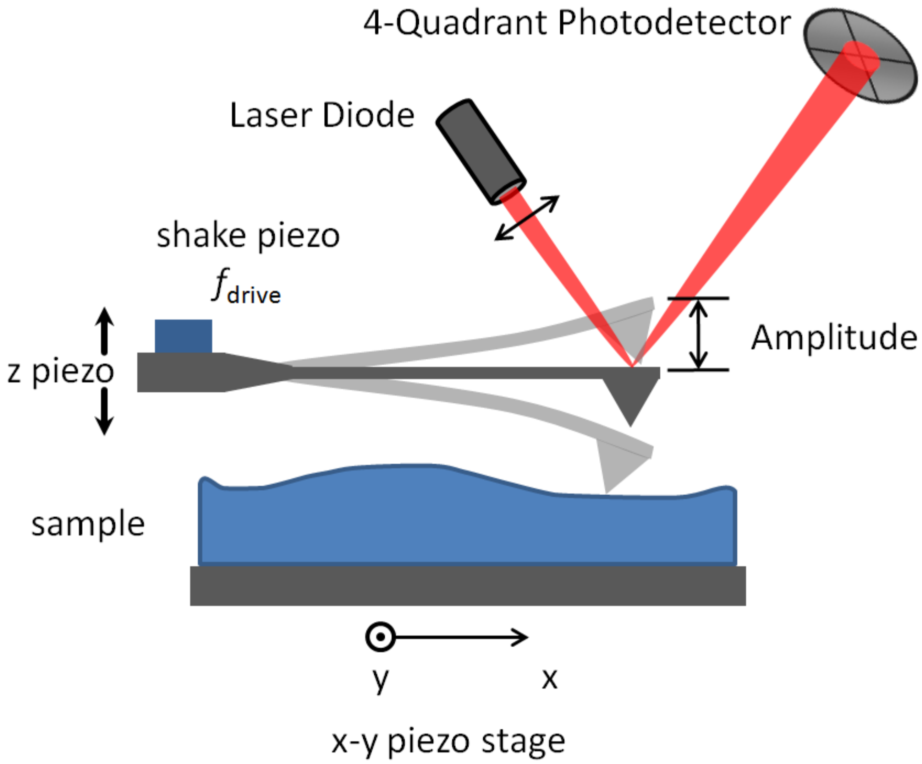

Figure 1.1. Schematic of AFM operating in tapping mode. Piezoelectric scanners control the x-y position of the sample, cantilever z height, and tip oscillation (frequency and amplitude). Reflected laser light from the AFM tip is monitored by a 4-quadrant photodetector.

The mechanical nature of AFM allows for a level of direct interaction with nanostructures that is not possible with other nanoscale imaging techniques such as scanning electron microscopy (SEM) or transmission electron microscopy (TEM). The work in Chapter 1 uses an AFM tip to measure CNT compression as a function of the force applied by the tip. This compression information is applied to tapping mode imaging to discern single and double-walled CNTs. The ability to distinguish CNTs with different numbers of concentric shells provides feedback for tuning growth processes to favor single-walled CNTs.

1.3 Scanning Photocurrent Microscopy of CNTs

While individual CNTs have a very small optical absorption cross-section, the optoelectronic properties are, none-the-less, very interesting. The one dimensional nature of CNTs leads to strong absorption resonances at certain electronic transitions.[9] As a consequence, a handful of techniques have been developed to probe CNTs using visible light. Most of these techniques are purely optical in nature, where CNT samples are illuminated with light and the resulting scattered/emitted light is measured. Important examples are resonant Raman scattering, fluorescence, and Rayleigh scattering.[10-12] These techniques can be difficult to implement for typical CNT device designs and only provide an indirect picture of electron transport properties.

To directly probe the optoelectronic properties of CNT devices, a relatively new technique has been developed known as scanning photocurrent microscopy (SPCM). This technique tracks changes in electron transport through the CNT while devices are illuminated by a focused laser spot. Raster scanning the laser spot generates a spatial map of the photo-response of the CNT device. These images can reveal information about the band bending near the metallic contacts and along the length of the CNT.[13-16] Additionally, this technique can reveal peaks in the photoconductivity as the wavelength is tuned across absorption resonances.[17,18] As an experimental technique, SPCM has proved useful for multiple nanomaterials including silicon nanowires, CNTs, graphene, and few layer molybdenum disulfide.[19-22]

The first photocurrent experiments investigated the photoresponse of CNT based field-effect transistors (FETs). In 2003 Freitag et al. made the first photoconductivity measurements of absorption resonances in individual SWNTs.[17] The first scanning photocurrent imaging was performed by Balasubramanian et al. in 2004, who reported localized photoresponse near the CNT-electrode junction.[20] More recently, SPCM was used to measure multiple electron-hole pair generation in CNT pn junctions.[7] Carrier multiplication could play key role in future high-efficiency solar cells and has been observed in other nanoscale materials including zero-dimensional quantum dots and two-dimensional graphene.[23,24] CNTs offer an ideal platform for studying the multiplication process which stems from strong electron-electron interactions.[6]

Beyond photovoltaic effects, SPCM has been used to indentify laser-induced thermoelectric effects in CNT films, graphene, and few-layer molybdenum disulfide.[21,22,25,26] This photothermoelectric mechanism originates from laser driven temperature gradients established along the nanostructure device. It has been difficult to differentiate photovoltaic and photothermoelectric effects in these systems due to the fact that the different photo-responses often have the same sign. In graphene p-n junctions it was definitively shown that the photothermoelectric effect is the dominant photoresponse mechanism.[26] For CNT film based devices there has been evidence for photothermoelectric effects. Results from individual single-walled CNT devices are reported in Chapter 5.

1.4 CNT Band Structure and Optoelectronic properties

As the physical structure of the CNT is a variation of graphene, so too is its band structure. First reported in 1947, the band structure of a single sheet of graphite has many unique properties including an effective zero-width band gap and a linear dispersion relationship near the Fermi level.[27] Graphene has generated significant attention due to this characteristic linear dispersion relationship which results in electrons and holes that behave as particles with zero effective mass.[28] In order to extrapolate from the graphene band structure to that of CNTs, the increased confinement of electrons must be considered.[2]

In graphene, the electrons are already confined to two dimensions due to the structure being a single sheet of atoms. When such a sheet is rolled into a cylinder, the constraint on the possible electron wave functions is increased.

Freedom remains for the electron wave vector up and down the axis of the tube ($k_{\|}$) but the wave vector along the circumference ($k_{\perp}$) is restricted to only certain values. This is seen as a periodic boundary condition on the electron wave function, where the relevant constraint comes from the diameter, d, of the CNT. Mathematically this constraint can be expressed as,

$$\mathbf{k}_{\perp} \cdot \mathbf{C} = k_{\perp}\pi d = 2\pi p, \quad (1.1)$$

where **C** is the chiral vector describing the circumference of the CNT and p is an integer.[2]

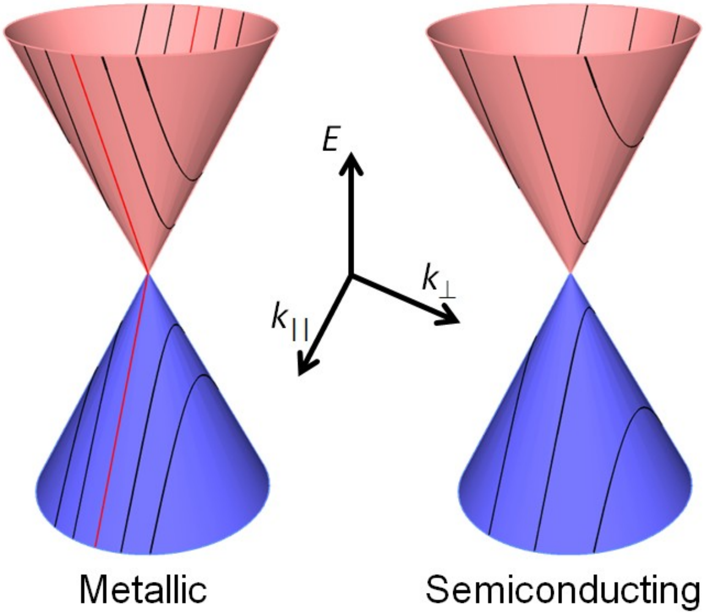

Figure 1.2. Diagram of a Dirac cone with projected cutting lines. Red and blue cones represent the conduction and valence bands of graphene, respectively. Metallic and semiconducting species are shown. The red cutting line in the metallic CNT passes directly through the Dirac point. The black lines represent the cutting lines of additional allowed values of $k_{\perp}$.

Starting from the two-dimensional band structure of graphene, $E(k_{\perp}, k_{||})$, the allowed values of $k_{\perp}$ can be envisioned as "cutting lines" (Figure 1.2).[29] Projected onto the graphene Dirac cone near the Fermi level, the allowed $k_{\perp}$ values result in a hyperbolic CNT band structure as a function of $k_{||}$. The indexed (i) conduction and valence (+ and -) bands for each cutting line are given by,

$$E(k_{||}) = \pm\sqrt{(\tfrac{1}{2}E_{g,i})^2 + (\hbar k_{||} v_F)^2}\,, \qquad (1.2)$$

where E_g is the energy separation between the intersection of $k_{\perp}$ with the upper and lower portions of the Dirac cone and v_F is the velocity of electrons in graphene, ~ 8×10^5 m/s.[30] Figure 1.3 shows the energy bands that result from the multiple cutting lines in Figure 1.2 as seen from the $k_{\perp}$ axis.

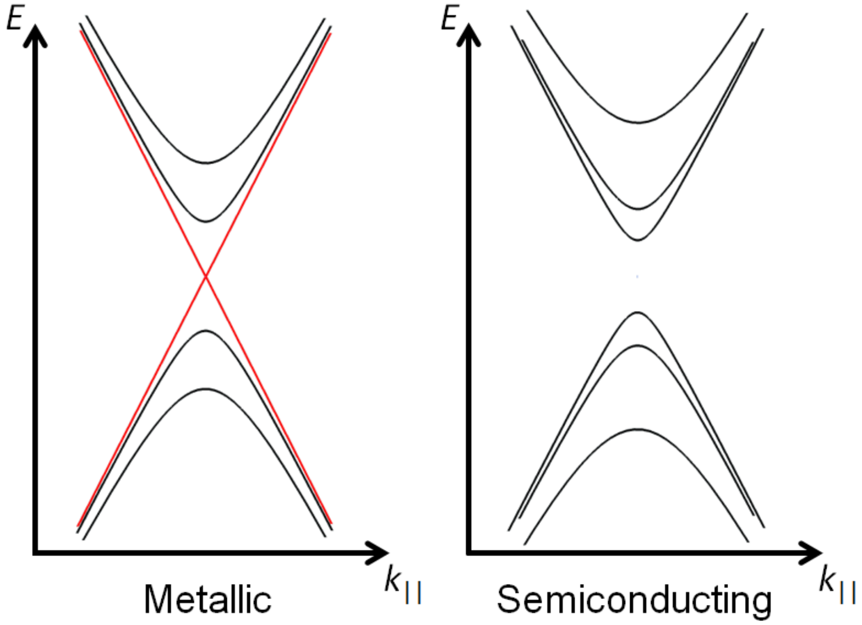

Figure 1.3. Schematic of hyperbolic CNT dispersion relationship. Graph shows the projected cutting lines from Figure 1.2 for both metallic and semiconducting CNT as a function of $k_{||}$. The cutting lines form the hyperbolic band structure described by Eq. 1.2.

The red zero-band-gap energy band in Figure 1.3 corresponds to a value of $k_\perp$ that passes directly through the Dirac point. In such an occurrence the resulting CNT is referred to as metallic. When this overlap between $k_\perp$ and the Dirac point does not occur, the CNT will have a non-zero bandgap and will be semiconducting. The underlying dependence of $k_\perp$ on the chiral vector means that the electronic properties of a given CNT are strongly structure dependent.[2]

Every single-walled CNT can be described by a chiral vector. Written in terms of graphene's primitive lattice vectors, the chiral vector defines how the CNT is rolled up from a sheet of graphene (Figure 1.4). Experimentally, indentifying a CNT's chiral vector has been accomplished with scanning tunneling microscopy or through optical measurements of CNT absorption, fluorescence, and scattering of light.[1,10,11]

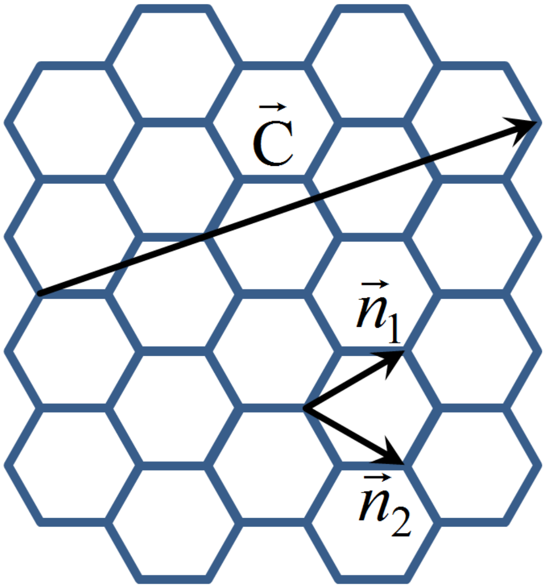

Figure 1.4. Diagram of carbon lattice with chiral vector and lattice vectors. The chiral vector **C** = (***n***$_1$, ***n***$_2$) shown is comprised of integer combinations of the lattice vectors ***n***$_1$ and ***n***$_2$. In this diagram, **C** = (4***n***$_1$, 1***n***$_2$).

Sharp resonant absorption features seen in optical measurements were first thought to stem from the one-dimensional density of states. Due to the inverse dependence on energy, one dimensional density of states diverges at the onset of each energy band. These spikes, also known as van Hove singularities were expected to cause narrow band-to-band transition widths.[9] This picture of optical transitions in CNTs predicts that absorption of a photon results in a free electron-hole pair. However, such transitions have not been observed. For a correct description, one must also consider the Coulomb interactions between carriers within the CNT.[31]

The electrons in CNTs experience significantly less electrostatic screening from the lattice compared to electrons in bulk materials. The resulting strong Coulomb interactions between charge carriers lead to tightly bound electron-hole pairs known as excitons.[32] The resonances in the CNT absorption spectrum were experimentally proven to be dominated by the formation of excitons rather than the creation of free electron-hole pairs.[31] Figure 1.5 shows a schematic of the differences between exciton absorption resonances (red trace) and band-to-band transitions (blue trace) recreated from Malic *et al.*[33] The strong Coulomb interactions and resulting exciton resonances raise a number of questions: what is the efficiency of photocurrent collection if exciton separation is necessary; how does strong electron-electron scattering affect energy relaxation pathways; and how does the CNT absorption spectrum depend on dielectric environment.

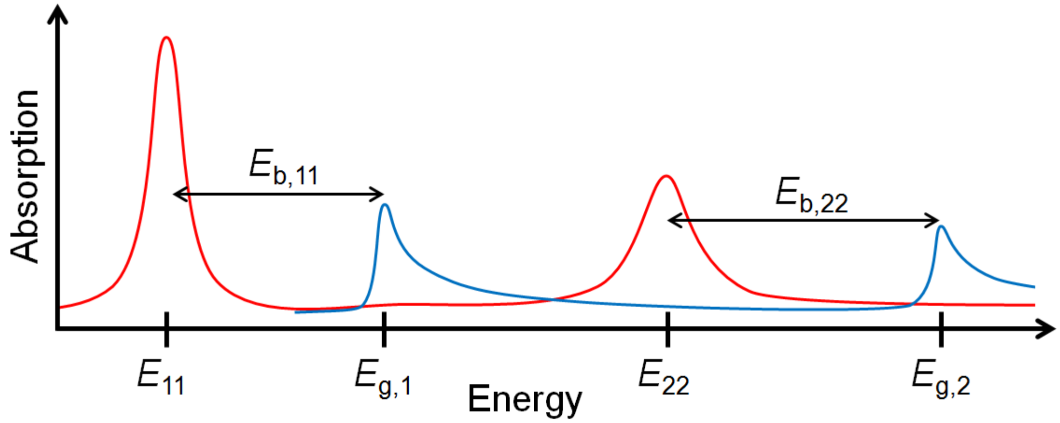

Figure 1.5. CNT absorption: exciton vs. free particles. Predicted absorption resonances calculated by Malic et al. for a (14,1) semiconducting CNT. Red line shows exciton absorption resonances (E_{ii}) calculated including Coulomb interactions. Blue line shows band-to-band absorption resonances ($E_{g,i}$) when electron-hole interactions are removed. The separation between the exciton (red) and band-edge (blue) peaks corresponds to exciton binding energy, $E_{b,ii}$.

Theoretical and experimental work is beginning to answer these questions. A recent experiment has observed spontaneous decay of excitons in CNTs and has measured photocurrent efficiency as a function of bias voltage.[34] Theoretical work has predicted energy relaxation pathways known as impact ionization and excitation to be efficient in CNTs due to strong coulomb interactions.[6] In a recent experiment, sudden steps in photocurrent are believed to be due to a carrier multiplication process such as impact ionization.[7] Measurements of CNT absorption resonances in different solvent environments have shown a small red shift in transition energy with increasing dielectric constant.[35] Much work is still needed to expand our understanding of CNT optoelectronic properties for use in next generation photovoltaic applications. The SPCM chapters in this dissertation build the foundations to begin experimentally revealing a deeper understanding of the optoelectronic processes in CNTs.

1.5 References

1 Wilder, J. W. G., Venema, L. C., Rinzler, A. G., Smalley, R. E. & Dekker, C. Electronic structure of atomically resolved carbon nanotubes. **391**, 59-62, doi:10.1038/34139 (1998).

2 Saito, R., Fujita, M., Dresselhaus, G. & Dresselhaus, M. S. Electronic structure of chiral graphene tubules. *Applied Physics Letters* **60**, 2204-, doi:10.1063/1.107080 (1992).

3 McEuen, P. L. & Fuhrer, M. S. Single-walled carbon nanotube electronics. *IEEE Transactions On Nanotechnology* **1**, 78-85, doi:10.1109/tnano.2002.1005429 (2002).

4 Avouris, P. & Chen, J. Nanotube electronics and optoelectronics. *Materials Today* **9**, 46-54 (2006).

5 Shockley, W. & Queisser, H. J. Detailed Balance Limit of Efficiency of p-n Junction Solar Cells. *Journal of Applied Physics* **32**, 510-, doi:10.1063/1.1736034 (1961).

6 Perebeinos, V. & Avouris, P. Impact excitation by hot carriers in carbon nanotubes. *Physical Review B* **74**, doi:Artn 121410 Doi 10.1103/Physrevb.74.121410 (2006).

7 Gabor, N. M., Zhong, Z., Bosnick, K., Park, J. & McEuen, P. L. Extremely efficient multiple electron-hole pair generation in carbon nanotube photodiodes. *Science (New York, N.Y.)* **325**, 1367-71, doi:10.1126/science.1176112 (2009).

8 Baer, R. & Rabani, E. Can Impact Excitation Explain Efficient Carrier Multiplication in Carbon Nanotube Photodiodes? *Nano Lett* **10**, 3277-82, doi:Doi 10.1021/Nl100639h (2010).

9 Kataura, H. *et al.* Optical properties of single-wall carbon nanotubes. *Synthetic Metals* **103**, 2555-8 (1999).

10 Jorio, a. *et al.* Structural (n, m) Determination of Isolated Single-Wall Carbon Nanotubes by Resonant Raman Scattering. *Physical Review Letters* **86**, 1118-21, doi:10.1103/PhysRevLett.86.1118 (2001).

11 Bachilo, S. M. *et al.* Structure-assigned optical spectra of single-walled carbon nanotubes. *Science* **298**, 2361-6, doi:DOI 10.1126/science.1078727 (2002).

12 Sfeir, M. Y. *et al.* Probing electronic transitions in individual carbon nanotubes by Rayleigh scattering. *Science (New York, N.Y.)* **306**, 1540-3, doi:10.1126/science.1103294 (2004).

13 Balasubramanian, K., Burghard, M., Kern, K., Scolari, M. & Mews, A. Photocurrent imaging of charge transport barriers in carbon nanotube devices. *Nano Lett* **5**, 507-10, doi:10.1021/nl050053k (2005).

14 Freitag, M. *et al.* Imaging of the schottky barriers and charge depletion in carbon nanotube transistors. *Nano Lett* **7**, 2037-42 (2007).

15 Freitag, M. *et al.* Scanning photovoltage microscopy of potential modulations in carbon nanotubes. *Applied Physics Letters* **91**, doi:Artn 031101 Doi 10.1063/1.2757100 (2007).

16 Ahn, Y. H., Tsen, A. W., Kim, B., Park, Y. W. & Park, J. Photocurrent imaging of p-n junctions in ambipolar carbon nanotube transistors. *Nano Lett* **7**, 3320-3 (2007).

17 Freitag, M., Martin, Y., Misewich, J. A., Martel, R. & Avouris, P. H. Photoconductivity of single carbon nanotubes. *Nano Lett* **3**, 1067-71, doi:Doi 10.1021/Nl034313e (2003).

18 Qiu, X. H., Freitag, M., Perebeinos, V. & Avouris, P. Photoconductivity spectra of single-carbon nanotubes: Implications on the nature of their excited states. *Nano Lett* **5**, 749-52, doi:Doi 10.1021/Nl050227y (2005).

19 Ahn, Y., Dunning, J. & Park, J. Scanning photocurrent imaging and electronic band studies in silicon nanowire field effect transistors. *Nano Lett* **5**, 1367-70 (2005).

20 Balasubramanian, K. *et al.* Photoelectronic transport imaging of individual semiconducting carbon nanotubes. *Appl Phys Lett* **84**, 2400-2 (2004).

21 Park, J., Ahn, Y. H. & Ruiz-Vargas, C. Imaging of photocurrent generation and collection in single-layer graphene. *Nano Lett* **9**, 1742-6, doi:10.1021/nl8029493 (2009).

22 Buscema, M. *et al.* Large and Tunable Photothermoelectric Effect in Single-Layer MoS2. *Nano Lett* **13**, 358-63 (2013).

23 Schaller, R. & Klimov, V. High Efficiency Carrier Multiplication in PbSe Nanocrystals: Implications for Solar Energy Conversion. *Physical Review Letters* **92**, 186601-, doi:10.1103/PhysRevLett.92.186601 (2004).

24 Tielrooij, K. J. *et al.* Photoexcitation cascade and multiple hot-carrier generation in graphene. *Nature Physics* **9**, 248-52, doi:10.1038/nphys2564 (2013).

25 St-Antoine, B. C., Menard, D. & Martel, R. Position Sensitive Photothermoelectric Effect in Suspended Single-Walled Carbon Nanotube Films. *Nano Lett* **9**, 3503-8, doi:Doi 10.1021/Nl901696j (2009).

26 Gabor, N. M. *et al.* Hot carrier-assisted intrinsic photoresponse in graphene. *Science (New York, N.Y.)* **334**, 648-52, doi:10.1126/science.1211384 (2011).

27 Wallace, P. The Band Theory of Graphite. *Physical Review* **71**, 622-34, doi:10.1103/PhysRev.71.622 (1947).

28 Charlier, J. C. E. P. C. Z. J. F. A. C. *Carbon Nanotubes*. Vol. 111 (Springer Berlin Heidelberg, 2008).

29 Samsonidze, G. G. *et al.* The Concept of Cutting Lines in Carbon Nanotube Science. *Journal of Nanoscience and Nanotechnology* **3**, 431-58, doi:10.1166/jnn.2003.231 (2003).

30 Saito, R., Dresselhaus, G. & Dresselahus, M. *Physical Properties of Carbon Nanotubes*. (1998).

31 Wang, F., Dukovic, G., Brus, L. E. & Heinz, T. F. The optical resonances in carbon nanotubes arise from excitons. *Science (New York, N.Y.)* **308**, 838-41, doi:10.1126/science.1110265 (2005).

32 Perebeinos, V., Tersoff, J. & Avouris, P. Scaling of excitons in carbon nanotubes. *Physical Review Letters* **92**, doi:Artn 257402 Doi 10.1103/Physrevlett.92.257402 (2004).

33 Pedrotti, F. L. & Pedrotti, L. S. *Introduction to optics*. 2nd edn, (Prentice Hall, 1993).

34 Kumamoto, Y. *et al.* Spontaneous exciton dissociation in carbon nanotubes. (2013).

35 Ohno, Y. *et al.* Excitonic transition energies in single-walled carbon nanotubes: Dependence on environmental dielectric constant. *Physica Status Solidi (B)* **244**, 4002-5, doi:10.1002/pssb.200776124 (2007).

CHAPTER 2

Identifying Individual Single-Walled and Double-Walled Carbon Nanotubes by Atomic Force Microscopy

T. DeBorde, J. C. Joiner, M. R. Leyden, and E. D. Minot

Nano Letters **8** (11), 2008

2.1 Introduction

The electronic and mechanical properties of carbon nanotubes (CNTs) depend on the number of concentric cylinders forming the CNT. The addition shells of a multiwalled nanotube, or neighboring tubes in a nanotube bundle, create parallel conduction paths and alter the electronic environment. Similarly, the radial compressibility of CNTs is affect by addition shells or bundling. Techniques to determine shell number or bundling, such as transmission electron microscopy, are often not compatible with experimental geometries for electrical and mechanical measurements. In such cases, researchers must rely on indirect evidence, such as the uncompressed height of a nanotube, to guess the exact shell structure.

Many authors have investigated stress-strain relationships of CNTs in the axial and radial directions;[1-6] however, these mechanical measurements have not demonstrated the resolution required to distinguish between single-walled nanotubes (SWNTs), double-walled nanotubes (DWNTs), and nanotube bundles. In this work we show that individual SWNTs and DWNTs have distinct mechanical signatures that are readily measured by atomic force microscopy (AFM). We have compared our measurements to a simple mechanical model that is based on theoretical predictions of the bending modulus of graphene.[7]

2.2 Methods

Carbon nanotubes were prepared on silicon substrates by either drop-casting commercially available CNTs (a mixture of DWNTs and SWNTs from Carbon Nanotechnologies Inc.) or by the chemical vapor deposition growth method.[8] Silicon AFM tips (Budget Sensors) with nominal spring constant $k = 40$ N/m and quality factor $Q \approx 400$ were characterized using the thermal amplitude method[9] and tip radius was found using $R_{\mathrm{tip}} = w^2/8h$ where w and h are the apparent width and height of a nanotube imaged by AFM. For ac-mode imaging the cantilever was driven close to resonance; the phase difference ϕ between cantilever motion and the driving piezo was 90 ± 5° before engaging with the sample.

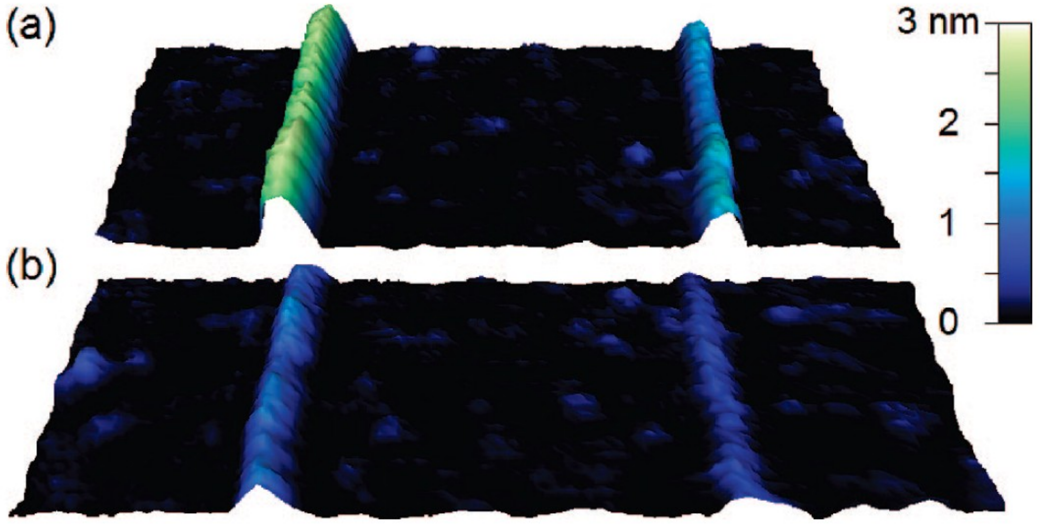

Figure 2.1. Gentle and aggressive AFM imaging of two CNTs. (a) Atomic force microscope image of two CVD grown nanotubes on a silicon substrate when energy transfer between tip and sample is small: A_{free} = 11.5 nm, A_{setpoint} = 10.6 nm, ϕ = 116° ($E_{\text{tap}} \sim 1$ eV). (b) Image of the same nanotubes when A_{free} = 86 nm, A_{setpoint} = 43 nm, ϕ = 43°. The same height scale applies to both panels (a) and (b). R_{tip} = 29 nm and k = 20.3 N/m.

Figure 2.1a shows an ac-mode AFM image (Asylum Research MFP-3D) of two CNTs with heights h = 2.4 and 1.5 nm. Compression of the two nanotubes during this image was minimized by driving the cantilever with a small free-air amplitude A_{free} = 11.5 nm and imaging with a correspondingly small amplitude set-point A_{setpoint} = 10.5 nm. The phase ϕ was monitored during image and remained > 90° (attractive mode imaging[10]). Figure 2.1b shows the same nanotubes imaged with Afree = 86 nm, Asetpoint = 43 nm, and $\phi < 90°$. The measured nanotube heights decrease to $h = 1.05$ and 0.55 nm, respectively. The reduction in h is reversible, and we see no evidence of mechanical damage to the nanotubes, the tip, or the substrate during our experiments.

The "gentle" imaging parameters used for Figure 2.1a are suitable for measuring the uncompressed height of a nanotube h_{max}.[11] Although the hammering force of the AFM tip on the sample is not a directly measured parameter in ac-mode AFM imaging, it is known that energy transfer from the tip to the sample is small when A_{free} is small and $\phi > 90°$. In Figure 2.1a, for example, E_{tap} the energy transferred from the tip to the sample during each cycle of cantilever motion was approximately 1 eV (energy dissipation calculations are described in Supporting Information). The "aggressive" imaging parameters used for Figure 2.1b clearly result in higher hammering forces (reduced h). We show below that this force is sufficient to flatten a SWNT or DWNT.

2.3 Results and Discussion

To quantify the compression of the larger nanotube in Figure 2.1b ($h_{\text{max}} = 2.4$ nm), we measured h as a function of radial compression force F. After acquiring an ac-mode image of the nanotube, the driven oscillation of the cantilever was stopped and the static deflection of the cantilever, Δ_{tip}, was monitored as the base of the cantilever was moved perpendicular to the surface by a distance z_{base}. Figure 2.2 shows the downward force, $F = k\Delta_{\text{tip}}$, acting on the sample as a function of tip position, $z_{\text{tip}} = z_{\text{base}} + \Delta_{\text{tip}}$, when the tip is engaged on either the substrate or the nanotube. To ensure that the tip was centered on the nanotube, a sequence of $F(z_{\text{tip}})$ curves were measured on a line of x-y coordinates which bisected the nanotube. Five measurements clearly engaged with the nanotube, and the three well-centered measurements are displayed in Figure 2.2. There is a time delay of several seconds between each $F(z_{\text{tip}})$ measurement.

During this delay, thermal drift changes z_{base} by a random distance of the order 1nm. To account for this drift, curves have been translated on the z_{tip} axis so that substrate and nanotube are separated by $h_{\max} = 2.4$ nm when $F = 0$ as F is increased from 0 to 50 nN, a 0.45 nm elastic deformation is observed on the CNT. At $F = 50$ nN the substrate and the nanotube curves are separated by 1.05 nm.

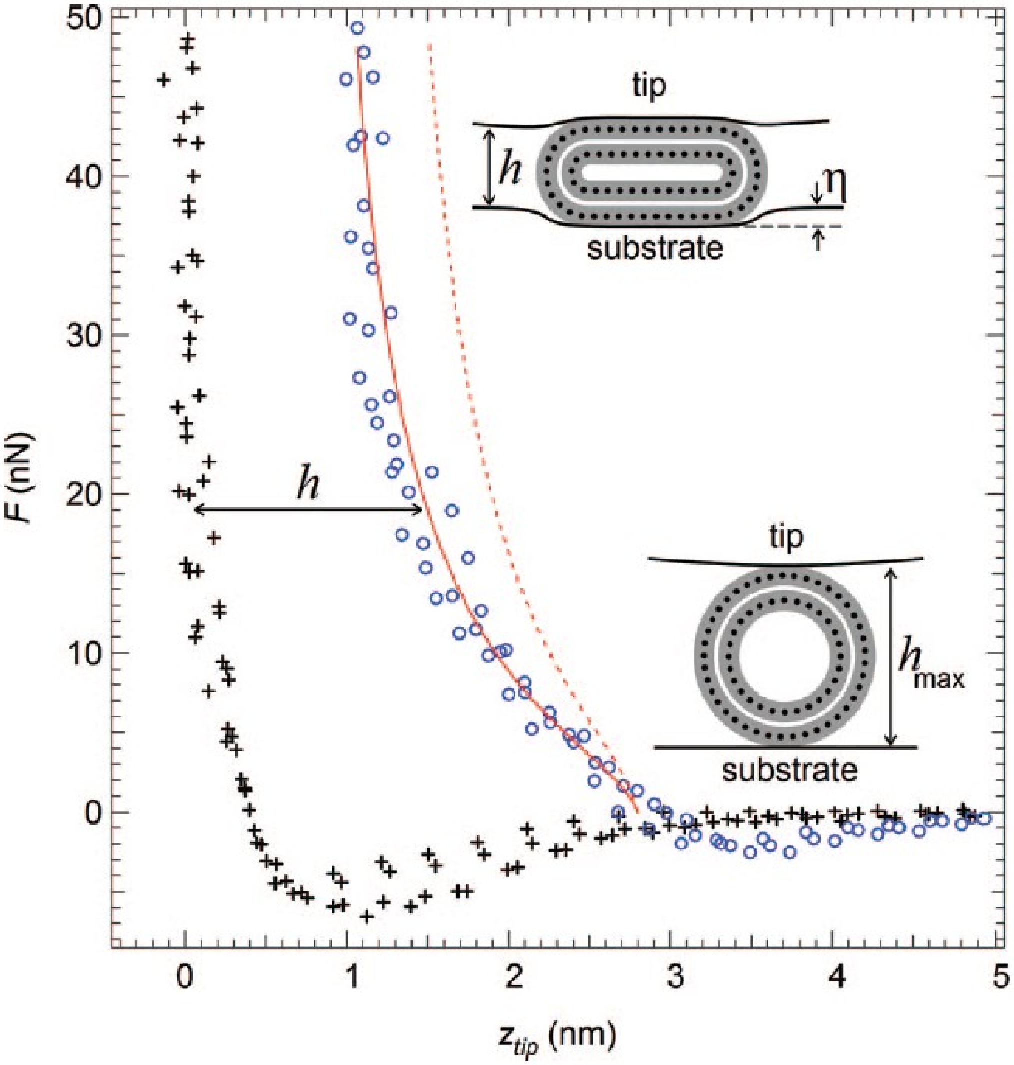

Figure 2.2. Static force-distance measurements with AFM tip. Crosses show the AFM tip engaging with the substrate with data from four different trials (two on

the left side of the CNT and two on the right side). Circles show the tip engaging with the DWNT (larger tube in Figure 2.1) with data from three different trials. Inset drawings show cross sections of the CNT during compression. Carbon ions in the CNT are represented by black dots. Grey bands depict the thickness of graphene, t, due to the electron cloud. For all measurements $R_{\mathrm{tip}} = 29$ nm, $\mathrm{d}z_{\mathrm{base}}/\mathrm{d}t = 50$ nm/s, data acquisition rate = 200 Hz and data is filtered with a low pass cutoff of 100 Hz. The dashed red line shows results of the graphene-bending model without considering additional substrate indentation. The solid red line shows results of the model when additional substrate indentation is included.

The minimum height 1.05 nm measured in Figure 2.1b and Figure 2.2 is consistent with expectations for a DWNT. The interlayer spacing of uncompressed graphite is 0.34 nm. Under high pressure (near the graphite-diamond transition), the interlayer spacing reaches 0.21 nm.[12] Therfore, if forces are sufficient to flatten the cross-section of a nanotube we naively expect $0.42 \text{ nm} < h < 0.68$ nm for SWNTs (the height of two graphene sheets under compression), and $0.84 \text{ nm} < h < 1.36$ nm for DWNTs. While this simple picture neglects nanoindentation of the substrate and the AFM tip (discussed below), minimum height is a useful way to tentatively assign a nanotube as SWNT or DWNT.

To confirm that the CNT is indeed double-walled we compare $F(h)$ to predictions based on the bending modulus of graphene. First principles modeling predicts that the energy cost per atom associated with bending a single sheet of graphene into a cylinder of diameter D is $U_{\mathrm{atom}} = \beta/D^2$, where β varies between 47 and 62 meV·nm^2 depending on details of the calculation.[7] We model the nanotube as two concentric graphene cylinders with $D_{\mathrm{outer}} = h_{\max} - t$ and $D_{\mathrm{inner}} = h_{\max} - 3t$ (see Figure 2.2), where $t \approx 0.34$ nm[13] and $\beta = 55$ meV·nm^2. (Note that the diameter of outer electron cloud surrounding the ionic lattice will be slightly smaller than $h_{\max}$ due to the electron cloud surrounding the ionic lattice). When the tube is compressed by the AFM tip ($R_{\mathrm{tip}} = 29$ nm), the geometry is similar to a garden hose squashed by a basketball (Figure 2.3). The radius of curvature of the AFM tip is much larger than D_{outer}, therefore when calculating bending energy the nanotube can be treated as mechanically decoupled rings. As rings evolve from circles to stadiums, bending energy is stored in the curved portion of the stadiums. The more the nanotube is squeezed, the more rings come into contact with the AFM tip. Using this model, we calculate the stored energy due to bending, $U_{\text{total}} = \Sigma U_{\text{atom}}$, and the corresponding compression force $F = |dU_{\text{total}}/dz_{\text{tip}}|$. The dashed line in Figure 2.2 shows the results of this fully constrained model.

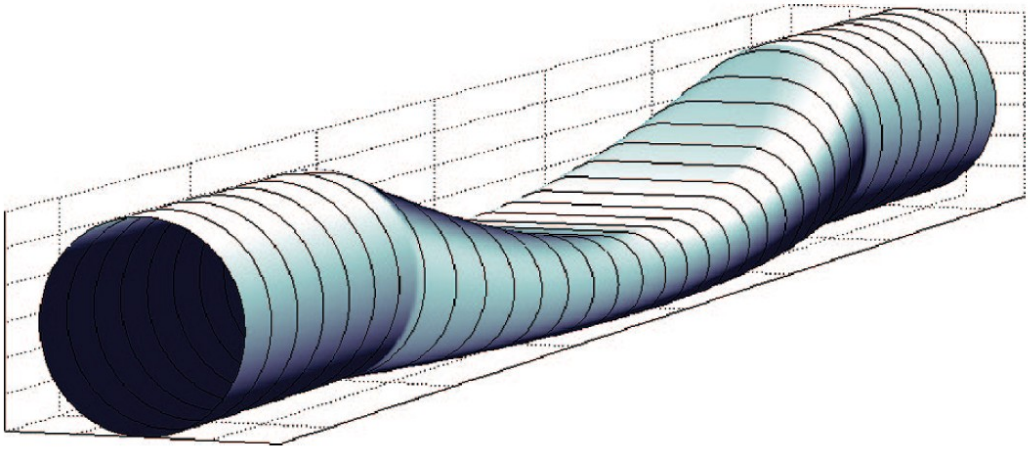

Figure 2.3. Diagram of a squashed CNT. Geometry of the squashed CNT corresponds to an AFM tip with $R_{\text{tip}} = 10D_{\text{outer}}$.

The discrepancy between measured $F(h)$ and the simple graphene-bending model (dashed line in Figure 2.2) is likely due to indentation of the AFM tip and the substrate. Figure 2.2 shows that some indentation occurs when the tip engages with bare silicon. Indentations will be even greater when a CNT is sandwiched between the two silicon surfaces due to the reduced contact area. The depth of the elastic indentation caused by a rigid sphere of radius R pressing on a flat silicon substrate is[14]

$$\eta = \left(\frac{3}{4\sqrt{R}} \frac{\left(1 - \nu_{\mathrm{Si}}\right)}{E_{\mathrm{Si}}} F \right)^{2/3}, \qquad (2.1)$$

where $E_{\mathrm{Si}} \approx 140$ GPa and $\nu_{\mathrm{Si}} \approx 0.2$ are the Young's modulus and Poisson ratio of silicon. The AFM tip will deform a similar amount leading to a total deformation $2\eta \approx 0.3$ nm at $F = 50$ nN. When the CNT is present in the sandwich a similar analysis based on effective contact area yields $2\eta \approx 0.6$ nm at $F = 50$ nN (the effective contact area is estimated as a fraction of the flattened nanotube surface in Figure 2.3). The additional indentation due to the presence of the CNT has the correct magnitude and function form to explain the discrepancy between measured $F(z_{\mathrm{tip}})$ and the simple graphene-bending model. We conclude that our measurements are consistent with predictions for a DWNT pushed by a silicon tip into a silicon substrate.

The effect of additional substrate indentation can be incorporated into the graphene-curvature model in a very simple way. A small increase in Douter and Dinner simulates the extra space $\eta(F)$ created when the CNT sinks into the substrate. The solid curve in Figure 2.2 shows the graphene-curvature model with $D_{\mathrm{outer}} = h_{\max}$ and $D_{\mathrm{inner}} = h_{\max} - 2t$, no other parameters have been changed with respect to the dashed line. It appears to be a coincidence that $\eta(F)$ is a similar magnitude to t, leading to this simple relationship between $h_{\max}$ and D_{outer} used for modeling.

The close agreement between the mechanical model and radial compression measurements (Figure 2.2) suggests that force-height data can be used as a signature to distinguish between SWNTs, DWNTs, and nanotube bundles. We tested the model on a possible SWNT (the smaller nanotube in Figure 2.1) by determining h as a function of tapping force F_{tap}. A series of images were obtained with a different A_{free} and A_{setpoint} values. For each image, F_{tap} was determined by measuring the height of the DWNT and comparing to the known force-height relationship of the DWNT (Figure 2.2). The uniformity of F_{tap} across the image was inferred from energy dissipation maps which showed equal energy dissipation on the substrate and on the centerlines of the two nanotubes (see Supporting Information). Figure 2.4 shows the resulting $h(F_{\mathrm{tap}})$ curve of the smaller nanotube. The nanotube reaches a minimum height of 0.55 nm at 25 nN, and the $h(F_{\mathrm{tap}})$ curve is in excellent agreement with the prediction of our mechanical model for single graphene cylinder of diameter 1.5 nm. We conclude that the nanotube is indeed single-walled.

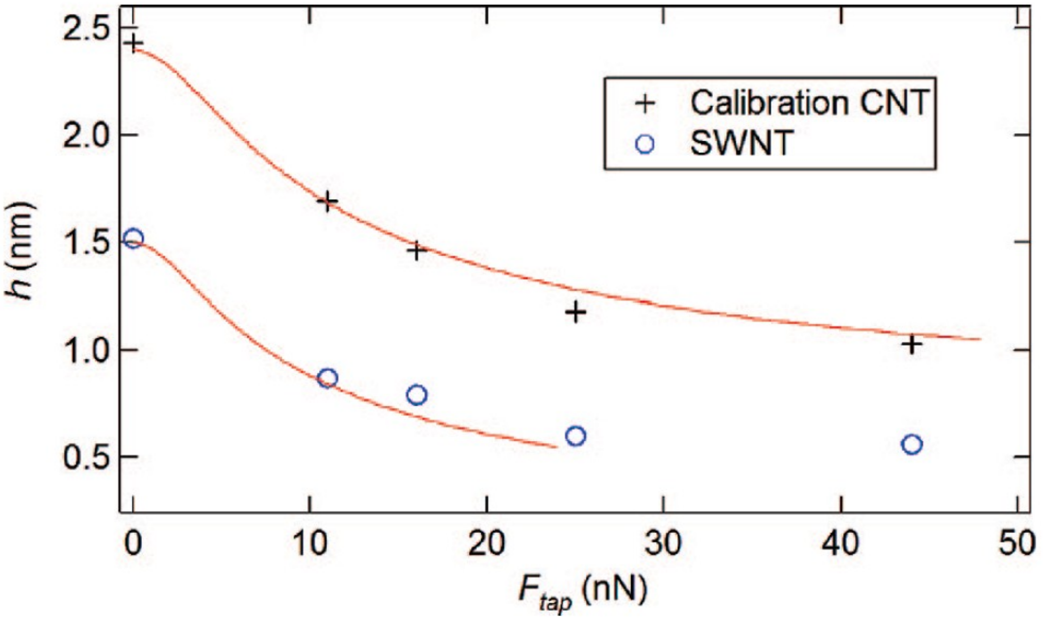

Figure 2.4. CNT compression during AFM imaging. Nanotube height measured by ac-mode AFM at increasingly aggressive imaging parameters. The CNT measured in Figure 2.2 is used to calibrate F_{tap}. Heights were extracted from AFM images by finding the average z coordinate on top of the nanotube (20 pixel average) and subtracting the average height of the substrate (~100 x 100 pixel average). The solid lines are modeled $h(F)$ for a DWNT and a SWNT with D_{outer} = 2.4 and 1.5 nm, respectively. The high force region, where graphene cylinders

are completely flattened, has not been modeled. Imaging parameters (A_{free} (nm), A_{set} (nm), ϕ) from smallest to largest F_{tap} are as follows (11.5, 10.6, 116°), (44.7, 39.7, 76°), (57.3, 42.5, 61°), (71.6, 42.5, 49°), and (86..1, 42.5, 43°).

The calibrated F_{tap} imaging technique described above circumvents experimental issues associated with measuring force-distance curves of smaller diameter CNTs (it is very difficult to obtain $F(z_{\mathrm{tip}})$ data such as Figure 2.2 on SWNTs, as evidenced by previous attempts[5,6]). We have used this technique on both silicon and silicon oxide substrates to indentify SWNTs and DWNTs (further examples are provided in Supporting Information). In all cases we found close agreement between experimental $h(F_{\mathrm{tap}})$ curves and the appropriate SWNT/DWNT mechanical model with $D_{\mathrm{outer}} = h_{\mathrm{max}}$ and $\beta = 55$ meV·nm^2.

2.4 Conclusion

In conclusion, measurements of h as a function of compression force (F or Ftap) can be used to indentify individual SWNTs and DWNTs. This AFM characterization technique will be useful for future investigation of the mechanical and electrical properties of CNT with known structure. Our measurements of radial compression are consistent with a graphene bending modulus $\beta = 55 \pm 10$ meV·nm^2 and highlight the importance of considering substrate indentation. More accurate determination of β will be possible by detailed modeling of the experiments described here, and future experiments using AFM tips and substrates made from high Young's modulus materials such as diamond.

2.5 Acknowledgements

We thank Guenter Schneider and Jason Li for useful discussions.

2.6 Supporting Information

A) Scatter plot of $h(F_{\mathrm{tap}} \sim 50$ nN) vs. $h_{\max}$ for all CNTs with $h_{\max} < 1.5$ nm

We have verified SWNTs in our sample are consistently compressed to the same height. We searched for SWNT candidates by looking for nanotubes with small h_{max} (measured by gentle ac-mode imaging). After determining h_{max} we changed imaging parameters to replicate $F_{\mathrm{tap}} \sim 50$ nN. F_{tap} was approximate because no comparison was made between $F(z_{\mathrm{tip}})$ curves and imaged heights. All 9 nanotubes with $h_{\mathrm{max}} < 1.5$ nm shrunk to $h = 0.55 \pm 0.1$ nm when imaged with $F_{\mathrm{tap}} \sim 50$ nN. This is compelling evidence that SWNTs have a distinct "fully compressed" height that can be measured by ac-mode AFM. However, we note that calibrated force-height curves would be necessary to determine whether these 9 nanotubes were individual SWNTs or two SWNTs bundled together (modeling of three nanotubes bundled together predicts $h > 0.55$ nm when $F = 50$ nN and $R_{\mathrm{tip}} \sim 30$ nm).

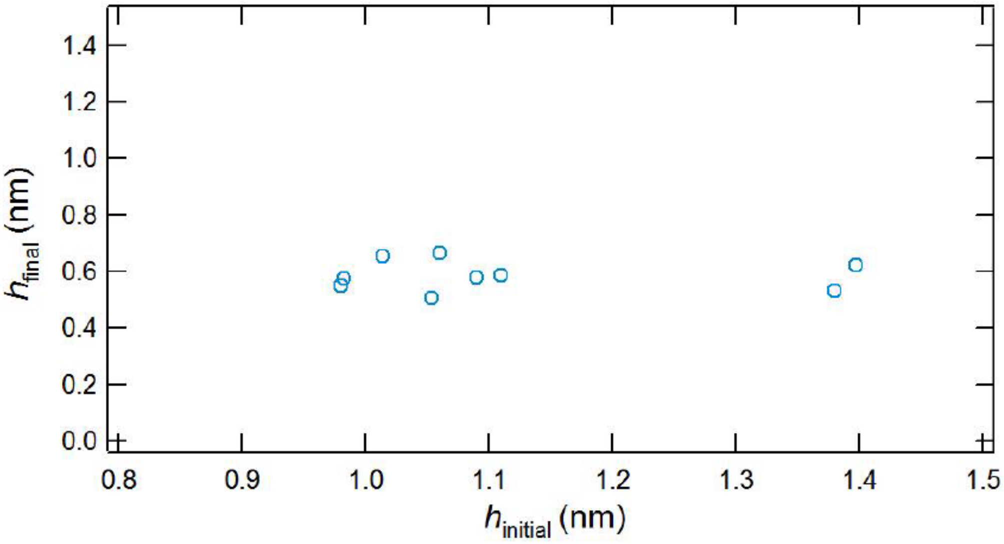

Figure 2.S1. Compressed vs. initial CNT height. The height of nanotubes when F_{tap} is near zero (h_{initial}), compared to the height when F_{tap} ~ 50 nN. This data set includes all nanotubes that were found with $h_{\text{initial}} < 1.5$ nm.

B) Map of E_{tap} when imaging nanotubes in Figure 2.1

During ac-mode imaging, the AFM tip transfers mechanical energy from the AFM cantilever to the sample. The energy transferred per cycle of cantilever motion *E*tap is given by[10]:

$$E_{\text{tap}} = \frac{\pi k A^2}{Q}\left[\left(\frac{A_{\text{free}}}{A}\right)\sin\phi - 1\right], \qquad (2.\text{S}1)$$

where A is the amplitude of the cantilever (A is approximately equal to the imaging set point, A_{setpoint}) and ϕ is the phase difference between the force driving the cantilever and the displacement of the cantilever. The rate of energy transfer is $P_{\text{tip}} = E_{\text{tap}}f$ where f is the resonant frequency of the cantilever.

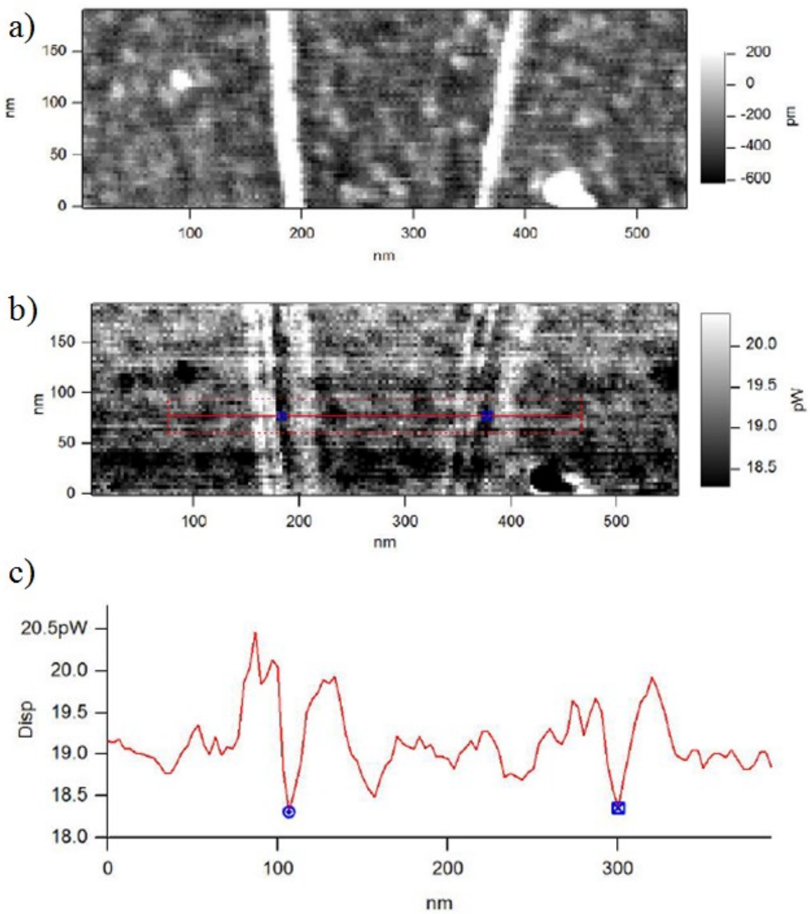

Figure 2.S2. AFM measurement of energy dissipation on two CNTs. (a) Height image of the nanotubes in Figure 2.1. $A_{\mathrm{free}} = 71.6$ nm and $A_{\mathrm{setpoint}} = 42.5$ nm and average phase on the substrate $\phi = 49.3°$. (b) Corresponding P_{tip} image calculated using Eq. 2.S1. (c) Cross section of the energy dissipation image taken from red line in (b).

Interestingly, P_{tip} peaks on either side of a nanotube. This is consistent with the nanotube sliding sideways on the surface during imaging. We hypothesize this sliding motion is reversible (nanotube position is restored by tension in the nanotube) and that energy is dissipating due to friction with the surface. Two further observations support this hypothesis: (1) Positions of high

P_{tip} correspond to height measurements equal to the substrate height as expected if the nanotube slides out of the way when the AFM tip hammers off-center. (2) During attractive mode imaging, when hammering force is less, height images of a nanotube appear wider by 5 to 10 nm.

C) Calibrated $h(F_{\text{tap}})$ curve for a DWNT on a silicon substrate

Two nanotubes, deposited from solution on a silicon substrate, were imaged with a range of A_{free} and A_{setpoint} values (see Table 2.S1 below). $R_{\text{tip}} = 29$ nm and $k = 27.7$ N/m. One image of the 11 images is shown below in Figure 2.S3a. The heights of the left and right nanotubes (h_{left} and h_{right}) were measured from cross sections of the images (20 pixel average). We assume that F_{tap} was approximately zero when $A_{\text{free}} = 5.14$ nm. We find $h_{\text{max}} = 2.72$ nm for the left nanotube and 1.68 nm for the right nanotube. $F(z_{\text{tip}})$ curves were measured for the left nanotube to facilitate calibration of F_{tap}. For a given height h_{left} in Table 2.S1, the corresponding F_{tap} was determined from the $F(z_{\text{tip}})$ curves (Figure 2.S3b).

Table 2.S1. AFM parameters for imaging DWNT

F (nN)	h left (nm)	h right (nm)	A_free	A_set	Phase (deg.)
0	2.72	1.68	5.14	2.88	129
7	2.65	1.57	8.42	4.8	131
19	2.15	1.3	13.66	7.69	134
28	2.02	1.18	17.55	14.41	112
44	1.8	0.95	26.03	16.38	54
55	1.72	0.91	32.83	18.73	45
61	1.64	0.89	38.94	22.09	42
69	1.61	0.87	44.87	25.46	41
82	1.54	0.86	57.8	32.66	38
115	1.46	0.82	62.91	32.66	34
133	1.4	0.82	82.18	32.66	26

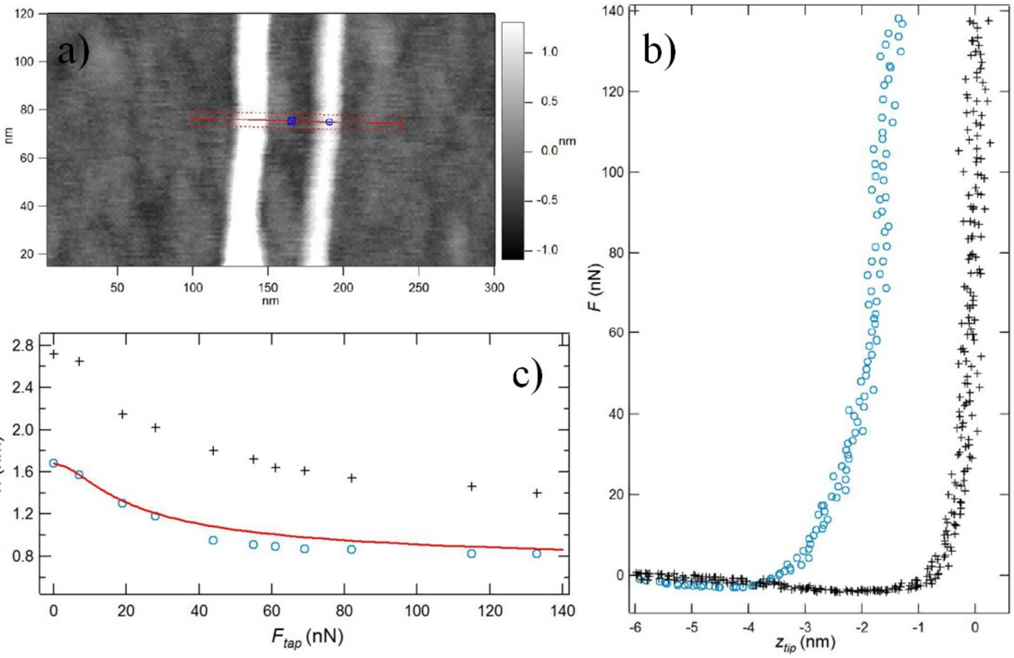

Figure 2.S3. AFM compression measurement on DWNT. (a) Height image of the nanotubes on silicon. A_{free} = 8.42 and A_{setpoint} = 4.8 nm and average phase on the substrate ϕ = 131.4. (b) Force-distance curves measured on the silicon substrate (black crosses) and the calibration CNT (blue circles). Curves have been separated by $h_{\max}$ = 2.72 nm at F = 0. (c) $h(F_{\text{tap}})$ plots for the calibration CNT (black crosses) and the right CNT (blue circles). The red line shows the modeled compression of a DWNT by an AFM tip with R_{tip} = 29 nm.

Using the calibrated values of F_{tap}, we plotted $h(F_{\text{tap}})$ for the calibration nanotube (left tube) and the right nanotube. The $h(F_{\text{tap}})$ curves were compared to models of individual SWNTs and DWNTs. The DWNT model (D_{outer} = 1.68 nm) fits the height data from the left nanotube and we conclude that the left nanotube is a bundle or a larger multi-walled nanotube.

D) Calibrated $h(F_{\text{tap}})$ curve for a SWNT and a bundle of two SWNTs

Two nanotubes grown by CVD on an oxide substrate (200 nm thermally grown silicon oxide on silicon) were imaged with a range of A_{free} and A_{setpoint} values (see Table 2.S2 below). R_{tip} = 83 nm and k = 32.65 N/m. One of the 9 images is shown below in Figure 2.S4a. The heights of the left and right nanotubes were measured from cross sections of the images avoiding areas of clear surface contamination. We assume that F_{tap} was approximately zero at the smallest A_{free} value. We find h_{max} = 1.86 nm for the left nanotube and 1.38 nm for the right nanotube. $F(z_{\mathrm{tip}})$ curves were measured for the left nanotube to allow calibration of F_{tap}. For a given height h_{left} in Table 2.S2, the corresponding F_{tap} was determined from the $F(z_{\mathrm{tip}})$ curves.

Table 2.S2. AFM parameters for imaging SWNT bundle

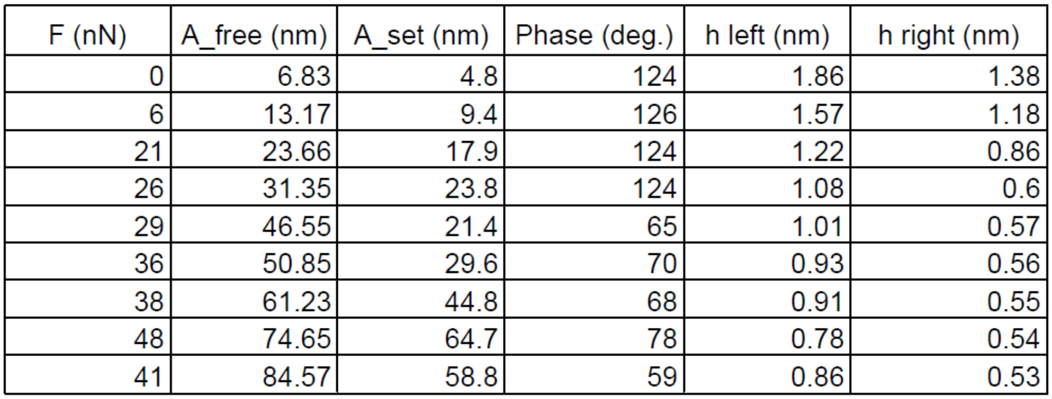

F (nN)	A_free (nm)	A_set (nm)	Phase (deg.)	h left (nm)	h right (nm)
0	6.83	4.8	124	1.86	1.38
6	13.17	9.4	126	1.57	1.18
21	23.66	17.9	124	1.22	0.86
26	31.35	23.8	124	1.08	0.6
29	46.55	21.4	65	1.01	0.57
36	50.85	29.6	70	0.93	0.56
38	61.23	44.8	68	0.91	0.55
48	74.65	64.7	78	0.78	0.54
41	84.57	58.8	59	0.86	0.53

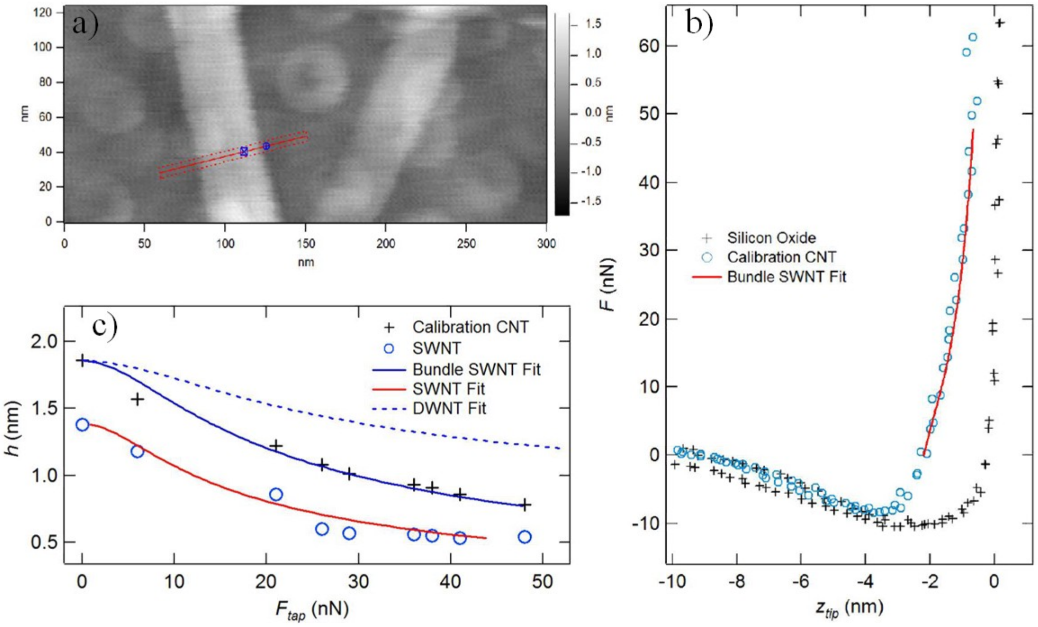

Figure 2.S4. AFM compression measurement on SWNT bundle. (a) Height image of two nanotubes on silicon oxide. A_{free} = 31.4 nm and A_{setpoint} = 23.8 nm and average phase on the substrate ϕ = 124°. (b) Force-distance curve measured over the silicon oxide substrate (black crosses) and calibration CNT (blue circles). Curves have been separated by $h_{\max}$ of the calibration tube measured in attractive ac-mode AFM. (c) $h(F_{\mathrm{tap}})$ plots for the calibration CNT (black crosses and the right CNT (blue circles).

Using the calibrated Values of F_{tap}, we plotted $h(F_{\mathrm{tap}})$ for the two nanotubes. Mechanical models of the individual SWNTs and DWNTs were compared to the $h(F_{\mathrm{tap}})$ data. The SWNT model (D_{outer} = 1.38 nm) fits the height data from the right nanotube very well. Mechanical models of an individual SWNT of DWNT model do not agree with measurements of the left nanotube. However, $h(F_{\mathrm{tap}})$ data from the left nanotube agrees very well with a model of two SWNTs (both with D_{outer} = 1.86 nm). Therefore, we identify the left nanotube as a bundle of two SWNTs.

2.7 References

1 Qian, D., Wagner, G. J., Liu, W. K., Yu, M.-F. & Ruoff, R. S. Mechanics of carbon nanotubes. *Applied Mechanics Reviews* **55**, 495-, doi:10.1115/1.1490129 (2002).

2 Palaci, I. *et al.* Radial elasticity of multiwalled carbon nanotubes. *Physical Review Letters* **94**, 175502- (2005).

3 Yu, M.-F., Kowalewski, T. & Ruoff, R. Investigation of the Radial Deformability of Individual Carbon Nanotubes under Controlled Indentation Force. *Physical Review Letters* **85**, 1456-9, doi:10.1103/PhysRevLett.85.1456 (2000).

4 Shen, W., Jiang, B., Han, B. & Xie, S.-s. Investigation of the Radial Compression of Carbon Nanotubes with a Scanning Probe Microscope. *Physical Review Letters* **84**, 3634-7, doi:10.1103/PhysRevLett.84.3634 (2000).

5 Fraxedas, J., Rius, G., Pérez-Murano, F. & Verdaguer, A. Determining radial breathing mode frequencies of single-walled carbon nanotubes with an atomic force microscope. *Europhysics Letters (EPL)* **78**, 16001-, doi:10.1209/0295-5075/78/16001 (2007).

6 Wang, H.-Y., Zhao, M. & Mao, S. X. Radial moduli of individual single-walled carbon nanotubes with and without electric current flow. *Applied Physics Letters* **89**, 211906-, doi:10.1063/1.2392825 (2006).

7 Robertson, D., Brenner, D. & Mintmire, J. Energetics of nanoscale graphitic tubules. *Physical Review B* **45**, 12592-5, doi:10.1103/PhysRevB.45.12592 (1992).

8 Kong, J., Soh, H. T., Cassell, A. M., Quate, C. F. & Dai, H. Synthesis of individual single-walled carbon nanotubes on patterned silicon wafers. *Nature* **395**, 1-4, doi:10.1038/27632 (1998).

9 Hutter, J. L. & Bechhoefer, J. Calibration of atomic-force microscope tips. *Review of Scientific Instruments* **64**, 1868-, doi:10.1063/1.1143970 (1993).

10 Cleveland, J. P., Anczykowski, B., Schmid, A. E. & Elings, V. B. Energy dissipation in tapping-mode atomic force microscopy. *Applied Physics Letters* **72**, 2613-, doi:10.1063/1.121434 (1998).

11 Postma, H. W. C., Sellmeijer, A. & Dekker, C. Manipulation and Imaging of Individual Single-Walled Carbon Nanotubes with an Atomic Force Microscope. *Advanced Materials* **12**, 1299-302, doi:10.1002/1521-4095(200009)12:17<1299::aid-adma1299>3.3.co;2-f (2000).

12 Alder, B. J. & Christian, R. H. Behavior of Strongly Shocked Carbon. *Physical Review Letters* **7**, 367-9 (1961).

13 Kiang, C. H., Endo, M., Ajayan, P., Dresselhaus, G. & Dresselhaus, M. Size Effects in Carbon Nanotubes. *Physical Review Letters* **81**, 1869-72, doi:10.1103/PhysRevLett.81.1869 (1998).

14 Oliver, W. C. & Pharr, G. M. Measurement of hardness and elastic modulus by instrumented indentation: Advances in understanding and refinements to methodology. *J Mater Res* **19**, 3-20, doi:DOI 10.1557/jmr.2004.19.1.3 (2004).

CHAPTER 3

A Spectrally-Tunable Photocurrent Microscope for Characterizing Nanoelectronic Devices

T. DeBorde, J. W. Kevek, T. Sharf, J. L. Wardini, and E. D. Minot

IEEE 11th International Conference on Nanotechnology, 2011

3.1 Introduction

Nanoscale materials often have unique and beneficial electronic and optoelectronic properties.[1] For example, recent studies of carbon-based optoelectronic devices have shown promise in the fields of photodetection, high-speed optical communications, and solar energy conversion.[2-4]

Scanning photocurrent microscopy (SPCM), and the closely related technique of scanning photoconductivity microscopy, are versatile methods for investigating optoelectronic properties of nanoelectronic devices.[4-6] In both techniques, a focused laser spot is raster scanned across a device while recording current (see Figure 3.1). Figure 3.1b shows an SPCM image superimposed on top of an atomic force microscopy (AFM) height image of a carbon nanotube field effect transistor (CNT FET). The color of each pixel corresponds to the measured current when the laser spot is centered on the *x*-*y* coordinates of the pixel. This measurement technique has been used with single-wavelength laser sources to investigate the optoelectronic properties of nanomaterial-metal interfaces (nanowire-metal, CNT-metal, and graphene-metal)[7-11] and nanoelectronic devices with other sources of built-in electric fields.[4,12]

Additional information about nanoelectronic devices can be gained by using a wavelength-tunable light source. Freitag et al. used wide-field illumination with a tunable Ti-Sapphire laser to measure resonant photoconductivity in CNT FETs.[13] Lee et al. used wide-field wavelength-tunable illumination from a monochromated white light source to investigate photocurrent resonances in CNT *p*-*n* junctions.[12] More recently, a tunable light source was combined with a scanning microscope to give both spatial and spectral resolution.[4] Gabor et al. used this technique to measure multiple electron generation in CNT photodiodes.[4]

The goal of our current work is to expand the capabilities of spectrally-tunable SPCM. Here we describe the construction of an SPCM instrument with a light source that has an extremely tunable spectral range and sample intensities above 5 kW/cm^2 per nanometer of bandwidth.

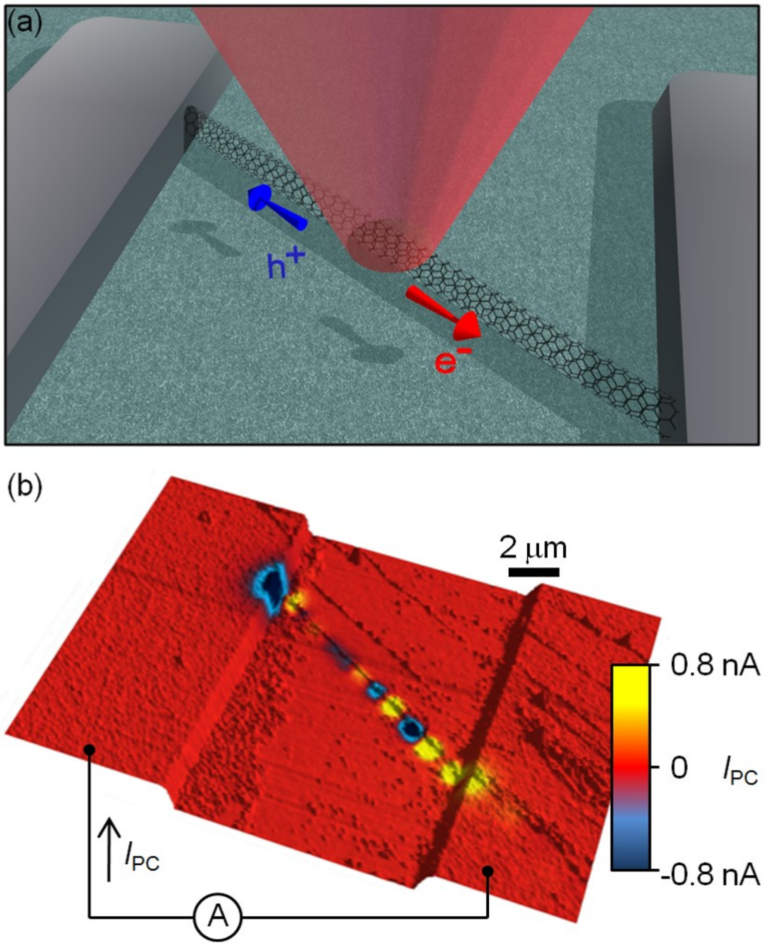

Figure 3.1. SPCM measurement example. (a) Cartoon diagram of a scanning photocurrent measurement. (b) SPCM image from a CNT FET device taken at 632 nm, 800 μW, and FWHM of approximately one micron. The photocurrent image has been superimposed onto an AFM height image of the device. The other nanotubes in the image do not make it across the electrode gap and show no photocurrent response.

3.2 Microscope Design

Our SPCM instrument diagramed in Figure 3.2 uses a Fianium super continuum laser (SC-450) as the primary light source. The super continuum outputs a wide wavelength range between 450 nm – 1800 nm with a roughly constant spectral power density (4 W total output power). A monochromator (Micro HR, *Horiba*) is used to select and control the output wavelength and bandwidth. The typical output bandwidth used for the measurements reported here was approximately 5 nm. In this configuration we are able to deliver a few hundred micro-watts of power to the sample with a micron scale spot size in the visible spectrum.

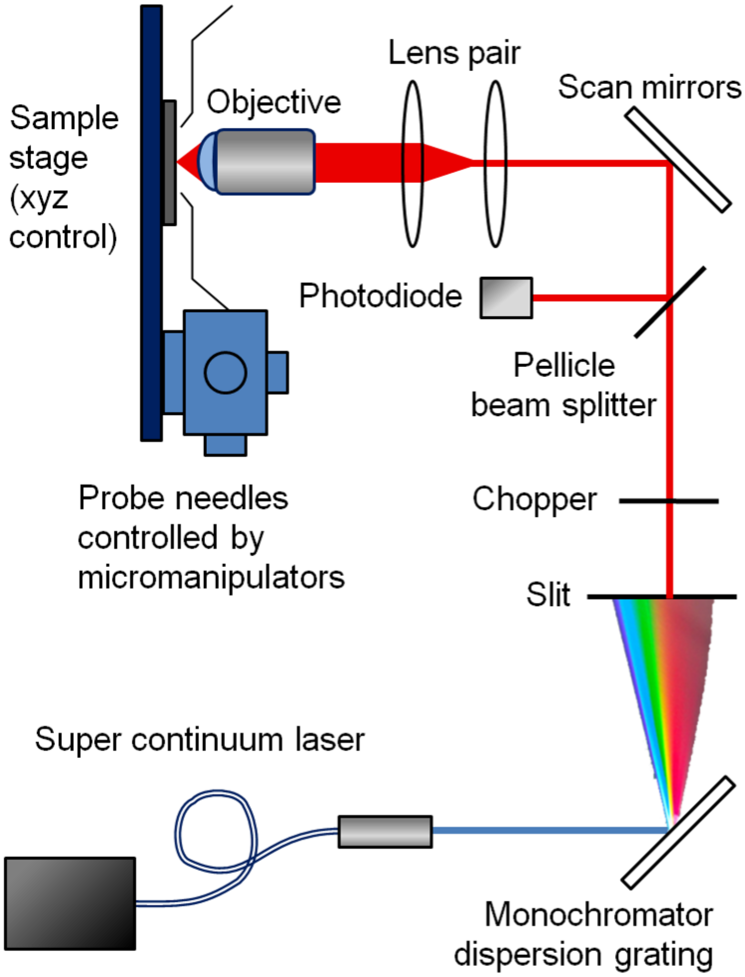

Figure 3.2. Schematic diagram of scanning photocurrent microscope.

We use a pair of scan mirrors (OHF-7, QD-4000, *Nutfield Technology*) to control the laser position on the sample. A pair of lenses (Achromatic Doublets with focal lengths of 5.0 cm and 7.5 cm, *Thorlabs*) is placed between the scan mirrors and the objective. This pair of lenses ensures that the collimated light source is centered in the middle of the back plane of the objective for all scan mirror angles.

For some applications it is desirable to increase excitation bandwidth to increase excitation power. However, opening the exit slit of the monochromator to increase bandwidth adversely affects image resolution due to the dispersion from the monochromator grating. A planned improvement to our setup is the use of a double monochromator operated in subtractive mode to remove the dispersion from the monochromated beam.

An additional feature that we have incorporated in our instrument is reflection imaging. Reflection images can be acquired simultaneously with photocurrent images, allowing us to determine laser position relative to the metal electrode structure. A pellicle beam splitter (92:8, *Thorlabs*) directs reflected light to a photodiode (PDA100A, *Thorlabs*). The electrodes (patterned thin metal films) reflect more strongly than the SiO_2/Si substrate.

Reflection imaging is also a convenient method of determining laser spot size (Figure 3.3). We define the normalized reflection R_{N} as

$$R_{\mathrm{N}} = \frac{R - R_{\mathrm{Si}}}{R_{\mathrm{M}} - R_{\mathrm{Si}}}, \qquad (3.1)$$

where R is the measured reflection signal, R_{Si} is the reflection from the SiO_2/Si substrate and R_{M} is the reflection from the metal electrode. Figure 3.3b shows R_{N} as a HeNe laser is scanned across the abrupt edge of a metalized area. The full-width at half max (FWHM) is estimated to be 1.1 μm. A similar FWHM is found for the super continuum light source when the bandwidth output is set to one nanometer. The focusing objective is a 50x, extra long working distance objective with a numerical aperture of 0.55 (CFI LU Plan BD ELWD 50X A, *Nikon*).

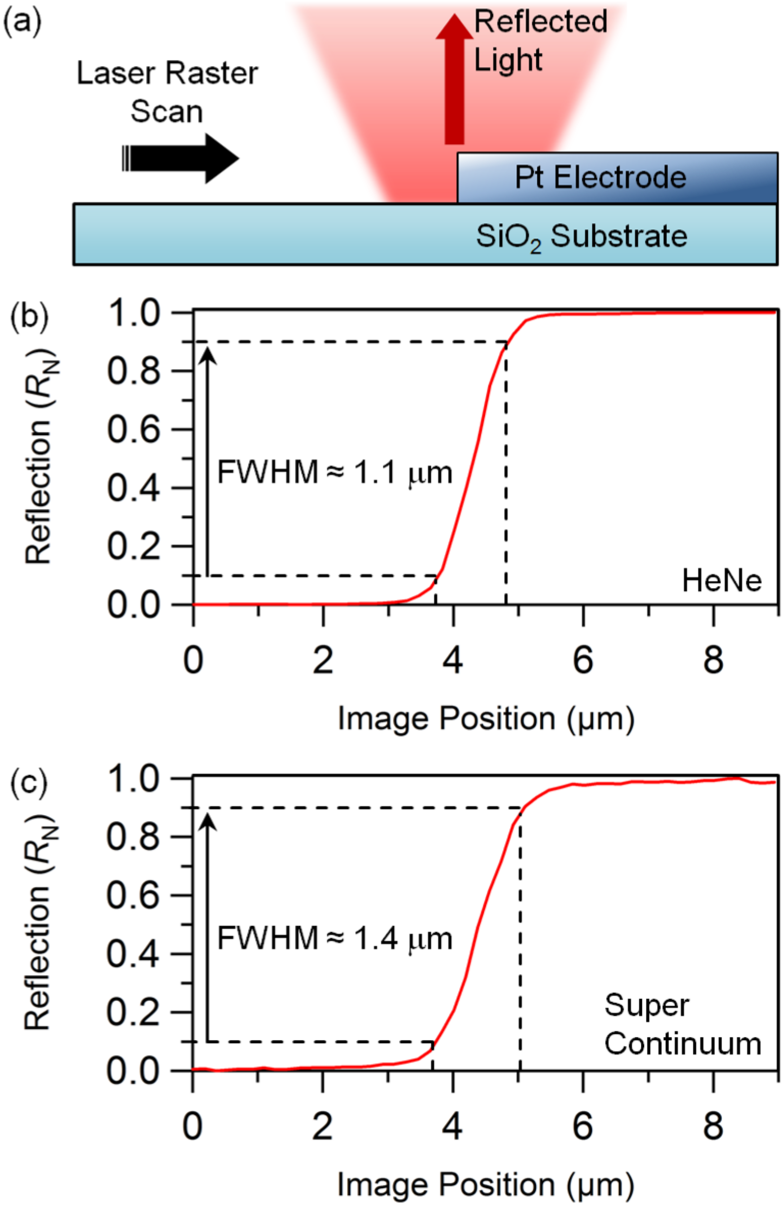

Figure 3.3. Reflection imaging spot size characterization. (a) Cartoon diagram of laser spot halfway onto a metal electrode corresponding to $R_N = 0.5$. (b) R_N of electrode edge from HeNe laser. (c) R_N of electrode edge from super continuum laser with monochromator output set to 632.8 nm and 1 nm bandwidth.

3.3 Results and Discussion

A. Photocurrent Imaging of a Typical CNT FET Device

An AFM height image and transistor curve for an ambipolar CNT FET device is shown in Figure 3.4. The device is made using chemical vapor deposition (CVD) growth of CNTs and standard photolithography techniques as described by Prisbrey et al.[14] The transistor curve in Figure 3.4b shows a large amount of advancing hysteresis when sweeping the gate voltage (V_g). Figure 3.4b shows that when $V_g = 0$ V the device is p-type (Fermi energy below the band gap) and when $V_g = 10$ V the device is n-type (Fermi level above the band gap) if dV_g/dt is sufficiently fast.

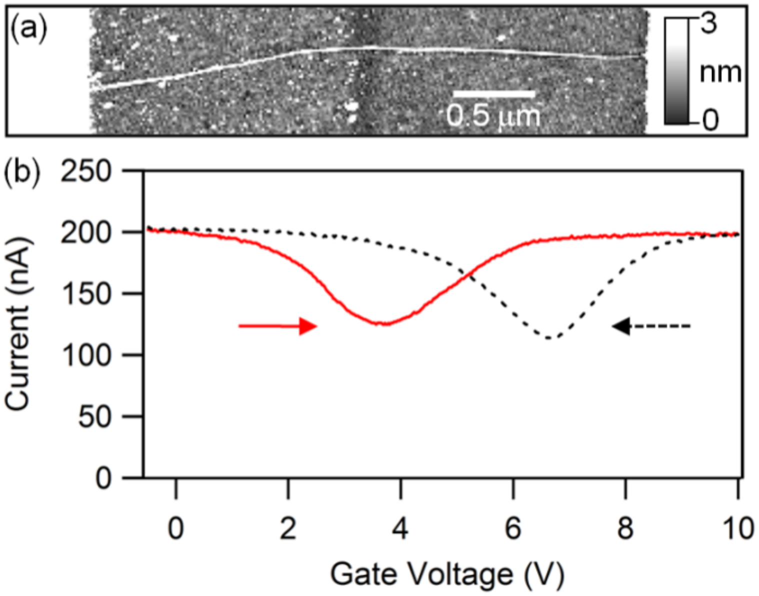

Figure 3.4. Ambipolar CNT FET device characteristics. (a) AFM Height image of CNT on SiO_2 crossing electrode gap. Scale bar is 0.5 µm. (b) Transistor curve of device. The solid (dashed) curve is an increasing (decreasing) V_g sweep. $V_{sd} = 25$ mV, $dV_g/dt = 0.5$ V/s.

To study the optoelectronic properties of this device we performed SPCM image at different gate voltages. Figure 3.5a shows a photocurrent image obtained at V_g = 0 V and with no bias across the source and drain electrodes (V_{sd} = 0 V, same configuration as Figure 3.1b). There are clear photocurrent spots visible at the left and right CNT-metal interfaces. A similar image was taken immediately after sweeping V_g to +10 V (Figure 3.1c). With the Fermi level in the conduction band, the polarity of the photocurrent spots switches sign.

Photocurrents generated at CNT-electrode interfaces have been studied by several previous authors.[5,8,9,15] The effect is typically attributed to a photoelectric effect, whereby the built-in electric field at a CNT-metal interface drives the photo-excited carriers either toward or away from the metal.[8,9] Thus, the polarity of this interfacial photocurrent is thought to depend on whether the CNT FET is operating in a p-type or n-type regime.

The reversal of photocurrent polarity observed in Figure 3.5c is not permanent and appears related to the device hysteresis. Photocurrent measurements were acquired for several minutes after V_g was swept from 0 V to 10 V and then held at 10 V (Figure 3.5d-h). Each image took 30 seconds to acquire. As time progresses we can visualize the hysteresis advance as it affects the photocurrent response. By the last image, V_g = 10 V, t = 410 s, the photocurrent closely resembles the starting structure shown in Figure 3.5a where V_g = 0 V.

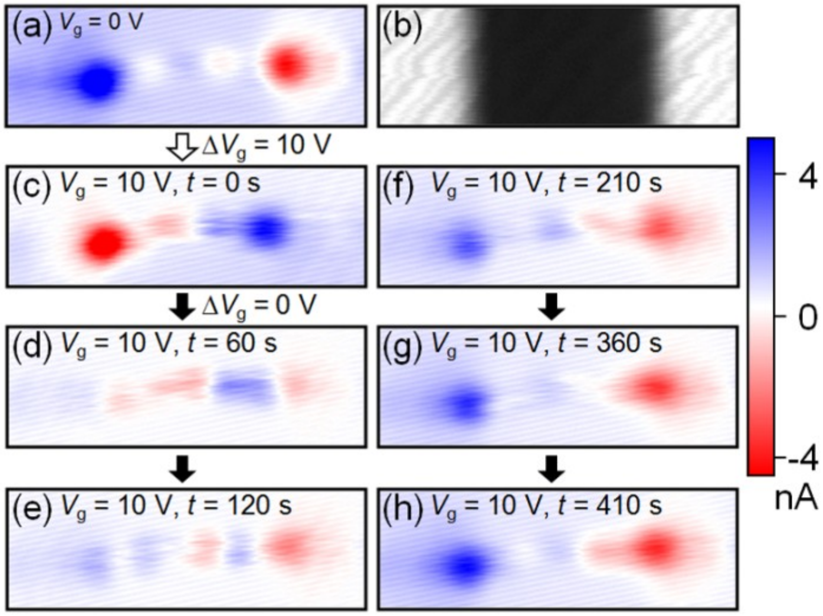

Figure 3.5. Imaging CNT FET hysteresis. (a) SPCM image of device in Figure 3.4 at V_g = 0V (b) Corresponding reflection image of device. (c) SPCM image taken immediately after sweeping V_g to 10 V. (d)-(h) Multiple SPCM images showing transient photocurrent behavior while V_g is held at 10 V. (d) t = 60 seconds (e) t = 120 seconds (f) t = 210 seconds (g) t = 360 seconds (h) t = 410 seconds.

Previous work by Lee et al. proposed that charge transfer between the CNT and silanol charge traps residing at the SiO_2-air interface causes advancing hysteresis in un-passivated CNT FET devices.[16] We conjecture that the photocurrent evolution shown in Figure 3.5 reflects this migration of charge on the device surface, which eventually nullifies the applied gate voltage.

Hysteresis presents a challenge for many potential studies of optoelectronic properties. The Fermi energy of the CNT cannot be held at a stable level to allow detailed studies. One approach to solve this problem is passivation by dielectric encapsulation.[17] A second strategy to reduce hysteresis, described below, is to use suspended CNT FET devices.

B. Photoconductivity Spectrum of a Suspended CNT FET

Figure 3.6a shows the transistor behavior of a suspended semiconducting CNT. As seen by previous authors[18], the suspended device geometry shows significantly less hysteresis than surface-bound CNT FETs. The CNT bridges a pair of Pt electrodes that are separated by a 1 μm gap that is 1 μm deep (see inset to Figure 3.6a). Details of the fabrication steps will be reported by Sharf et al.[19] A reflection image and short-circuit photocurrent image of the device are shown in Figure 3.6b and c respectively. The reflection image clearly shows the Pt electrodes and the islands of catalyst that were placed on top of the Pt to facilitate growth of CNTs by chemical vapor deposition.

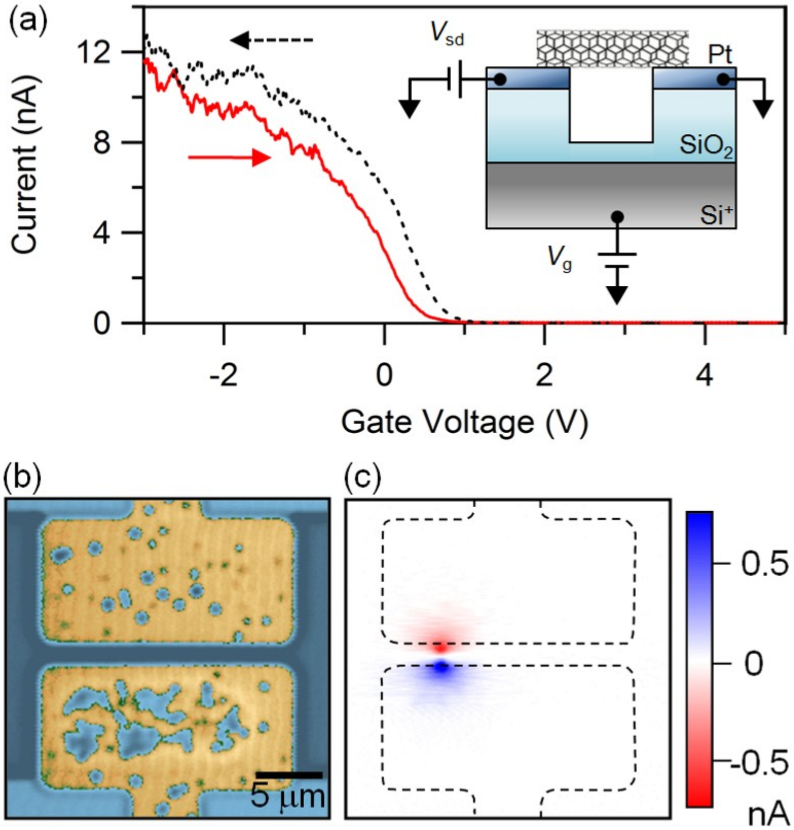

Figure 3.6. Suspended CNT FET device characteristics. (a) Transistor curve of device. V_{sd} = 25 mV, dV_g/dt = 0.5 V/s. Inset shows device geometry (b) Reflection

image of device. (c) Short circuit photocurrent image of device taken with lock-in amplifier.

Figure 3.7 shows the spectrally-resolved photoconductivity of the suspended CNT. The monochromated light source was focused on the center of the suspended CNT (half-way between the photocurrent spots seen in Figure 3.6c). The gate voltage was set to 1.8 V, ensuring that the transistor was in the off state (depleted of charge carriers). A dc bias of 200 mV was applied between the source and drain electrodes. The monochromated light source was chopped at 3 kHz and was varied from 455 nm (2.73 eV) to 750 nm (1.65 eV). The photoinduced current was measured with a lock-in amplifier (SR830, *SRS*). The spectral response shows sharp resonances at 1.82 eV and 2.17 eV. The spectral power density of the light source is shown in Figure 3.7b. Clearly, the spectral peaks in the photoinduced current are not related to the incident power of the light source.

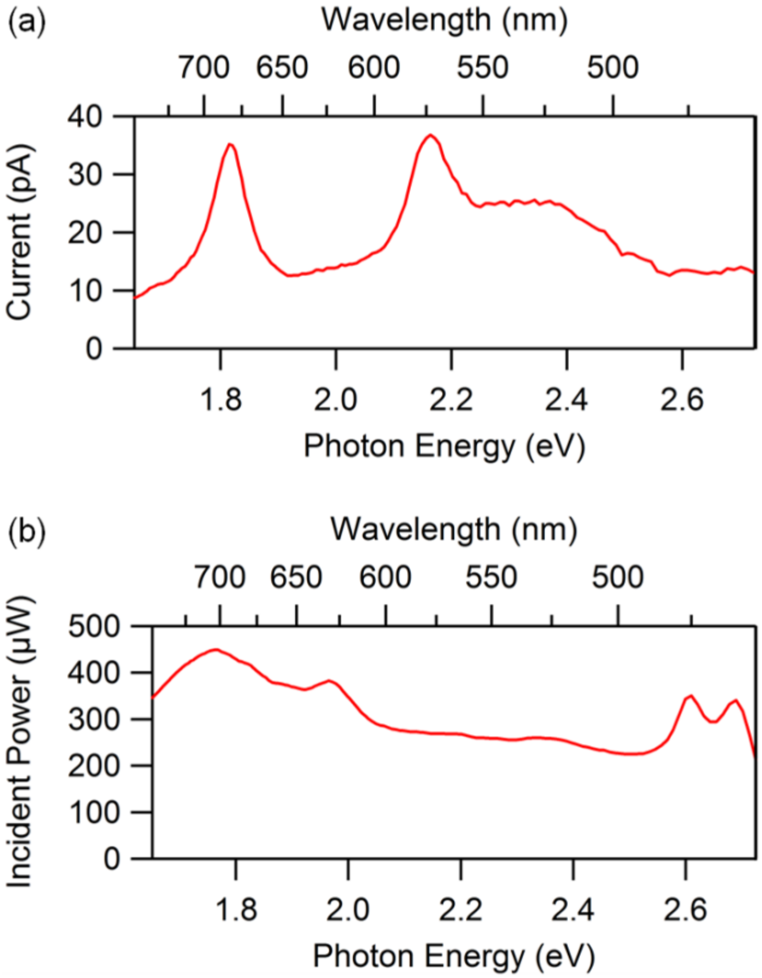

Figure 3.7. Spectral dependence of suspended CNT FET. (a) Measured change in current as photon energy is varied. (b) Power incident to sample as a function of photon energy.

Resonant photoconductivity of a semiconducting CNT was previously measured by Freitag et al. The authors observed peaks in the range 1.3-1.45 eV which they assigned to the E_{22} transition since the average diameter of these nanotubes was approximately 1.3 nm.[13] Similarly, we tentatively assign the resonances measured in our device to the E_{33} and E_{44} transitions in a CNT of diameter approximately 2.0 nm. The less intense, broad feature 200 meV above the 2.17 eV peak is likely related to a phonon-coupled transition.[20]

3.4 Conclusion

We have described our newly constructed a SPCM instrument that is capable of micron resolution imaging across a wide spectral range. Preliminary results demonstrate both spatial and spectral characterization of nanoscale optoelectronic devices. SPCM imaging on surface bound CNTs illustrates the challenges associated with hysteretic effects. A photoconductivity measurement of a suspended CNT FET shows resonances near 1.82 eV and 2.17 eV. Promising directions for future research include chirality assignment of the CNTs in FET devices and studies of the wavelength dependent efficiency of photocurrent generation in CNT and graphene photodiode devices.

3.5 Acknowledgment

Acknowledgment is made to the Donors of the American Chemical Society Petroleum Research Fund for the support of this research. Additional support for this work was provided by the Oregon Nanoscience and Microtechnology Institute (ONAMI). Sample fabrication was performed at the Cornell node of the National Nanofabrication Infrastructure Network, which is supported by the National Science Foundation (Grant ECS-0335765). We thank Nathan Gabor, Xiaodong Xu, and Jiwoong Park for several useful discussions.

3.6 References

1 Avouris, P., Freitag, M. & Perebeinos, V. Carbon-nanotube photonics and optoelectronics. *Nat Photonics* **2**, 341-50 (2008).

2 Xia, F. N., Mueller, T., Lin, Y. M., Valdes-Garcia, A. & Avouris, P. Ultrafast graphene photodetector. *Nat Nanotechnol* **4**, 839-43 (2009).

3 Mueller, T., Xia, F. N. A. & Avouris, P. Graphene photodetectors for high-speed optical communications. *Nat Photonics* **4**, 297-301 (2010).

4 Gabor, N. M., Zhong, Z., Bosnick, K., Park, J. & McEuen, P. L. Extremely efficient multiple electron-hole pair generation in carbon nanotube photodiodes. *Science (New York, N.Y.)* **325**, 1367-71, doi:10.1126/science.1176112 (2009).

5 Balasubramanian, K. *et al.* Photoelectronic transport imaging of individual semiconducting carbon nanotubes. *Appl Phys Lett* **84**, 2400-2 (2004).

6 Freitag, M. *et al.* Scanning photovoltage microscopy of potential modulations in carbon nanotubes. *Applied Physics Letters* **91**, doi:Artn 031101 Doi 10.1063/1.2757100 (2007).

7 Ahn, Y., Dunning, J. & Park, J. Scanning photocurrent imaging and electronic band studies in silicon nanowire field effect transistors. *Nano Lett* **5**, 1367-70 (2005).

8 Freitag, M. *et al.* Imaging of the schottky barriers and charge depletion in carbon nanotube transistors. *Nano Lett* **7**, 2037-42 (2007).

9 Ahn, Y. H., Tsen, A. W., Kim, B., Park, Y. W. & Park, J. Photocurrent imaging of p-n junctions in ambipolar carbon nanotube transistors. *Nano Lett* **7**, 3320-3 (2007).

10 Xia, F. N. *et al.* Photocurrent Imaging and Efficient Photon Detection in a Graphene Transistor. *Nano Lett* **9**, 1039-44, doi:Doi 10.1021/Nl8033812 (2009).

11 Park, J., Ahn, Y. H. & Ruiz-Vargas, C. Imaging of photocurrent generation and collection in single-layer graphene. *Nano Lett* **9**, 1742-6, doi:10.1021/nl8029493 (2009).

12 Lee, J. U. Band-gap renormalization in carbon nanotubes: Origin of the ideal diode behavior in carbon nanotube p-n structures. *Physical Review B* **75**, - (2007).

13 Freitag, M., Martin, Y., Misewich, J. A., Martel, R. & Avouris, P. H. Photoconductivity of single carbon nanotubes. *Nano Lett* **3**, 1067-71, doi:Doi 10.1021/Nl034313e (2003).

14 Prisbrey, L., DeBorde, T., Park, J., Yong & Minot, E. D. Controlling the Function of Carbon Nanotube Devices with Re-writable Charge Patterns. *Applied Physics Letters* **99** (2011).

15 Mohite, A., Lin, J. T., Sumanasekera, G. & Alphenaar, B. W. Field-enhanced photocurrent spectroscopy of excitonic states in single-wall carbon nanotubes. *Nano Lett* **6**, 1369-73, doi:Doi 10.1021/Nl060333f (2006).

16 Lee, J. S. *et al.* Origin of gate hysteresis in carbon nanotube field-effect transistors. *J Phys Chem C* **111**, 12504-7, doi:Doi 10.1021/Jp074692q (2007).

17 Kim, W. *et al.* Hysteresis caused by water molecules in carbon nanotube field-effect transistors. *Nano Lett* **3**, 193-8 (2003).

18 Muoth, M. *et al.* Hysteresis-free operation of suspended carbon nanotube transistors. *Nat Nanotechnol* **5**, 589-92, doi:Doi 10.1038/Nnano.2010.129 (2010).

19 Sharf, T., Kevek, J. W. & Minot, E. D. in *Nanotechnology (IEEE-NANO), 2011 11th IEEE Conference on.* 122-5.

20 Qiu, X. H., Freitag, M., Perebeinos, V. & Avouris, P. Photoconductivity spectra of single-carbon nanotubes: Implications on the nature of their excited states. *Nano Lett* **5**, 749-52, doi:Doi 10.1021/Nl050227y (2005).

CHAPTER 4

Photoconductivity Resonances in Suspended Semiconducting Carbon Nanotube Field-Effect Transistors

T. DeBorde, Lee Aspitarte, T. Sharf, J. W. Kevek, and E. D. Minot

In preparation, 2014

4.1 Introduction

Carbon nanotubes (CNTs) are a promising platform for future optoelectronic applications.[1] The absorption resonances of a CNT depend on its diameter and chirality. Due to the variety of different CNT structures, these resonances span the entire visible range,[2] offering a wide tunability for photodetection and solar energy harvesting. However, the variability of CNT properties also presents an obstacle. It is difficult to obtain chirally pure CNTs, and therefore difficult to optimize device performance. The ability to identify CNT chirality can enable refinement of growth specificity and the investigation of structure-property relationships; two important necessities for making CNTs a viable material in future applications.

Optical techniques based on Raman and Rayleigh scattering, polarization-based microscopy, and spatially-modulated spectroscopy have been developed to identify the chiral structure of individual CNTs.[3-8] Optoelectronic techniques have also been developed to determine the chiral structure of CNTs in pn junction devices. These techniques require minimal optical systems, but the pn junction device configuration is challenging to fabricate. In this work, we demonstrate that optoelectronic chiral identification can be achieved using a simpler device geometry. We use a scanning photocurrent microscope to measure the resonances in the photoconductivity of CNT field-effect transistors (FETs).

The first spectrally-resolved photoconductivity investigations of CNTs used near IR wavelengths (750 – 1000 nm) and investigated CNT FETs that were buried in silicon oxide.[9] These measurements demonstrated sharp photoconductivity resonances, but were not sufficient for chiral identification. Moreover, the photoconductivity resonances of dielectric-buried CNTs will differ from CNTs in vacuum.[10] Here we use a wide spectral range to study suspended CNTs (no dielectric coating). We compare our measured photoconductivity resonances to Rayleigh scattering resonances that have been measured from suspended CNTs.[6]

4.2 Methods

Fabrication of the devices used in this work has been described in detail previously by Sharf *et al.*[11] Devices are fabricated on Silicon wafers (p^+) with one micron of thermally grown oxide. Platinum/Titanium electrodes (100/1 nm) are created using standard photolithography techniques. Reactive ion etching is used to produce a trench between the source-drain electrodes (~1 μm in width) with the electrode layer acting as a shadow mask during the etching process.

After creating the electrodes and trench, windows are patterned on the source/drain electrodes for deposition of the CNT growth catalyst. Electron beam physical vapor deposition is used to put down the iron catalyst pads and supporting layers (Fe/SiO2/Ti, 1/20/1 nm). The final fabrication step is a fast-heat chemical vapor deposition growth process at 800 °C which has been shown to result in defect-free CNTs.[11]

Wavelength-resolved scanning photocurrent microscopy (SPCM) measurements are achieved using a super continuum laser (Fianium, SC-450) that is dispersed and filtered by a monochromator (Horiba Jobin-Yvon, HRMicro). Scanning and imaging are accomplished with a pair of scan mirrors (Nutfield Tech., OHF-7, QD-4000) and a 50x objective (Nikon, CFI LU BD ELWD, NA = 0.55) coupled with a confocal lens pair (Thorlabs, Achromatic doublets). Reflection images are recorded by measuring the reflected light intensity with a silicon photodetector (Thorlabs, PDA 100A). An instrument schematic and detailed description of the microscope can be found in ref. 12.[12]

4.3 Results and Discussion

Figure 4.1 shows a typical suspended CNT FET. A total of 13 such devices were characterized for this study. All 13 devices have transport properties consistent with semiconducting CNTs with band gaps ≥ 0.5 eV. Figure 4.1b shows the transistor curve for device 1 with on and off state transport regimes corresponding to a p-type device. Catalyst density and growth parameters have been tuned to result on average with one CNT connecting the source-drain electrodes (Figure 4.1a). Scanning electron microscopy imaging is done after photocurrent measurements to avoid contamination. The number of connected CNTs is initially determined with SPCM imaging which neither dirties nor damages the device.

An SPCM image of device 1 is shown in Figure 4.1c and d. Figure 4.1c is the reflection image of the device that shows the source-drain electrodes, the trench channel etched into the silicon oxide, and the catalyst deposited on the right electrode which scatters light away from the photodetector. From the reflection image, the full-width at half-maximum (fwhm) of the laser spot is estimated to be 600 nm. The photocurrent image, Figure 4.1d, shows two strong spots of opposite polarity surrounded by fainter semi-circle halos. The strong spots are caused by a combination of photovoltaic and photothermoelectric (PTE) mechanisms, while the fainter halos are purely thermoelectric in origin.[13] The photocurrent is measured by a current preamplifier (SRS, model SR 570) connected to the right electrode while keeping the left electrode grounded.

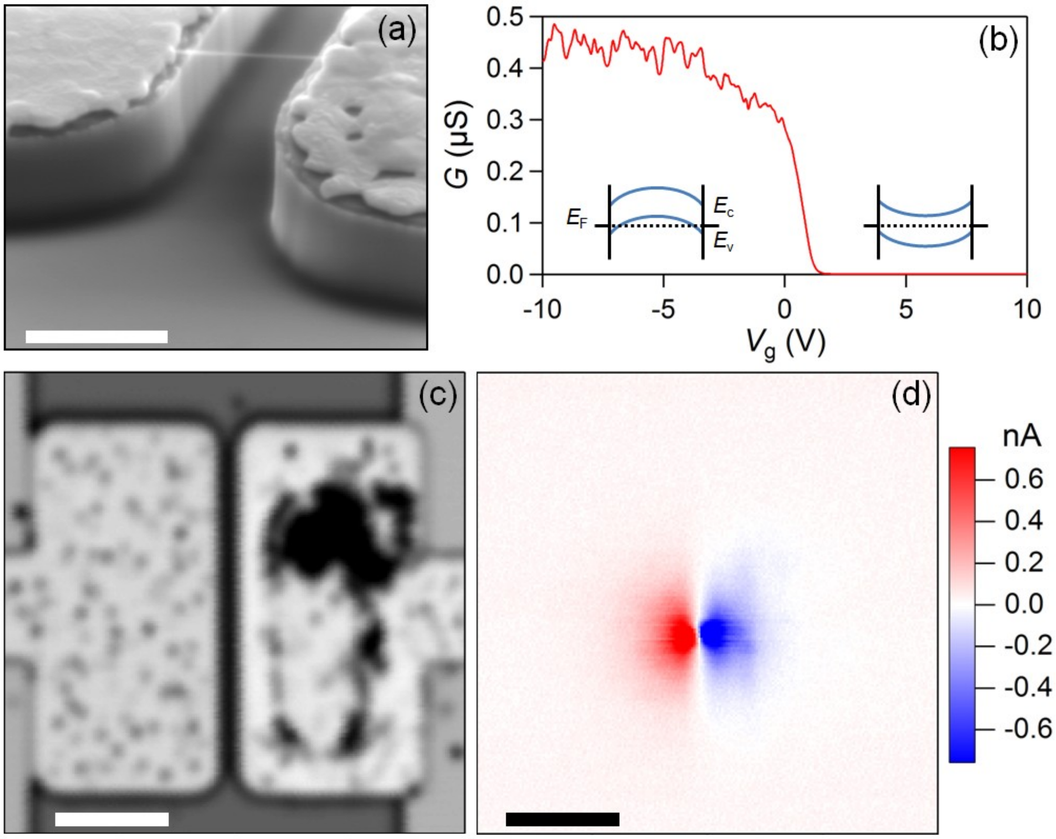

Figure 4.1. Suspended CNT FET device. (a) Scanning electron microscopy image of typical device. Scale bar is 1 μm (b) Transistor curve of conductance versus back gate voltage, V_g, of device 1. Inset cartoons show band bending diagrams for the on and off state. (c) Reflection image of device 1. (d) Photocurrent image of device 1, $V_g = 0$ V. Photocurrent is measured with a current preamplifier connected the right electrode, the left electrode is grounded. Scale bar in c and d is 5 μm.

Figure 4.2 shows three photocurrent images taken at $V_g = 8$ V, each with a different source-drain bias. Dashed lines in the images denote the positions of the electrode edges determined from the reflection data. Figure 4.2b (4.2c) show the off-state photocurrent response of device 1 with -30 mV (-70 mV) applied at the input of the current preamplifier (V_{ds}). As V_{ds} is lowered, the magnitude of the left negative photocurrent spot decreases. At -70 mV bias, only one spot of uniform polarity remains. Both the spatial size and magnitude of the right positive photocurrent response increase as V_{ds} is decreased. Symmetric trends are seen when V_{ds} is raised above zero. To learn more about the off-state photocurrent dependence on applied bias, we analyze bias dependent cross sections of the SPCM images in Figures 4.2a-c.

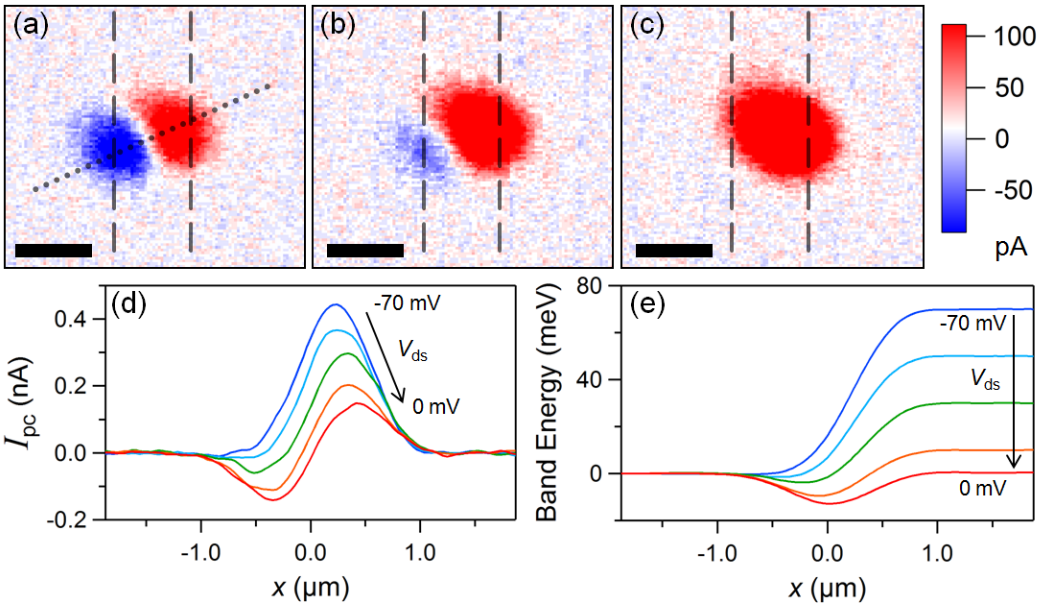

Figure 4.2. Off-state SPCM images of device 1. Photocurrent is measured with a current preamplifier connected the right electrode while varying the potential offset at the input (V_{ds}). The left electrode is grounded. Dashed lines in the images represent electrode edges. (a) SPCM image of device 1 at $V_g = 8$ V with $V_{\mathrm{ds}} = 0$. (b) SPCM image of device 1 at $V_g = 8$ V and $V_{\mathrm{ds}} = -30$ mV. (c) SPCM image of device 1 at $V_g = 8$ V and $V_{\mathrm{ds}} = -70$ mV. Scale bar in (a)-(c) is 1 μm. (d) Line graphs corresponding to the dotted line in (a) with decreasing V_{ds}. From the top right peak (blue trace) to the bottom right peak (red trace) V_{ds} is -70 mV, -50 mV, -30 mV, -10 mV, and 0. (e) Profiles of the electron band energy calculated by

integrating the V_{ds}-dependent line graphs from (d). Band energy profiles have been scaled based on V_{ds}.

Figure 4.2d shows profiles of the photocurrent spots measured along the dotted line in Figure 4.2a at different values of V_{ds}. The edges of the electrodes correspond to ±0.5 μm; the photocurrent beyond the edges is due to the spatial extent of the laser spot. The peak value of the positive photocurrent shows a linear increase as V_{ds} is lowered. The cross sections illustrate the evolution the photocurrent spots as the magnitude of the source-drain bias is increased: a shift from a symmetric pair of opposite polarity spots to a single large spot. For photovoltaic photocurrent generation, this should correspond to the emergence of a single dominant electric field along the CNT channel.

Thermoelectric-driven currents are suppressed at $V_{\mathrm{g}} = 8$ V because the FET is gated into the off-state (high resistance state).[14] Therefore, we can calculate the band bending profiles in the CNT based on the spatial dependence of the photocurrent.[15,16] Figure 4.2e shows the results of integrating the V_{ds}-dependent photocurrent cross sections measured along the CNT channel from Figure 4.2d. The band energy axis has been scaled using the values of the applied bias. The apparent band bending beyond the electrode edges (±0.5 μm) is a result of the finite laser spot. We interpret the profiles in Figure 4.2e as V_{ds}-dependent, resolution-limited estimates of the electron energy band bending along the CNT channel.

The $V_{\mathrm{ds}} = 0$ profile (bottom red trace) in Figure 4.2e is consistent with the off-state band bending diagram where the positive back gate voltage lowers the conduction and valence bands. Band banding near the electrodes will separate photoexcited charge carriers in opposite directions as seen in Figure 4.2a. As the magnitude of V_{ds} is increased, the band bending near the contacts is overwhelmed by the source-drain potential. At high V_{ds}, charge carriers that are photoexcited along the CNT channel will all be swept out of the CNT in the same direction.

The off-state, high-bias measurement configuration (Figure 4.2c) is particularly useful for characterizing CNT optoelectronic properties. First, the thermoelectric effect from illuminating the electrodes no longer contributes to the measured photocurrent. Second, fluctuations in the background "dark current" are significantly reduced by operating in the high resistance off state. Third, with a sufficient V_{ds}, the spatially-averaged photocurrent is a large, non-zero value unlike the zero-bias case. This uniform response allows for simple defocused measurements with a large laser spot.

Figure 4.3a shows a spectrally-resolved photoconductivity measurement from device 2. The data in Figure 4.3a (red circles) is measured while the device is in the off state and $V_{\mathrm{ds}} = 250$ mV. The resonant feature is fit (solid line) with a Lorentzian peak plus a linear background (blue dashed line). The resonant peak is located near 1.73 eV and has a line width of 76 meV. The line width of this peak is similar to the line widths for photocurrent resonances reported previously (~60-100 meV).[9,17,18] Figure 4.3b shows the laser power dependence of the photoconductivity on resonance. In this power range the data displays a linear dependence on incident laser power. As an additional check, the photoresponse displays strong polarization dependence both on and off resonance. This dependence is consistent with the polarization dependent CNT absorption cross-section.[19]

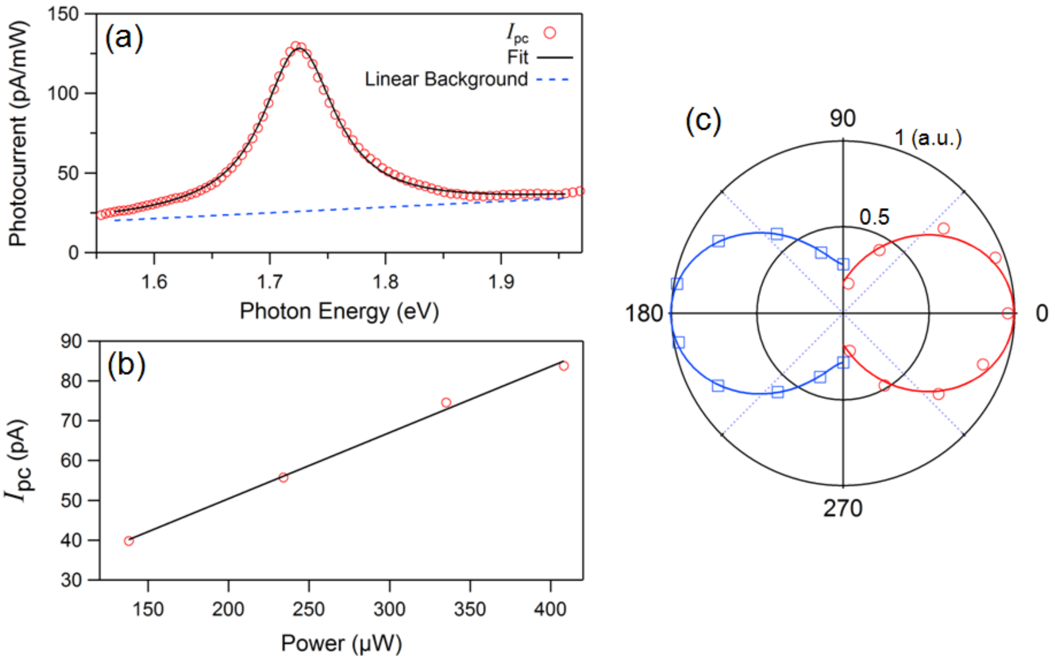

Figure 4.3. Spectrally-resolved photoconductivity. Photocurrent is measured in the off state (V_g = 8 V) at high bias (250 mV). (a) Spectrally-resolved photoconductivity data measured from Device 2. Measured photocurrent is normalized by incident laser power measured at the sample position. Data is shown as red circles and is fit (solid line) with a Lorentzian peak plus a linear background (blue dashed line). The line width of the peak is 76 meV. (b) Photocurrent versus incident laser power measured at the resonant photon energy, 1.72 eV. (c) Polarization dependence comparison between the off-state, high-bias photoresponse on resonance and the off-state, zero-bias photoresponse of a single photocurrent spot. On resonant data, taken at 1.72 eV, is plotted as red circles and off resonant data, taken at 1.96 eV (633 nm), is plotted as blue squares. The polarization data have both been normalized to have a maximum value of one.

The optical resonances in CNTs are associated with the creation of excitons.[20] Systematic mapping of exciton resonances to CNT chiral index has lead to an “atlas” of CNT resonances.[6] Therefore, accurate measurement of 2 or more optical resonances is typically sufficient to identify the chiral index of a CNT. In this work, we assign the measured photoconductivity resonances to excitonic transitions in the CNT. For the energy ranges we investigate, ~1.4 – 2.7 eV, we associate measured peaks with the E_{33}, E_{44}, E_{55}, and E_{66} exciton resonances.

Figure 4.4a shows the spectrally-resolved photoconductivity of device 3 taken in the high-bias off-state configuration. The measured photocurrent has been normalized with the wavelength dependent laser power measured at the sample. See supporting information for photoconductivity spectra of additional CNT FET devices. The data, shown as red circles in Figure 4.3a, is fit (solid line) with a combination of Lorentzian functions plus a constant baseline (blue dashed line). The measurement reveals multiple distinct resonant peaks in photoconductivity which can be distinguished based on magnitude and fwhm. There are three large resonant peaks that appear in Figure 4.3a near 1.45 eV, 1.92 eV, and 2.3 eV. In addition, there are three smaller satellite peaks positioned approximately 200 meV in energy above the stronger peaks. A better fit to the peaks is possible with a slightly varying baseline. This variation in the background photoconductivity may be a result of the duration of the measurement which takes place over approximately ten minutes.

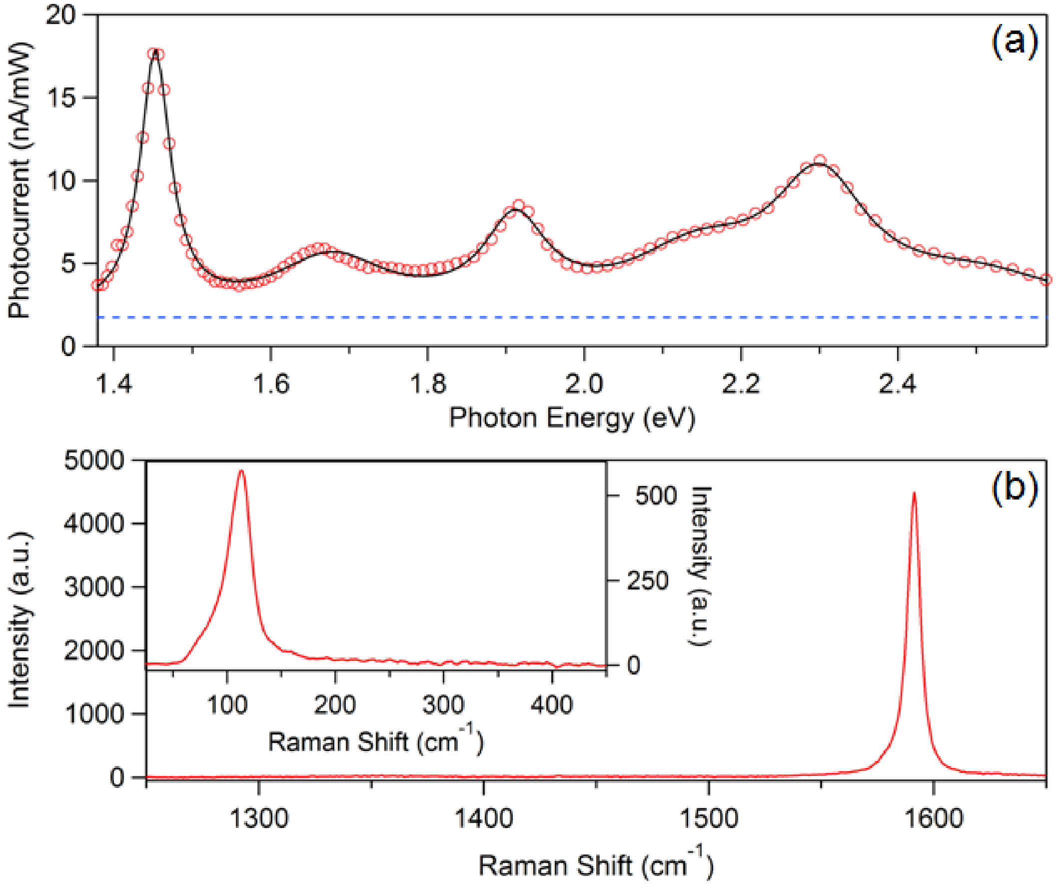

Figure 4.4. Spectrally-resolved CNT photoconductivity and Raman shift. (a) Photoconductivity of device 3 measured as a function of incident photon energy. Photocurrent is normalized by the laser power spectrum measured at the sample. Data is shown as circles. The fit to the data (solid line) is comprised of Lorentzian functions plus a constant baseline (blue dashed line). (b) Raman shifts from device 3. Excitation wavelength used was 532 nm (2.33 eV). Main graph shows Raman *G*-band near 1600 cm^{-1}. Inset graph shows the radial breathing mode of the CNT, ω_{RBM} = 112 cm^{-1}. Main graph shows no evidence of the *D*-band near 1350 cm^{-1}.

Comparing the locations of the photoconductivity resonances to existing CNT spectral data measured *via* Rayleigh scattering by Liu *et al.*, we assign the three large peaks in Figure 4.3a to the E_{33} (1.45 eV), E_{44} (1.92 eV), and E_{55} (2.3 eV) transitions.[6] From this comparison we assign a chiral index of (26,10) to the CNT in device 3. Satellite peaks seen ~200 meV above CNT resonances have been reported previously and have been explained as phonon sidebands (PSBs).[17,21] Theoretical calculations indicate these additional peaks originate from dual excitation of an exciton and an optical phonon.[22] The consistent presence of satellite peaks ~200 meV above each large peak is good indication that the measured resonances correspond to exciton creation and PSB transitions.

The fwhm linewidths of the resonant features in Figure 4.4a can be extracted from the Lorentzian fits. For both the main E_{ii} and PSB transitions, the size of the linewidth increases with increasing photon energy. This trend is consistent among all measured CNT FET devices (see supporting information). The linewidths of the E_{33}, E_{44}, and E_{55} peaks in Figure 4.4a are approximately 50, 70, and 150 meV, respectively. A strong energy dependence of the E_{22} linewidth has previously been observed in photoluminescence experiments.[23] Hertel et al. attributed the decay mechanism of the E_{22} excitons to optical phonon emission. This decay pathway is very fast, with lifetimes $\leq$ 50 femtoseconds.[24,25] Consistent linewidth vs. energy dependence has also been measured for the E_{11} and E_{22} excitons *via* photoconductivity experiments with suspended CNT based pn junctions.[18]

The linewidths of the E_{33} and E_{44} resonances in Figure 4.4a are smaller than previous E_{22} resonant photoconductivity linewidths, 90-100 meV, measured from surface-based CNT FETs.[9,17] Blancon et al., have reported CNT absorption cross-sections of the same CNT from suspended and SiO_2 supported regions, demonstrating a significant increase in linewidth for the substrate-bound section.[8] Photoluminescence measurements have shown that surface interactions enhance non-radiative decay pathways.[26] The narrower linewidths reported here are consistent with our suspended device structure. In addition to the substrate, CNT doping can influence the resonant linewidth. In recent polarization-based microscopy measurements, linewidths were broadened as the CNT was moved to higher doping levels through application of a back gate voltage. In our measurement configuration the CNT is gated into the off state, leaving it effectively undoped along the channel.

To corroborate the resonance-matching chiral assignment, we measured the resonant Raman spectrum of device 3. Raman excitation experiments were only possible with a limited number of laser wavelengths, which prohibited similar resonant Raman spectroscopy for the majority of our measured devices. Of particular interest is the radial breathing mode frequency which is a sensitive measure of CNT diameter. Figure 4.4b shows Raman shifts measured from device 3. The excitation laser line for the Raman measurement was 532 nm. The main graph of Figure 4.4b shows the Raman shifts near the *D*- and *G*-bands. Chemical vapor deposition CNT growth as the final fabrication step results in pristine crystal structures,[27] consistent with the absence of the *D*-band. The inset graph, at smaller Raman shifts, shows the measured radial breathing mode of the CNT after subtracting the Si background. The presence of the radial breathing mode peak is good indication of the presence of a resonant transition near the excitation line, ~2.33 eV, consistent with the photoconductivity peak at 2.3 eV.

To estimate the CNT diameter we use the relation established by Meyer et al.,[28]

$$\omega_{RBM} = A / d_{CNT} + B , \quad (4.1)$$

where A = 204 cm^{-1}, B = 27 cm^{-1}, and d_{CNT} is the diameter of the CNT in nanometers. The position of the radial breathing mode in Figure 4.4b is ω_{RBM} = 112 cm^{-1}, from which we find d_{CNT} = 2.4 nm. From the (26,10) chiral index found by resonance-matching, the diameter of this CNT structure is 2.52 nm. The good agreement with the RBM diameter supports our chiral index assignment.

Figure 4.5 shows the resonant photoconductivity results from multiple suspended CNT FET devices. To characterize the accuracy of a given chiral assignment we determine a residual energy parameter, E_{res},

$$E_{\mathrm{res}}^2 = \sum_i \left(E_{ii,PC} - E_{ii,Atlas}\right)^2 , \quad (4.2)$$

where $E_{ii,PC}$ and $E_{ii,Atlas}$ refer to the measured photoconductivity peaks and the reference resonant transitions, respectively.[6] Chirality assignment requires choosing a chiral index that minimizes E_{res}. In certain cases the minimization of E_{res} is insufficient to identify a unique chiral index. In these cases, a measured pair of peaks could be decently matched to the E_{33} and E_{44} of one CNT and the E_{44} and E_{55} of another. To exclude false positive matches, additional predicted peaks of the potential matches are checked against the photoconductivity spectrums. If a predicted peak in our energy range is absent from the measured spectrum, that chiral index is eliminated as a potential match. The presence of measured low-energy PSB peaks that indicate a main transition below our energy range can also be used to eliminate false positive matches. The top panel of Figure 4.5 shows the resulting E_{res} values for the 13 measured CNT FET devices. The values are plotted against the calculated diameter of the matched chiral index. All of the measured CNTs have an E_{res} value below 35 meV with the majority of the matches below 20 meV.

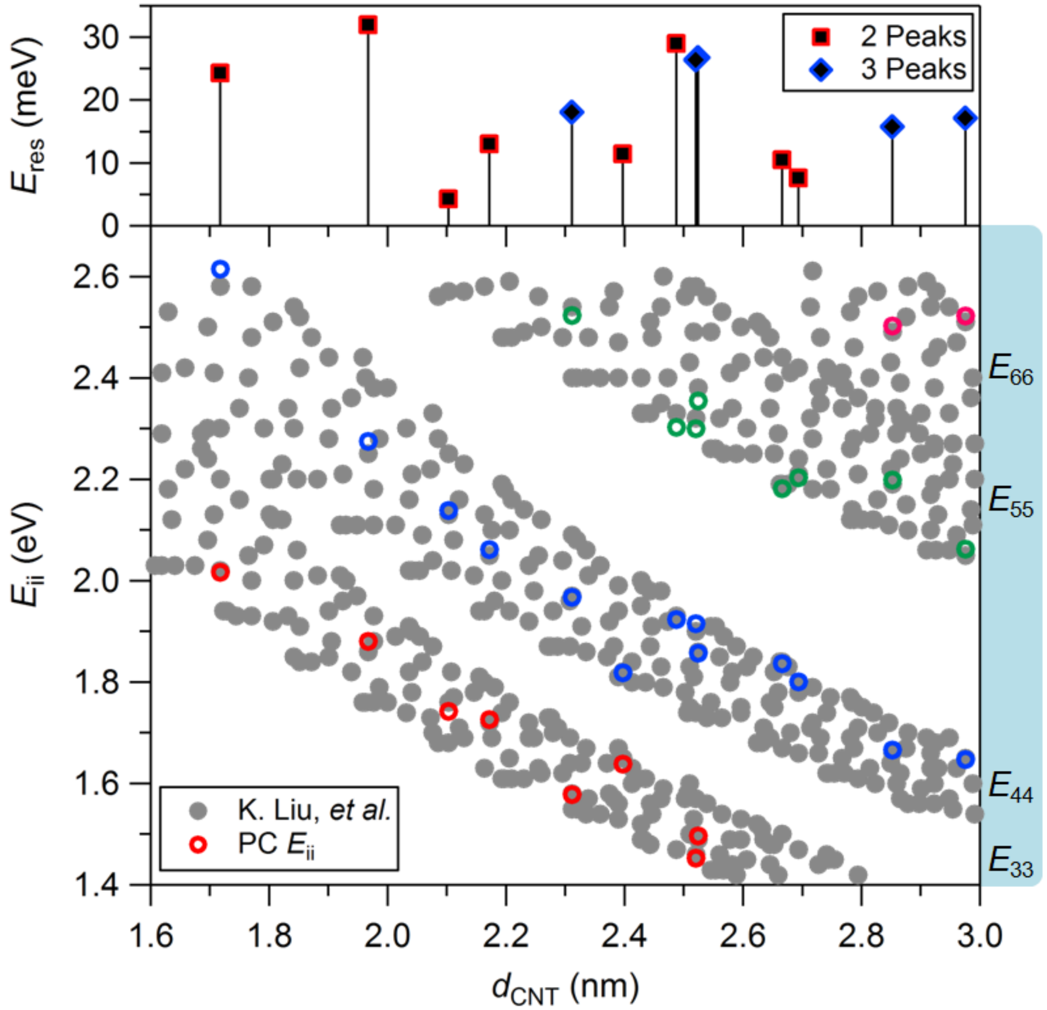

Figure 4.5. Energy residuals and CNT Kataura plot. Top panel shows energy residual parameter, E_{res}, for photoconductivity measured CNTs plotted against the diameter of the corresponding resonance-matched CNT. Photoconductivity spectrums with 2 peaks are represented with squares while spectrums with 3 peaks are shown as diamonds. E_{res} is calculated (eq. 4.2) using resonant transitions from Liu *et al*. Bottom panel shows resonant transitions from Rayleigh scattering measurements and extrapolated transition values (filled gray circles) from semiconducting CNTs with diameters between 1.6 and 3 nm. Measured photoconductivity resonances are plotted as empty, colored circles.

The bottom panel of Figure 4.5 is a Kataura plot of the measured energy of each photoconductivity resonance (empty, colored circles). The corresponding E_{res} values are shown directly above. The diameter values have been assigned using the identified chiral indices. The CNT resonances used to identify chiral indices are also plotted (filled, gray circles).[6] The transitions range from E_{33} to E_{66} as indicated on the right side of the bottom panel. The experimental range of excitation energies (1.4 – 2.7 eV) combined with the experimental range of CNT diameters allows measurements of 2 or 3 resonant peaks for a given CNT. To match a measured photoconductivity spectrum with a chiral index, we restrict ourselves to spectrums showing at least two resonant peaks.

We note the absence of smaller diameter CNTs, < 1.6 nm, in Figure 4.5. This could stem from several possibilities. First, larger diameter CNTs have been shown to have better electrical contact. Though we try to measure all possible devices, those with significant contact resistance (>5 MΩ) are difficult to extract photoconductivity spectrums from. Second, the absorption cross-section is expected to linearly increase with CNT diameter.[29,30] Third, the thickness of the electron-beam deposited Fe catalyst layer (1 nm) may favor growth of larger tubes. Previous growth experiments on quartz with 0.2 nm thick Fe catalyst layers preferentially grew single-walled CNTs with $d_{\mathrm{CNT}} \leq 1.5$ nm for the same growth parameters.[31]

Low values of E_{res}, typically ~20 meV or less, are good evidence that photoconductivity spectrums can be directly used for identifying CNT chirality. The Rayleigh scattering resonances used for chiral identification all fall within 20 meV of the predicted transition energies from an empirical equation describing the subband dependent CNT resonances.[6] If two or more resonances are measured with this level of accuracy, chiral index can be unambiguously assigned.

4.4 Conclusion

We have measured photoconductivity spectrums for suspended semiconducting CNT FETs. Back-gate and source-drain voltage dependence has been investigated *via* SPCM imaging. The spatial dependence of the photocurrent response has been used to estimate the band-bending along the CNT channel and indicates a photovoltaic photocurrent generation mechanism. Low noise measurements of wavelength dependent photocurrent stemming from CNT absorption have been made in a high-bias off-state measurement configuration. From the resulting photoconductivity spectrums, CNT chiral indices can be identified through resonance matching with existing Rayleigh scattering data. This work shows that spectrally-resolved photoconductivity is a viable avenue for chiral identification of CNTs implemented into simple FET device designs.

4.5 Supporting Information

A) Photoconductivity Spectra of CNT FET devices

Additional example photoconductivity spectra are shown in Figure 4.S1. These measurements are made in the high-bias, off-state configuration as described in the main text, though exact bias and back gate voltage values differ slightly between devices. Photoconductivity spectra are each normalized by wavelength resolved laser power measurements taken shortly after photocurrent measurements. The traces in Figure 4.S1 have been arbitrarily rescaled and offset for clarity and ease of comparison.

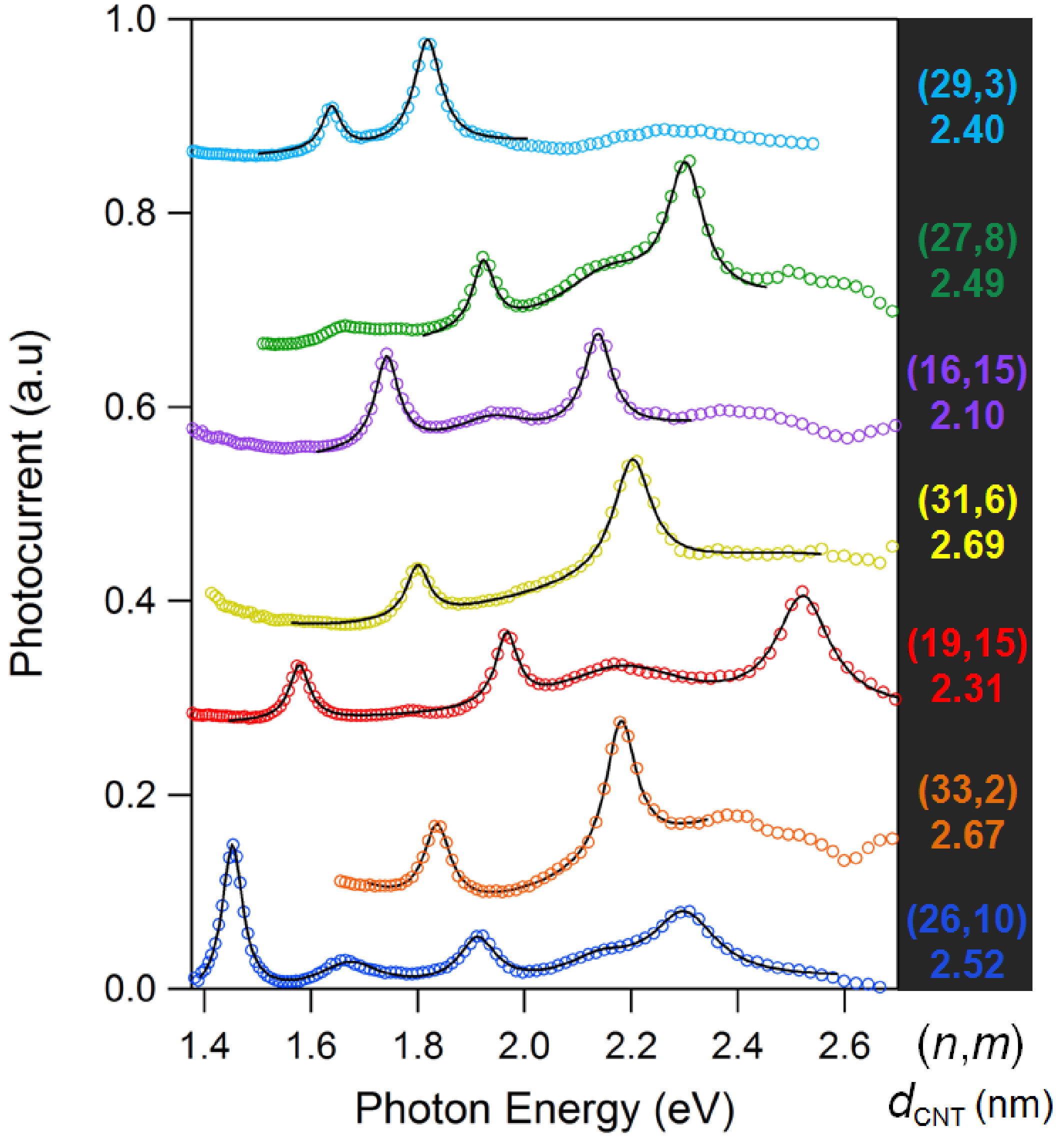

Figure 4.S1. Photoconductivity spectra of additional CNT FET devices. Photoconductivity spectra have been normalized with incident laser power spectra measured at the sample position and have also been rescaled to be plotted together. Measured data is shown as colored circles and fit by Lorentzian peaks plus linear backgrounds (black lines). Chiral index and associated CNT diameter are displayed on the right of each trace.

More work is required to investigate family type trends of the resulting spectra. Specifically trends in relative E_{ii} peak intensity and presence (absence) of phonon sideband peaks. Here we define family type following the convention mod(|n-m|,3) to distinguish type 1 and type 2 semiconducting CNTs.[32] The measured spectra are dominated by type 1 semiconducting CNTs (see Table S4.1). Further measurements are needed to determine if this trend will continue and its potential cause.

Table 4.S1. Matched photoconductivity resonance data

(n, m)	d_{CNT} (nm)	Type	E_{res} (meV)	E_{33} (eV)	E_{44} (eV)	E_{55} (eV)	E_{66} (eV)
(16,9)	1.72	1	34.2	2.016	2.614		
(15,14)	1.97	1	31.9	1.881	2.274		
(16,15)	2.10	1	19.4	1.742	2.138		
(17,15)	2.17	2	13	1.726	2.062		
(19,15)	2.31	1	18	1.578	1.967	2.522	
(29,3)	2.40	2	11.3	1.639	1.819		
(27,8)	2.49	1	27.5		1.923	2.302	
(26,10)	2.52	1	26.4	1.453	1.916	2.300	
(22,15)	2.52	1	26.7	1.497	1.857	2.355	
(33,2)	2.67	1	10.5		1.837	2.181	
(31,6)	2.69	1	7.5	1.800	2.203		
(23,19)	2.85	1	15.7		1.666	2.198	2.502
(32,10)	2.98	1	17.1		1.647	2.062	2.522

B) Lorentzian Linewidths of Photoconductivity Resonances

Figure 4.S2 shows the Lorentzian linewidths extracted from fitting each measured photoconductivity spectra (see Figure 4.S1). The resonant linewidths in each individual spectra all show an increasing dependence on transition energy. The energy dependence between different spectra however has some variation resulting in a broad overall spread in transition energy and index (E_{ii}) similar to previously reported data.[18,23] Though not a conclusive indication, peak width could potentially be used to refine the E_{ii} resonance identification process.

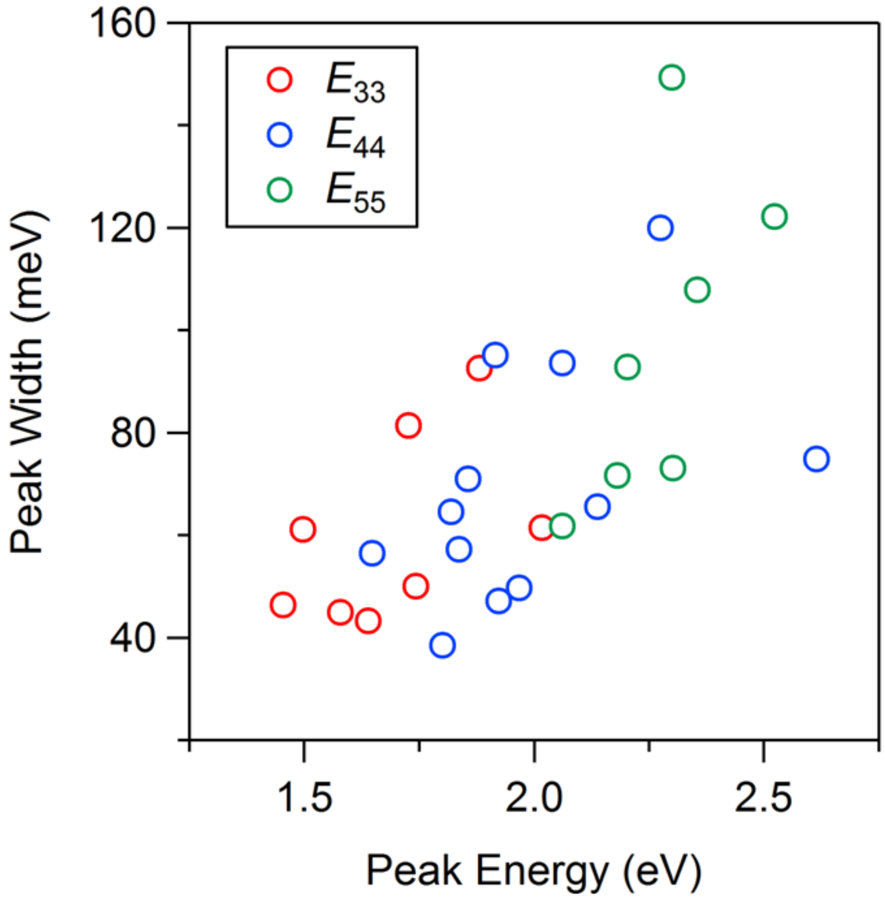

Figure 4.S2. Lorentzian linewidth versus transition energy. The graph shows fwhm linewidths plotted against resonant transition energy. Linewidths are distinguished by their transition index (E_{ii}) with colored circles.

4.6 References

1 Avouris, P., Freitag, M. & Perebeinos, V. Carbon-nanotube photonics and optoelectronics. *Nat Photonics* **2**, 341-50 (2008).

2 Kataura, H. *et al.* Optical properties of single-wall carbon nanotubes. *Synthetic Metals* **103**, 2555-8 (1999).

3 Jorio, a. *et al.* Structural (n, m) Determination of Isolated Single-Wall Carbon Nanotubes by Resonant Raman Scattering. *Physical Review Letters* **86**, 1118-21, doi:10.1103/PhysRevLett.86.1118 (2001).

4 Sfeir, M. Y. *et al.* Probing electronic transitions in individual carbon nanotubes by Rayleigh scattering. *Science (New York, N.Y.)* **306**, 1540-3, doi:10.1126/science.1103294 (2004).

5 Joh, D. Y. *et al.* On-chip Rayleigh imaging and spectroscopy of carbon nanotubes. *Nano letters* **11**, 1-7, doi:10.1021/nl1012568 (2011).

6 Liu, K. *et al.* An atlas of carbon nanotube optical transitions. *Nature nanotechnology* **7**, 325-9, doi:10.1038/nnano.2012.52 (2012).

7 Liu, K. *et al.* High-throughput optical imaging and spectroscopy of individual carbon nanotubes in devices. *Nature nanotechnology* **8**, 917-22, doi:10.1038/nnano.2013.227 (2013).

8 Blancon, J.-C. *et al.* Direct measurement of the absolute absorption spectrum of individual semiconducting single-wall carbon nanotubes. *Nature communications* **4**, 2542-, doi:10.1038/ncomms3542 (2013).

9 Freitag, M., Martin, Y., Misewich, J. A., Martel, R. & Avouris, P. H. Photoconductivity of single carbon nanotubes. *Nano Lett* **3**, 1067-71, doi:Doi 10.1021/Nl034313e (2003).

10 Perebeinos, V., Tersoff, J. & Avouris, P. Scaling of excitons in carbon nanotubes. *Physical Review Letters* **92**, doi:Artn 257402 Doi 10.1103/Physrevlett.92.257402 (2004).

11 Sharf, T., Kevek, J. W., DeBorde, T., Wardini, J. L. & Minot, E. D. Origins of Charge Noise in Carbon Nanotube Field-Effect Transistor Biosensors. *Nano Lett* **12**, 6380-4, doi:Doi 10.1021/Nl303651t (2012).

12 DeBorde, T., Kevek, J. W., Sharf, T., Wardini, J. L. & Minot, E. D. in *Nanotechnology (IEEE-NANO), 2011 11th IEEE Conference on.* 382-6.

13 DeBorde, T., Aspitarte, L., Sharf, T., Kevek, J. W. & Minot, E. D. Photothermoelectric Effect in Suspended Semiconducting Carbon Nanotubes. *ACS Nano*, doi:10.1021/nn403137a (2013).

14 Small, J. P., Perez, K. M. & Kim, P. Modulation of thermoelectric power of individual carbon nanotubes. *Physical Review Letters* **91**, doi:Artn 256801 Doi 10.1103/Physrevlett.91.256801 (2003).

15 Freitag, M. *et al.* Imaging of the schottky barriers and charge depletion in carbon nanotube transistors. *Nano Lett* **7**, 2037-42 (2007).

16 Ahn, Y. H., Tsen, A. W., Kim, B., Park, Y. W. & Park, J. Photocurrent imaging of p-n junctions in ambipolar carbon nanotube transistors. *Nano Lett* **7**, 3320-3 (2007).

17 Qiu, X. H., Freitag, M., Perebeinos, V. & Avouris, P. Photoconductivity spectra of single-carbon nanotubes: Implications on the nature of their excited states. *Nano Lett* **5**, 749-52, doi:Doi 10.1021/Nl050227y (2005).

18 Malapanis, A., Perebeinos, V., Sinha, D. P., Comfort, E. & Lee, J. U. Quantum efficiency and capture cross section of first and second excitonic transitions of single-walled carbon nanotubes measured through photoconductivity. *Nano letters* **13**, 3531-8, doi:10.1021/nl400939b (2013).

19 Islam, M. F., Milkie, D. E., Kane, C. L., Yodh, A. G. & Kikkawa, J. M. Direct measurement of the polarized optical absorption cross section of single-wall carbon nanotubes. *Physical Review Letters* **93**, doi:Artn 037404 Doi 10.1103/Physrevlett.93.037404 (2004).

20 Wang, F., Dukovic, G., Brus, L. E. & Heinz, T. F. The optical resonances in carbon nanotubes arise from excitons. *Science (New York, N.Y.)* **308**, 838-41, doi:10.1126/science.1110265 (2005).

21 Berciaud, S. *et al.* Excitons and high-order optical transitions in individual carbon nanotubes: A Rayleigh scattering spectroscopy study. *Physical Review B* **81**, 041414-, doi:10.1103/PhysRevB.81.041414 (2010).

22 Perebeinos, V., Tersoff, J. & Avouris, P. Effect of Exciton-Phonon Coupling in the Calculated Optical Absorption of Carbon Nanotubes. *Physical Review Letters* **94**, 027402-, doi:10.1103/PhysRevLett.94.027402 (2005).

23 Hertel, T. *et al.* Intersubband decay of 1-D exciton resonances in carbon nanotubes. *Nano letters* **8**, 87-91, doi:10.1021/nl0720915 (2008).

24 Ma, Y.-Z. *et al.* Ultrafast carrier dynamics in single-walled carbon nanotubes probed by femtosecond spectroscopy. *The Journal of chemical physics* **120**, 3368-73, doi:10.1063/1.1640339 (2004).

25 Manzoni, C. *et al.* Intersubband Exciton Relaxation Dynamics in Single-Walled Carbon Nanotubes. *Physical Review Letters* **94**, 207401-, doi:10.1103/PhysRevLett.94.207401 (2005).

26 Lefebvre, J., Homma, Y. & Finnie, P. Bright Band Gap Photoluminescence from Unprocessed Single-Walled Carbon Nanotubes. *Physical Review Letters* **90**, 217401-, doi:10.1103/PhysRevLett.90.217401 (2003).

27 Kong, J., LeRoy, B. J., Lemay, S. G. & Dekker, C. Integration of a gate electrode into carbon nanotube devices for scanning tunneling

microscopy. *Appl Phys Lett* **86**, 112106, doi:Doi 10.1063/1.1883301 (2005).

28 Meyer, J. *et al.* Raman Modes of Index-Identified Freestanding Single-Walled Carbon Nanotubes. *Physical Review Letters* **95**, 217401-, doi:10.1103/PhysRevLett.95.217401 (2005).

29 Joh, D. Y. *et al.* Single-walled carbon nanotubes as excitonic optical wires. *Nat Nanotechnol* **6**, 51-6, doi:Doi 10.1038/Nnano.2010.248 (2011).

30 Verdenhalven, E. & Malić, E. Excitonic absorption intensity of semiconducting and metallic carbon nanotubes. *Journal of physics. Condensed matter : an Institute of Physics journal* **25**, 245302-, doi:10.1088/0953-8984/25/24/245302 (2013).

31 Almaqwashi, A. A., Kevek, J. W., Burton, R. M., DeBorde, T. & Minot, E. D. Variable-force microscopy for advanced characterization of horizontally aligned carbon nanotubes. *Nanotechnology* **22**, 275717- (2011).

32 Choi, S., Deslippe, J., Capaz, R. B. & Louie, S. G. An Explicit Formula for Optical Oscillator Strength of Excitons in Semiconducting Single-Walled Carbon Nanotubes: Family Behavior. *Nano Letters* **13**, 54-8, doi:Doi 10.1021/Nl303426q (2013).

CHAPTER 5

Photothermoelectric Effect in Suspended Semiconducting Carbon Nanotubes

T. DeBorde, L. Aspitarte, T. Sharf, J. W. Kevek, and E. D. Minot

ACS Nano, *accepted Dec 19, 2013*

5.1 Introduction

Nanoscale optoelectronic devices exhibit fascinating physical phenomena and are of increasing interest for applications as photodetectors and energy harvesting devices.[1-5] Recent observations include multiple electron-hole generation in carbon nanotube (CNT) pn junctions[2] and ultrasensitive bolometric detection in suspended graphene membranes.[4] Nanoscale confinement of the excited carriers in these systems strongly influences the electron transport and energy relaxation pathways responsible for these novel phenomena. For example, the photocurrent extracted from a graphene pn junction is not dominated by the photovoltaic effect (as expected for traditional semiconductor devices), but rather by a photothermoelectric (PTE) effect.[6]

Carbon nanotubes offer a unique combination of electron transport and energy relaxation pathways. The bandgap of a CNT is widely tunable *via* subtle changes in CNT diameter and chirality.[7] Strong electron-electron interactions in CNTs mean that excitons play an important role in light absorption and energy relaxation. These electron-electron interactions also lead to a strong enhancement in the impact ionization pathway for energy relaxation.[2,8]

Carbon nanotube optoelectronic devices have been studied intensively using electrically-driven light emission,[3,9] spectrally-resolved photoconductivity and photocurrent,[2,10-14] and spatially-resolved photocurrent and photoconductivity.[15-19] Previous studies of surface-bound CNT field-effect transistors (FETs) identified the photovoltaic effect as the mechanism for photocurrent generation at the metal-CNT interface.[16-18] In this work, we have investigated suspended CNT FETs. Suspended CNTs become much hotter than substrate-bound CNTs for a given amount of heat input.[20,21] Therefore, the suspended geometry should promote PTE effects.[22,23] Our measurements of suspended CNTs show that light-induced thermal gradients lead to significant currents which overwhelm photovoltaic currents in some regimes of electrostatic doping. Our measurements give new insight into the tunable and spatially inhomogeneous Seebeck coefficient of electrostatically-gated CNTs and demonstrate a new mechanism for optimizing CNT-based photodetectors and energy harvesting devices.

5.2 Methods

We fabricated devices using standard photolithography techniques. Metal electrodes (Pt/Ti, 100/1 nm thickness) sit on a 1 μm thermally-grown oxide layer atop p^+ silicon. The source-drain electrodes situated 1 μm apart, act as a shadow mask for the etching of a ~1 μm deep trench in the oxide layer. We then pattern catalyst islands of Fe (Fe/SiO_2/Ti, 1/20/1 nm) on the electrodes a few microns from the edge of the trench. CNTs are grown as the last step in the fabrication resulting in defect-free suspended carbon nanotubes.[24]

The design of our homebuilt scanning photocurrent microscope has been described previously.[25] Measurements of I_{sc} were made using SRS current preamplifier model SR 570. Measurements of V_{oc} were made using a voltage preamplifier (SRS model SR 560).

5.3 Results and Discussion

Figure 5.1a shows the geometry of our suspended CNT FET.[26] The CNT was grown on top of the Pt electrodes as the last step of the fabrication process. Raman spectra obtained from the suspended CNTs are free from defect peaks as shown in the inset of Figure 1b (in contrast to Raman spectra obtained from surface-bound CNT sections). The absence of a defect peak indicates that the suspended CNT is free from electrostatic disorder.[24] Figure 5.1b shows a typical low-bias conductance measurement of a completed suspended CNT FET (device 1) where a single CNT connects the electrodes.

The high on/off ratio of the FET (Figure 5.1b) indicates a band gap greater than about 0.5 eV. For a more accurate estimate of CNT band gap, an additional ten semiconducting CNT devices were fabricated and tested by spectrally-resolved photoconductivity measurements.[10,25] Determination of E_{33} and E_{44} resonances yielded diameters ranging from 1.9 – 2.4 nm. It is somewhat surprising that no CNTs were found with smaller diameters. However, all devices were pre-selected to have good electrical contact and it is known that metal/CNT contact improves dramatically with increasing CNT diameter.[27] We conclude that the CNTs in this study have diameters ranging from 1.9 – 2.4 nm and band gaps ranging from 0.73 to 0.58 eV.[28]

A photocurrent image of device 1 is shown in Figure 5.1c. To make this image, we raster scanned a 100 μW diffraction limited laser spot, wavelength 633 nm, across the device while recording the short-circuit current I_{sc} as a function of laser position. Electrode edges (dotted lines in Figure 5.1c) are located by measuring the reflected laser light intensity. From the reflection image, we determine the laser intensity profile follows a Gaussian point spread function with FWHM ≈ 550 nm. The photocurrent image shows strong responses where the CNT contacts the metal. A halo of photocurrent extends more than 2 μm away from each CNT-metal contact point. Similar observations of long-range signals have been reported previously.[16,17,23]

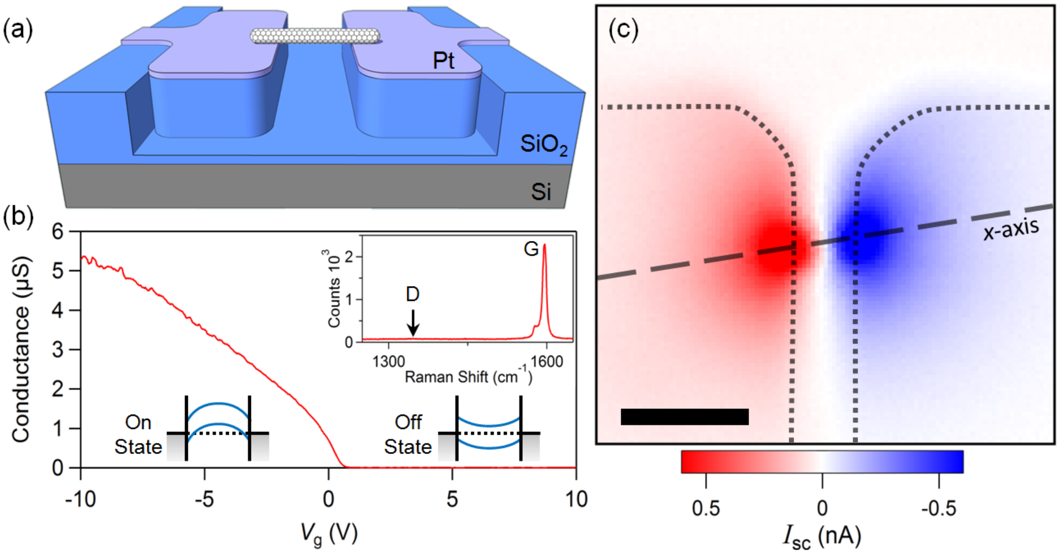

Figure 5.1. Suspended CNT FET device characteristics. (a) Diagram of suspended nanotube device. (b) Conductance measurement of device 1 taken with a 25 mV source-drain bias voltage. Inset graph shows Raman spectra from the suspended CNT. Inset diagrams show band bending for the on and off states. (c) Short-circuit scanning photocurrent image of device 1 taken with $G(V_g = 0) \approx 1$ μS. Laser power at the sample is 100 μW (λ = 633 nm). Dotted lines represent the electrode edges as measured from corresponding reflectance image (not shown). Dashed line shows CNT axis (x-axis). Scale bar is 2 μm.

To gain more insight into the photocurrent generation mechanisms, we performed line scans of laser position, x_{laser}, along the CNT axis (x-axis) at different values of V_g. The line traces in Figure 5.2a show $I_{sc}(x_{\text{laser}})$ at V_g = 0 V (in the off state) and V_g = -1.5 V (in the on state). The position x_{laser} = 0 corresponds to when the laser is centered on the middle of the trench. The color map of $I_{sc}(x_{\text{laser}}, V_g)$ shows the evolution of $I_{sc}(x_{\text{laser}})$ as a function of V_g. Understanding the features in $I_{sc}(x_{\text{laser}}, V_g)$ is the central topic of this paper.

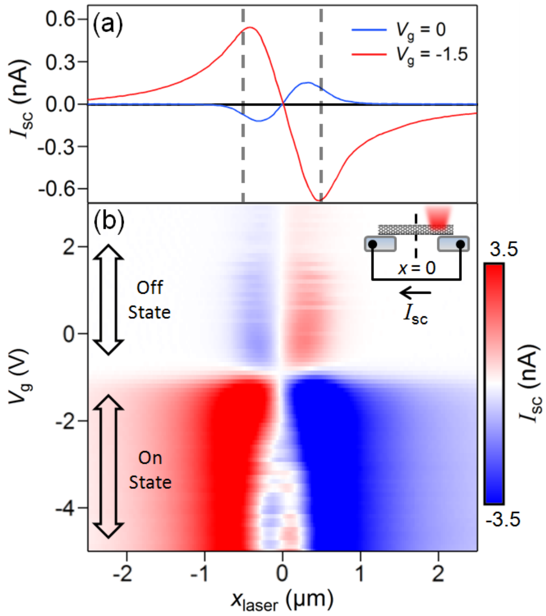

Figure 5.2. Gate-dependent line scans of device 1. (a) Line scans of I_{sc} measured in the on state (V_g = -1.5 V) and off state (V_g = 0) taken along the x-axis shown in Figure 5.1c. Vertical dashed lines in (a) indicate the position of the electrode edges. (b) Map of the gate voltage dependence of I_{sc} along the x-axis. Laser power at the sample is 120 μW (λ = 633 nm). The center of the trench is defined as x = 0. The inset diagram shows the I_{sc} measurement configuration.

When the laser spot is centered several microns from the electrode edge, the suspended CNT is not illuminated. In this case, current cannot be generated by a photovoltaic mechanism, therefore, we explore the possibility of a PTE effect. Figure 5.3 shows the open-circuit voltage $V_{oc}(V_g)$ with the laser spot centered at $x \approx 1.8$ μm (illuminating the metal electrode, but not the CNT). A peak response of V_{oc} = 250 μV is observed at V_g = 0.3 V (the threshold of the on state). The polarity of V_{oc} corresponds to a build-up of negative charge on the laser-illuminated electrode, or equivalently, a build-up of positive charge on the dark electrode. The open-circuit voltage falls to a plateau at more negative V_g and drops to near zero at positive V_g.

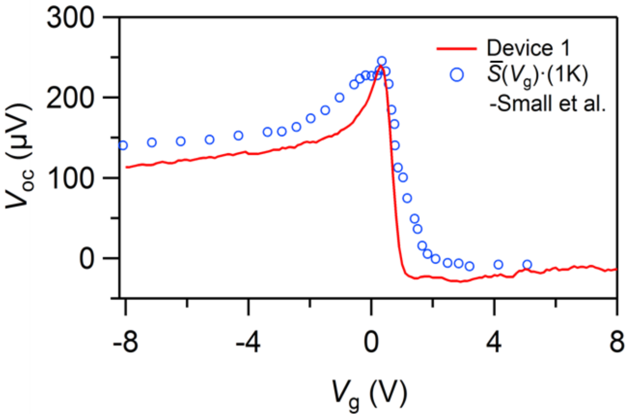

Figure 5.3. Open-circuit voltage of device 1. $V_{oc}(V_g)$ measured at x_{laser} = 1.8 μm. Open circles represent the Seebeck coefficient measurement of a semiconducting CNT from Small *et al.* re-plotted here for a temperature difference ΔT = 1 K. Small's data has been offset in V_g to match the threshold voltage of device 1.

From previous thermoelectric measurements of single-walled CNT devices,[29] we expect

$$V_{oc} = \bar{S}(V_g)\cdot\Delta T\,, \qquad (5.1)$$

where ΔT is the temperature difference across the CNT device, $\bar{S}(V_g) > 0$ is the effective Seebeck coefficient for a p-type CNT device (spatially averaged along the length of the CNT), and the Seebeck coefficient of the metal electrodes is negligible (S_{Pt}(300 K) ≈ -5 μV/K).[30] Small *et al.* used on-chip heaters and thermometers to determine $\bar{S}(V_g)$ of non-suspended semiconducting CNT devices (Figure 5.3, open circles). Small *et al.* observed a peak value of $\bar{S}(V_g)$ ≈ 250 μV/K when V_g was set to the on-state threshold.

When x_{laser} = 1.8 μm we estimate ΔT = 1 K, *i.e.* the hot end of the CNT is 1 K hotter than the cold end. We find this ΔT value *via* two independent approaches. In the first approach, we assume that the previously measured peak Seebeck coefficient, 250 μV/K, is approximately equal for surface-bound and suspended CNTs. In the second approach, we measure the temperature of a CNT on top of a Pt electrode when the CNT and Pt are illuminated by a 100 μW laser. This thermometry measurement is performed by micro Raman spectroscopy and utilizes the temperature-dependent *G*-band shift. We find a temperature rise of 2 K directly underneath the laser spot and estimate the resulting ΔT = 1 K (see supporting info).

Figure 5.3 shows a comparison between our measurement of $\bar{S}(V_g)\cdot(1\text{ K})$ and the previous measurement by Small *et al*. The data are in good agreement if one assumes a factor two difference in gate-coupling efficiency. In addition to differences in gate-coupling efficiency, a sharper peak in $V_{oc}(V_g)$ could also be caused by the absence of substrate-induced electrostatic disorder in suspended CNTs.[31]

Returning now to Figure 5.2, we can understand the gradual increase in on-state I_{sc} as the laser moves closer to the electrode edge. Scanning the laser toward the electrode edge will increase the temperature at the hot end of the CNT, thereby increasing ΔT. The observed rise in $I_{sc}(x_{laser})$ is consistent with a thermally-driven I_{sc} that tracks ΔT. The on-state ($V_g < -2$ V) photocurrent peaks at $x_{laser} \approx \pm 0.6$ μm, where the laser spot reaches the edge of the metal electrode.

As the laser begins to illuminate the CNT, light can be absorbed by both the CNT and the metal electrode. To study this mixed regime, it is helpful to identify current generated by CNT absorption as opposed to current generated by heating of the metal electrode. The absorption cross section of the CNT is known to be polarization dependent,[32] therefore, we measured $I_{sc}(V_g, x_{laser})$ with polarization either parallel (||) (Figure 5.4a) or perpendicular (⊥) to the CNT axis. Figure 5.4b shows the difference between the two laser polarization measurements $\Delta I_{sc}(V_g, x_{laser}) = I_{sc,||}(V_g, x_{laser}) - I_{sc,\perp}(V_g, x_{laser})$.

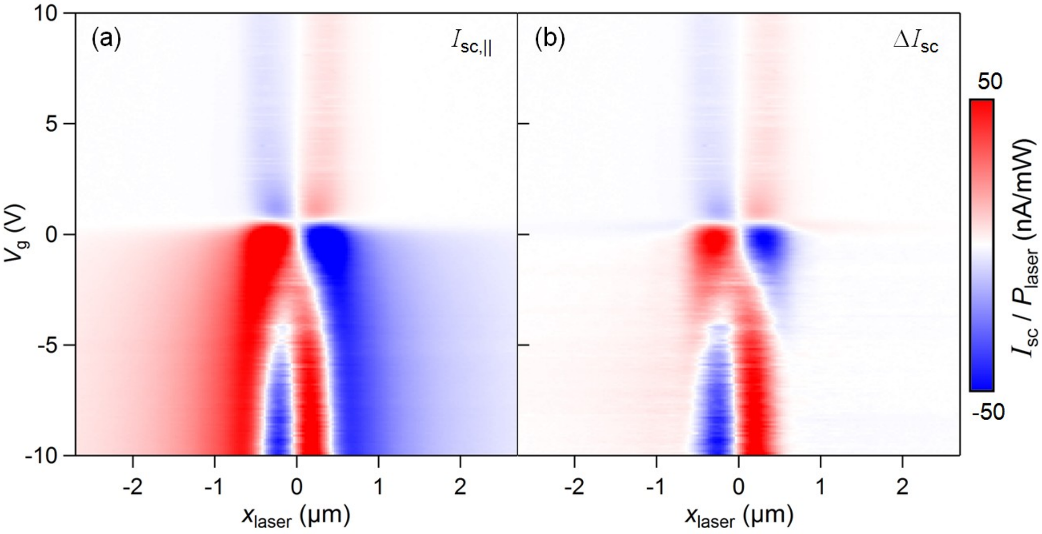

Figure 5.4. Polarization dependent photocurrent maps. (a) $I_{sc,||}(V_g, x_{laser})$ and (b) $\Delta I_{sc}(V_g, x_{laser}) = I_{sc,||}(V_g, x_{laser}) - I_{sc,\perp}(V_g, x_{laser})$ from device 2. Photocurrent values have been normalized by the incident laser power, ~ 70 μW.

Figure 5.4b shows that light absorption by the CNT also plays an important role in photocurrent generation. We first examine the off-state photocurrent, where $I_{sc,||}(V_g, x_{laser}) \approx 3.5 \cdot I_{sc,\perp}(V_g, x_{laser})$. The ratio of $I_{sc,||}$ to $I_{sc,\perp}$ is consistent with previous photocurrent polarization ratios for CNTs[11] and we conclude that $\Delta I_{sc}(V_g, x_{laser})$ corresponds to approximately 70% of the current generated by CNT light absorption. In the off state, the parallel and perpendicular polarization measurements have the same functional form, with Gaussian peaks at ±0.3 μm (FWHM = 550 nm). These observations show that heating of the metal electrode does not generate photocurrent in the off state. We conclude that the photocurrent observed in the off state is due to the photovoltaic effect, in agreement with previous measurements of surface-bound CNTs.[17,18,33]

Next we discuss ΔI_{sc} near the transition between off state and on state which occurs at $V_g \approx 0$ V for this device. Tuning V_g from the off state to the on state leads to an abrupt sign flip in ΔI_{sc} and an increase in the magnitude ΔI_{sc}. The peaks in $\Delta I_{\mathrm{sc}}(x_{\mathrm{laser}})$ remain at ± 0.3 μm. This behavior is consistent with the photovoltaic mechanism. First, the sign flip is expected from a reversal of band bending (see diagrams in Figure 5.1b). Second, the position of the peaks do not shift, indicating the mechanism is the same on both sides of the transition. Third, the change in magnitude is expected due to the asymmetry between the Schottky barriers for n-type/p-type transport. A large barrier limits the extraction of photogenerated electrons in the off-state, while a small barrier limits the extraction of photogenerated holes in the on-state. We conclude that the ΔI_{sc} signal near the on/off transition is due to the photovoltaic effect.

Deeper in the on state ($V_{\mathrm{g}} < -3$ V) there is another sign flip in ΔI_{sc}. In Figure 5.4b this is seen as the gradual emergence of peaks at $x_{\mathrm{laser}} \approx \pm 0.2$ μm which overwhelm the peaks at ± 0.3 μm. We have observed these unexpected features in all five devices measured. These anomalous photocurrent features contradict all predictions of the photovoltaic mechanism.

When light is absorbed by the CNT, hot electron-hole pairs are generated. These electron-hole pairs can contribute directly to I_{sc} *via* the photovoltaic mechanism, but they also raise the local temperature of the CNT. In our experiment, the photon energy is approximately 1.5 eV greater than the band gap. Much of this excess energy will be redistributed *via* rapid relaxation pathways such as optical phonon generation and collisions with other charge carriers, both of which occur on the 10 fs time scale.[8] We argue below that this photo-induced heating creates temperature gradients in the CNT, thereby driving PTE currents that dominate ΔI_{sc} at more negative V_{g}.

Previous authors have quantified the phonon temperature of suspended CNTs while illuminating the CNT with a focused laser.[21] The key factors determining the CNT phonon temperature are the rate that heat is delivered, the distance from the laser-heated segment to the metal electrodes, the thermal conductance of the CNT, and the thermal contact resistance at the CNT-metal contact. Based on the results of Hsu *et al.*,[21] a 100 μW laser focused on the CNT a few hundred nm from the electrode will heat the CNT by a few Kelvin. For a more accurate estimate we conducted G-band shift thermometry measurements on device 2 (Figure 5.4) and found a temperature increase at the center of the CNT of $T_{\max} - T_0 \approx 5$ K for an incident power of 100 μW where T_0 is the ambient temperature (see supporting info).

Figure 5.5 shows our proposed mechanism for the new photocurrent peaks emerging at $V_g < -3$V. The Seebeck coefficient in the CNT will be spatially inhomogeneous due to band bending (Figure 5.5a). In sections of CNT that are lightly doped, $S(x)$ will be large (on the order of 250 μV/K). In sections of CNT that are heavily doped, $S(x)$ will be small. For an inhomogeneous system, the net PTE voltage is found by calculating

$$V_{\mathrm{oc}}(x_{\mathrm{laser}}) = -\int S(x) \cdot \frac{dT(x, x_{\mathrm{laser}})}{dx} dx, \quad (5.2)$$

where $T(x,x_{\mathrm{laser}})$ is the temperature profile along the CNT for each position of the laser. For the purpose of calculations, we assume a temperature T_0 at both electrodes (ideal heat sinks) and a triangular peak in the temperature profile (see Figure 5.5b). With such a temperature profile, Eq. 5.2 predicts zero voltage if $S(x)$ is homogeneous, for example, in the flat band condition when the CNT is uniformly doped. However, Eq. 5.2 predicts a non-zero V_{oc} as $S(x)$ becomes inhomogeneous. Deep in the on state, $S(x)$ will be large near the electrodes (lightly doped sections of CNT) and small in the center of the CNT (highly doped sections of CNT). The polarity of ΔI_{sc} that we observe deep in the on state is consistent with this expected $S(x)$.

To further test this proposed mechanism we estimate $S(x)$ directly from measurements of $V_{\mathrm{oc}}(x_{\mathrm{laser}})$ (note that V_{oc} is equal to I_{sc} multiplied by the on-state resistance of the device). We utilize a relationship derived by St. Antoine *et al.* for a 1d system with uniform thermal conductivity κ, heated by a zero-width source that delivers heat at position x at a rate q.[22] For this ideal system, it is found that

$$S(x) = \frac{\kappa}{q}\frac{dV_{\mathrm{oc}}}{dx} + \bar{S}\,. \qquad (5.3)$$

The ratio q/κ can be determined from the maximum temperature rise at the center of the CNT. We find $q/\kappa \approx 20$ K/µm when laser power is 100 µW.

Figure 5.5c,d show plots of $V_{\mathrm{oc}}(x_{\mathrm{laser}})$ and the calculated $S(x)$ when $V_{\mathrm{g}} = -10$ V. The parameter $\bar{S}$ is found from earlier measurements of $\bar{S}(V_{\mathrm{g}})$ (Figure 5.3). Consistent with the expected band bending, the calculated $S(x)$ is large near the electrodes and small near the center of the CNT. The calculated $S(x)$ does not reach 250 µV/K (the peak value in Figure 5.3). However, spatial resolution is limited by the width of the laser spot and we interpret the calculated $S(x)$ as a locally-averaged value. With improved spatial resolution we would expect to reveal narrower/taller peaks in $S(x)$.

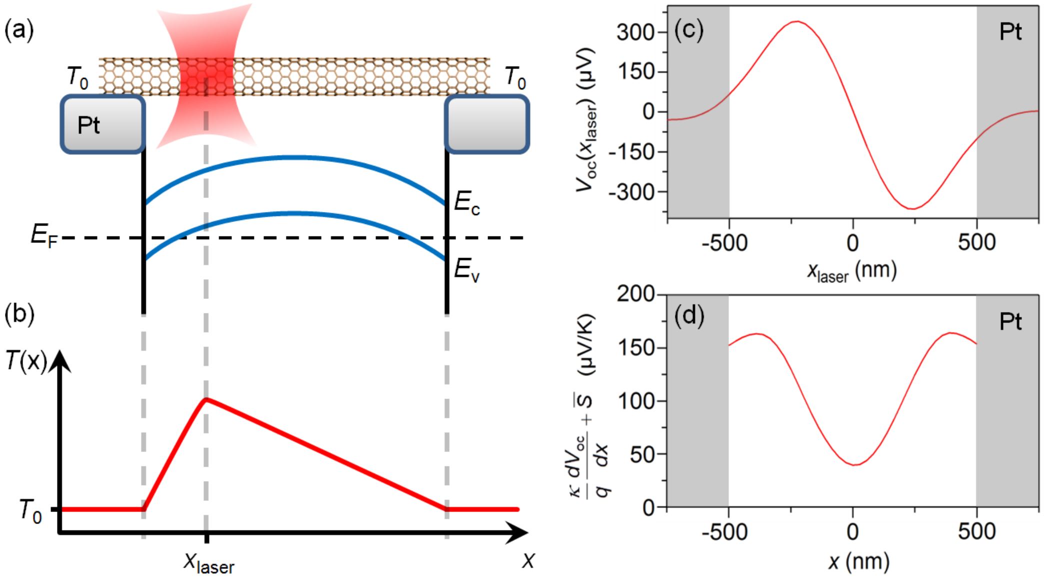

Figure 5.5. Mechanism for the on-state PTE response. (a) Cartoon of the laser-illuminated device and corresponding on-state band diagram. (b) Temperature profile due to photo-induced heating. The laser is considered to be a point source

at x_{laser}. (c) Measured $V_{\text{oc}}(x_{\text{laser}})$ at $V_g \approx$ -10 V after removing contributions from heating of the metal electrodes (Figure 5.4b). (d) The result of Eq. 5.3 calculated using V_{oc} from (c) and $\bar{S} \approx 120\ \mu\text{V/K}$.

The analysis described above could be improved by direct measurement of the electron temperature in the CNT. Raman-shift thermometry, which we use in this work, measures the phonon temperature in the CNT. However, gradients in the electron (or hole) temperature ultimately drive the PTE effect. Photoexcitation does not always heat the electron system and the phonon system equally. For example, in laser-illuminated graphene photodiodes the electron temperature is thought to differ from the phonon temperature.[6] For our CNT devices, the thermal conductivity between the free carriers and the lattice is less than the thermal conductivity from the lattice to the electrodes (see Supporting Information). Therefore, the measured phonon temperature is likely a lower bound on the temperature of the free carriers. Further work is required to establish the actual temperature of the free carriers.

In summary, the PTE mechanism explains our experimental observation of anomalous photocurrent features at $V_g <$ -3 V. Moreover, $V_{\text{oc}}(x_{\text{laser}})$ data combined with temperature calibration data can be used to estimate $S(x)$ with diffraction-limited spatial resolution.

5.4 Conclusion

We have observed evidence for both the photovoltaic mechanism and the PTE mechanism driving photocurrents in suspended CNT FETs. In the off state, the photovoltaic effect is the dominant mechanism. In the on state, laser heating of the electrodes leads to PTE voltages/currents. Utilizing this electrode heating effect, we have made the first measurement of the gate-dependent Seebeck coefficient for an ultra-clean suspended CNT. In the on state, laser heating of the

CNT also leads to PTE voltages/currents. These PTE effects dominate photovoltaic effects when band bending creates inhomogeneous $S(x)$. To quantify these PTE effects we introduced temperature calibration techniques that extend the utility of scanning photocurrent microscopy. Our findings demonstrate the critical role of light-induced heating in suspended CNT optoelectronic systems. These heating effects will play a role in optimizing CNT-based photodetectors and light-harvesting devices.

5.5 Acknowledgements

We thank George Nazin for valuable discussions. This material is based upon work supported by the National Science Foundation under Grant No. 1151369. Sample fabrication was performed at the MaSC Facility at Oregon State University and the Cornell NanoScale Facility, a member of the National Nanotechnology Infrastructure Network, which is supported by the National Science Foundation (Grant ECCS-0335765).

5.6 Supporting Information

A) Photocurrent due to CNT absorption versus Pt Absorption

Figure 5.4a of the main text shows the raw $I_{sc,||}(V_g, x)$ data measured from device 2. This data can be decomposed into a polarization sensitive contribution and a polarization insensitive contribution as shown in Fig. 5.S1.

The polarization sensitive component is related to light absorption by the CNT and is discussed in detail in the main text. The polarization insensitive component corresponds to laser heating of the Pt electrode. When the laser is close to the electrode edge, the heating effect is maximized.

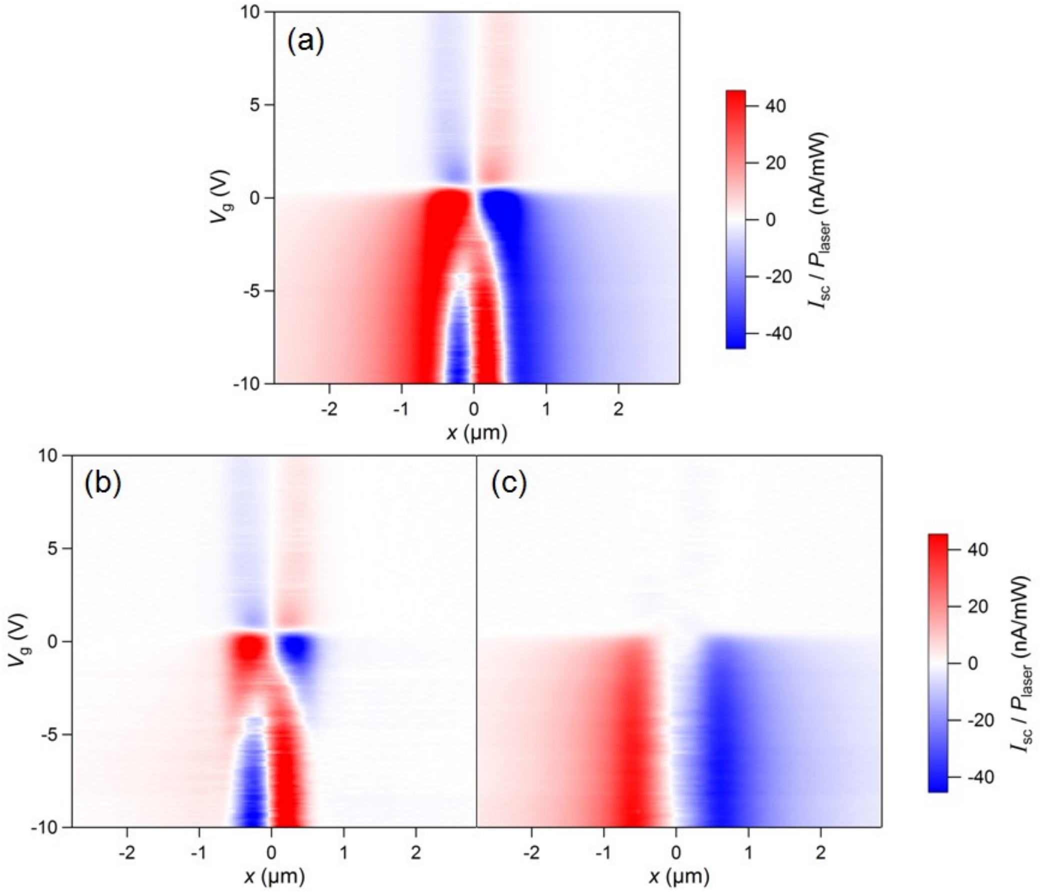

Figure 5.S1. Polarization dependent photocurrent imaging. Photocurrent from device 2 is decomposed into polarization sensitive and polarization insensitive components. (a) Raw data. (b) The polarization sensitive component of $I_{\mathrm{sc},\|}(V_\mathrm{g}, x)$. (c) The polarization insensitive component of $I_{\mathrm{sc},\|}(V_\mathrm{g}, x)$. All plots have the same color scale.

B) Temperature measurements using the Raman *G*-band

The position of the *G*-band in the Raman spectra of single-walled carbon nanotubes (CNTs) is sensitive to temperature.[34,35] We use this effect to quantify laser heating effects in our experiment. The Raman signal was excited using a 532 nm laser (Horiba Jobin Yvon, LabRAM HR 800).

We studied laser heating of both the suspended section of CNT and the section resting on the Pt electrode. For both geometries we performed a calibration experiment together with a laser heating experiment. For the calibration experiment, laser power was minimized (50 μW, λ = 532 nm, focused to a diffraction limited spot) and the temperature of the whole chip was tuned by a sample heater (Electro-Flex Heat silicon rubber heater, model # EFH-SH-1X2-5-12A). The temperature of the chip was measured with a thermocouple (Omega, model # HH802U) attached to the chip surface. For the laser heating experiment (local heating of the surface), the sample heater was turned off and incident laser power was varied. Figure 5.S2 shows representative Raman spectra measured during the calibration experiments.

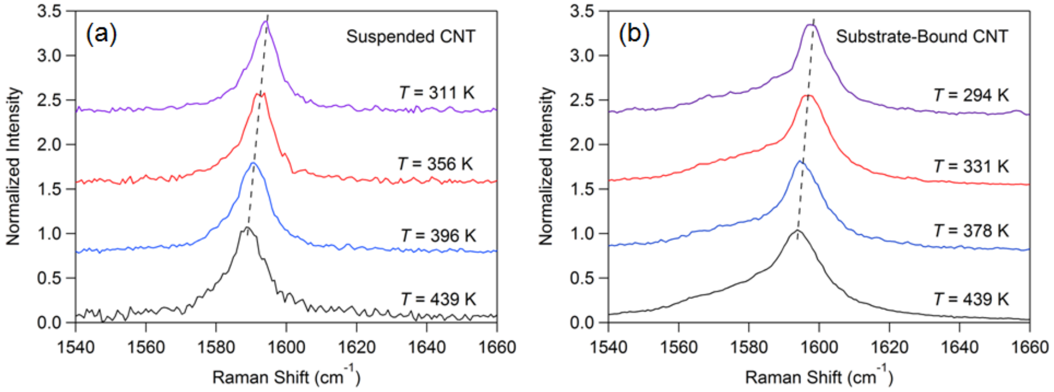

Figure 5.S2. Temperature dependent CNT Raman response. Carbon Nanotube Raman *G*-band measured at different sample-heated temperatures from suspended, (a), and substrate-bound sections, (b). Excitation laser wavelength and power was 532 nm and 50 μW, respectively.

The position of the Raman peak versus temperature for the suspended CNT is plotted in Figure 5.S3a. A linear regression gives a slope dG_{Raman}/dT = -0.0347 cm^{-1}/K, which we interpret as the calibration factor relating the suspended CNT temperature to *G*-band position.

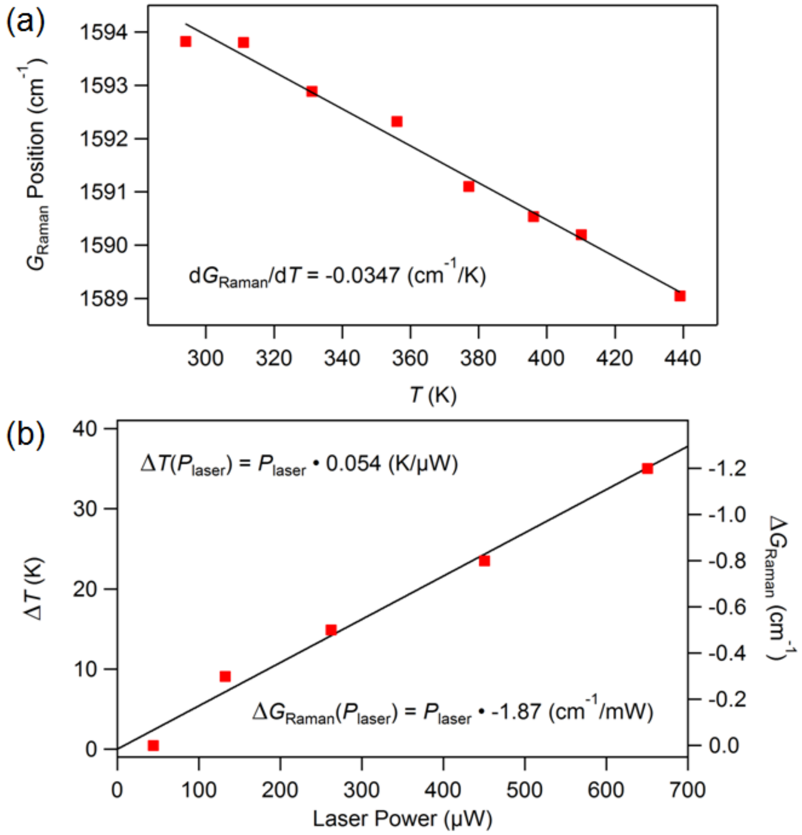

Figure 5.S3. Raman response of suspended CNT from device 2. (a) Temperature dependent measurements of *G*-band position, dG_{Raman}/dT = -0.0347 cm^{-1}/K. (b) Power dependent measurements of *G*-band position, dT/dP_{laser} = 0.054 K/μW.

After the calibration experiment, we locally heat the suspended CNT with varying laser power. Figure 5.S3b shows the position of the Raman peak versus incident laser power. On the left-hand *y*-axis, *G*-band position has been converted to ΔT using the calibration factor dG_{Raman}/dT = -0.0347 cm^{-1}/K. From this measurement we conclude that a 100 μW laser focused at the center of the suspended region leads to a temperature increase of approximately 5 K.

The position of the Raman peak versus temperature for the CNT resting on the Pt electrode is plotted in Figure 5.S4a. Measurements were performed with the laser spot centered approximately 1 μm from the edge of the trench. A linear regression yields a slope dG_{Raman}/dT = -0.0311 cm^{-1}/K, which we interpret as the calibration factor relating the CNT temperature to *G*-band position.

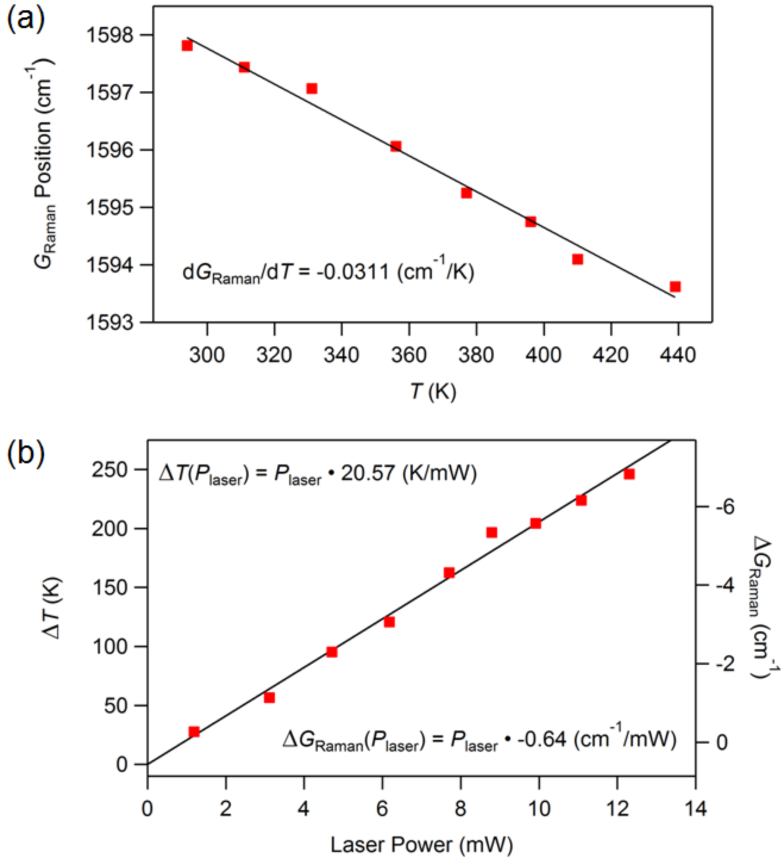

Figure 5.S4. Raman response of Pt supported CNT from device 2. (a) Temperature dependent measurements of *G*-band position, dG_{Raman}/dT = -0.0311 cm^{-1}/K. (b) Power dependent measurements of *G*-band position, dT/dP_{laser} = 20.5 K/mW.

After the calibration experiment, we locally heat the Pt electrode with varying laser power. The CNT absorption cross-section is negligible compared to the Pt absorption cross-section, however, we expect the CNT to stay in thermal equilibrium with the Pt. Figure 5.S4b shows the position of the Raman peak versus incident laser power. On the left-hand *y*-axis, *G*-band position has been converted to ΔT using the calibration factor $\mathrm{d}G_{\mathrm{Raman}}/\mathrm{d}T$ = -0.0311 cm^{-1}/K. Extrapolating to a laser power of 100 μW we conclude that light absorption by the Pt electrode leads to a temperature increase of 2 K at the center of the laser spot.

Based on the analysis above, we can expect a maximum temperature difference across the CNT of $\Delta T \approx 2$ K when a 100 μW laser spot is centered on the Pt close to one end of the CNT. If the laser spot is moved further away from the edge of the Pt electrode, ΔT will drop. The photocurrent due to Pt light absorption reaches half the peak value when $x \approx 1.8$ μm (see Fig 5.S1c). Therefore, we conclude that $\Delta T \approx 1$ K when $x = 1.8$ μm.

C) Order of magnitude calculation for laser heating of the suspended carbon nanotube

We estimate the order of magnitude temperature increase of the suspended CNT with a simple heat transport model. The laser delivers heat energy to the center of the 1 μm long suspended CNT. The heat input from the laser can be estimated using the optical absorption cross-section width, $\delta_{\mathrm{abs}} \approx (0.3)\cdot d_{\mathrm{CNT}}$,[36] the power of the incident laser and the spot size of the focused laser. We calculate approximately 140 nW of heat input for an incident laser power of 100 μW, a beam spot FHWM = 550 nm and d_{CNT} = 2 nm. The thermal conductivity of CNTs is approximately 2800 W/m·K,[37] and we assume a cross-sectional area of 2 nm^2. When the system reaches steady state, 70 nW of heat will be deposited into the left (right) electrode. Based on these assumptions we estimate the temperature in the center of the CNT, $T_{\mathrm{max}} \approx 6$ K.

D) Order of magnitude calculation for laser heating of the platinum electrode

To estimate the temperature increase of the Pt electrode due to laser heating, we consider a simple model of heat flow through our three-layer system. The substrate is composed of the 100 nm Pt electrode, a 1 µm thick layer of thermally-grown SiO_2, and a Si back plane (thickness ~ 500 µm). Light absorption by the Pt electrode at 633 nm can be calculated using Fresnel equations. For 100 nm thick Pt we expect 38% of the incident laser power to be absorbed, resulting in a heat input of 38 µW. This heat will spread in the Pt layer, but will ultimately reach the Si back plane. The thermal conductivity of SiO_2 is the main bottleneck for heat transport (k_{SiO_2} = 1.3 W/m·K). For simplification, we consider transport through of column of this structure with a cross-sectional area of 10 µm^2. In steady state, the heat flow through the SiO_2 is Q = 38 µW. This heat flow is reached when the Pt electrode is 3 K hotter than the underlying Si.

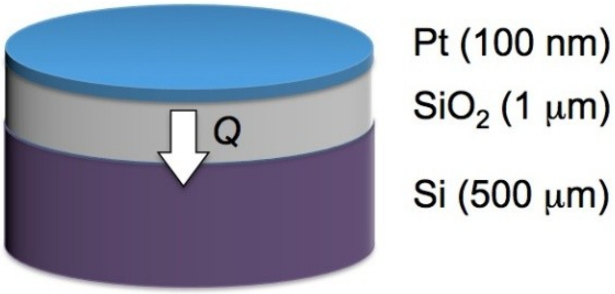

Figure 5.S5. Diagram for heat flow through electrodes. Structure for simplified model of heat transport through the Platinum electrode to the silicon back plane.

E) Phonon temperature vs. electron temperature in laser-illuminated carbon nanotube

It is possible for laser excitation to drive the electron temperature and phonon temperature out of equilibrium. To analyze this possibility, we consider a simplified thermal transport model describing the suspended CNT system (Figure 5.S6). Photon energy is initially transferred to hot photoexcited carriers. The excess kinetic energy of these hot carriers then flows to the sea of free carriers (fraction α), or to the lattice (fraction $1-\alpha$). Calculating the fraction α is challenging and is beyond the scope of this work. However, it is instructive to analyze the limiting cases $\alpha = 0$ and $\alpha = 1$.

Heat transport between the free carriers, the lattice and the electrodes can be modeled using three thermal conductances, $G_{\text{e-ph}}$, $G_{\text{e-bath}}$ and $G_{\text{ph-bath}}$, as shown in Figure 5.S6.

We estimate $G_{\text{e-ph}}$ using the phonon scattering time at room temperature $\tau_{\text{ph}} \sim 1\text{ps}$,[38] and the heat capacity of the free carriers at room temperature, $C_e = 8\pi L k_B^2 T_e/(3hv_F)$.[39] Assuming the energy relaxation time $\tau_{\text{relax}} \sim \tau_{\text{ph}}$,[40] we find $G_{\text{e-ph}} \approx 2$ nW/K.

We estimate $G_{\text{e-bath}}$ by applying the Wiedemann-Franz law to a nanoscale device following Santavicca *et al.*[40]

$$G_{\text{e-bath}} = 2\frac{\pi^2 k_B^2}{3e^2}\frac{T_{avg}}{R_C/2}, \qquad (5.\text{S}1)$$

where the first factor of two accounts for heat leaving both ends of the CNT. For our devices, the total contact resistance is $R_c \sim 200\ \text{k}\Omega$ (corresponding to $100\ \text{k}\Omega$ at each end) which yields $G_{\text{e-bath}} \approx 0.16$ nW/K.

We estimate $G_{\text{ph-bath}}$ by assuming a CNT lattice thermal conductivity of 2800 W/m·K,[37] a CNT cross-sectional area of 2 nm^2, and CNT segments of length 500 nm connected to the left and right electrodes. These approximations yield $G_{\text{ph-bath}} \approx 20$ nW/K.

The resulting thermal circuit allows us to calculate the ratio T_e/T_{ph} as a function of α. In the limiting case $\alpha = 0$ we find $T_e \approx T_{\text{ph}}$. However, in the limiting case $\alpha = 1$, we find $T_e \approx 10T_{\text{ph}}$. We conclude that the measured phonon temperature is a lower bound for the actual temperature of the free carriers.

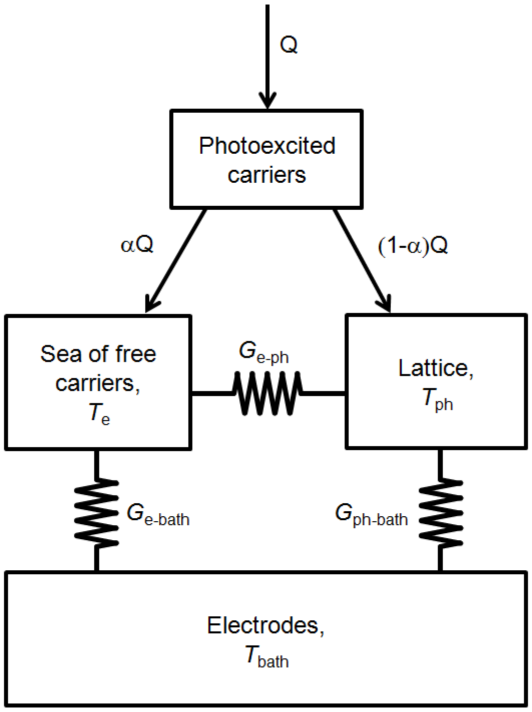

Figure 5.S6. CNT device thermal circuit diagram. Simplified thermal circuit describing laser heating of a suspended CNT.

5.7 References

1 Gabor, N. M. Impact Excitation and Electron-Hole Multiplication in Graphene and Carbon Nanotubes. *Acc Chem Res* **46**, 1348-57, doi:10.1021/ar300189j (2013).

2 Gabor, N. M., Zhong, Z., Bosnick, K., Park, J. & McEuen, P. L. Extremely efficient multiple electron-hole pair generation in carbon nanotube photodiodes. *Science (New York, N.Y.)* **325**, 1367-71, doi:10.1126/science.1176112 (2009).

3 Misewich, J. A. *et al.* Electrically induced optical emission from a carbon nanotube FET. *Science* **300**, 783-6, doi:DOI 10.1126/science.1081294 (2003).

4 Freitag, M., Low, T. & Avouris, P. Increased Responsivity of Suspended Graphene Photodetectors. *Nano Lett* **13**, 1644-8, doi:Doi 10.1021/Nl4001037 (2013).

5 Cutler, M. & Mott, N. F. Observation of Anderson Localization in an Electron Gas. *Phys Rev* **181**, 1336-&, doi:DOI 10.1103/PhysRev.181.1336 (1969).

6 Gabor, N. M. *et al.* Hot carrier-assisted intrinsic photoresponse in graphene. *Science (New York, N.Y.)* **334**, 648-52, doi:10.1126/science.1211384 (2011).

7 Bachilo, S. M. *et al.* Structure-assigned optical spectra of single-walled carbon nanotubes. *Science* **298**, 2361-6, doi:DOI 10.1126/science.1078727 (2002).

8 Perebeinos, V. & Avouris, P. Impact excitation by hot carriers in carbon nanotubes. *Physical Review B* **74**, doi:Artn 121410 Doi 10.1103/Physrevb.74.121410 (2006).

9 Chen, J. *et al.* Bright infrared emission from electrically induced excitons in carbon nanotubes. *Science* **310**, 1171-4, doi:DOI 10.1126/science.1119177 (2005).

10 Freitag, M., Martin, Y., Misewich, J. A., Martel, R. & Avouris, P. H. Photoconductivity of single carbon nanotubes. *Nano Lett* **3**, 1067-71, doi:Doi 10.1021/Nl034313e (2003).

11 Qiu, X. H., Freitag, M., Perebeinos, V. & Avouris, P. Photoconductivity spectra of single-carbon nanotubes: Implications on the nature of their excited states. *Nano Lett* **5**, 749-52, doi:Doi 10.1021/Nl050227y (2005).

12 Mohite, A., Lin, J. T., Sumanasekera, G. & Alphenaar, B. W. Field-enhanced photocurrent spectroscopy of excitonic states in single-wall carbon nanotubes. *Nano Lett* **6**, 1369-73, doi:Doi 10.1021/Nl060333f (2006).

13 Lee, J. U., Codella, P. J. & Pietrzykowski, M. Direct probe of excitonic and continuum transitions in the photocurrent spectroscopy of individual carbon nanotube p-n diodes. *Appl Phys Lett* **90**, 053103, doi:Doi 10.1063/1.2435980 (2007).

14 Barkelid, M., Steele, G. A. & Zwiller, V. Probing Optical Transitions in Individual Carbon Nanotubes Using Polarized Photocurrent Spectroscopy. *Nano Lett* **12**, 5649-53, doi:Doi 10.1021/Nl302789k (2012).

15 Balasubramanian, K. *et al.* Photoelectronic transport imaging of individual semiconducting carbon nanotubes. *Appl Phys Lett* **84**, 2400-2 (2004).

16 Balasubramanian, K., Burghard, M., Kern, K., Scolari, M. & Mews, A. Photocurrent imaging of charge transport barriers in carbon nanotube devices. *Nano Lett* **5**, 507-10, doi:10.1021/nl050053k (2005).

17 Freitag, M. *et al.* Imaging of the schottky barriers and charge depletion in carbon nanotube transistors. *Nano Lett* **7**, 2037-42 (2007).

18 Ahn, Y. H., Tsen, A. W., Kim, B., Park, Y. W. & Park, J. Photocurrent imaging of p-n junctions in ambipolar carbon nanotube transistors. *Nano Lett* **7**, 3320-3 (2007).

19 Buchs, G., Barkelid, M., Bagiante, S., Steele, G. A. & Zwiller, V. Imaging the formation of a p-n junction in a suspended carbon nanotube with scanning photocurrent microscopy. *J Appl Phys* **110**, 074308, doi:Doi 10.1063/1.3645022 (2011).

20 Pop, E. *et al.* Negative differential conductance and hot phonons in suspended nanotube molecular wires. *Phys Rev Lett* **95**, 155505, doi:Doi 10.1103/Physrevlett.95.155505 (2005).

21 Hsu, I. K. *et al.* Optical measurement of thermal transport in suspended carbon nanotubes. *Appl Phys Lett* **92**, 063119, doi:Doi 10.1063/1.2829864 (2008).

22 St-Antoine, B. C., Menard, D. & Martel, R. Position Sensitive Photothermoelectric Effect in Suspended Single-Walled Carbon Nanotube Films. *Nano Lett* **9**, 3503-8, doi:Doi 10.1021/Nl901696j (2009).

23 St-Antoine, B. C., Menard, D. & Martel, R. Photothermoelectric effects in single-walled carbon nanotube films: Reinterpreting scanning photocurrent experiments. *Nano Res* **5**, 73-81, doi:DOI 10.1007/s12274-011-0186-x (2012).

24 Sharf, T., Kevek, J. W., DeBorde, T., Wardini, J. L. & Minot, E. D. Origins of Charge Noise in Carbon Nanotube Field-Effect Transistor Biosensors. *Nano Lett* **12**, 6380-4, doi:Doi 10.1021/Nl303651t (2012).

25 DeBorde, T., Kevek, J. W., Sharf, T., Wardini, J. L. & Minot, E. D. in *Nanotechnology (IEEE-NANO), 2011 11th IEEE Conference on.* 382-6.

26 Sharf, T., Kevek, J. W. & Minot, E. D. in *Nanotechnology (IEEE-NANO), 2011 11th IEEE Conference on.* 122-5.

27 Kim, W. *et al.* Electrical contacts to carbon nanotubes down to 1 nm in diameter. *Appl Phys Lett* **87**, 173101, doi:Doi 10.1063/1.2108127 (2005).

28 Dukovic, G. *et al.* Structural dependence of excitonic optical transitions and band-gap energies in carbon nanotubes. *Nano Lett* **5**, 2314-8, doi:Doi 10.1021/Nl058122 (2005).

29 Small, J. P., Perez, K. M. & Kim, P. Modulation of thermoelectric power of individual carbon nanotubes. *Physical Review Letters* **91**, doi:Artn 256801 Doi 10.1103/Physrevlett.91.256801 (2003).

30 Moore, J. P. & Graves, R. S. Absolute Seebeck Coefficient of Platinum from 80 to 340 K and Thermal and Electrical Conductivities of Lead from 80 to 400 K. *J Appl Phys* **44**, 1174-8, doi:Doi 10.1063/1.1662324 (1973).

31 Amer, M. R., Bushmaker, A. & Cronin, S. B. The Influence of Substrate in Determining the Band Gap of Metallic Carbon Nanotubes. *Nano Lett* **12**, 4843-7, doi:Doi 10.1021/Nl302321k (2012).

32 Islam, M. F., Milkie, D. E., Kane, C. L., Yodh, A. G. & Kikkawa, J. M. Direct measurement of the polarized optical absorption cross section of single-wall carbon nanotubes. *Physical Review Letters* **93**, doi:Artn 037404 Doi 10.1103/Physrevlett.93.037404 (2004).

33 Balasubramanian, K., Burghard, M., Kern, K., Scolari, M. & Mews, A. Photocurrent imaging of charge transport barriers in carbon nanotube devices. *Nano Lett* **5**, 507-10 (2005).

34 Li, H. D. *et al.* Temperature dependence of the Raman spectra of single-wall carbon nanotubes. *Appl Phys Lett* **76**, 2053-5, doi:Doi 10.1063/1.126252 (2000).

35 Chiashi, S., Murakami, Y., Miyauchi, Y. & Maruyama, S. Cold wall CVD generation of single-walled carbon nanotubes and in situ Raman scattering measurements of the growth stage. *Chem Phys Lett* **386**, 89-94, doi:DOI 10.1016/j.cplett.2003.12.126 (2004).

36 Joh, D. Y. *et al.* Single-walled carbon nanotubes as excitonic optical wires. *Nat Nanotechnol* **6**, 51-6, doi:Doi 10.1038/Nnano.2010.248 (2011).

37 Pop, E., Mann, D., Wang, Q., Goodson, K. E. & Dai, H. J. Thermal conductance of an individual single-wall carbon nanotube above room temperature. *Nano Lett* **6**, 96-100, doi:Doi 10.1021/Nl052145f (2006).

38 Zhou, X. J., Park, J. Y., Huang, S. M., Liu, J. & McEuen, P. L. Band structure, phonon scattering, and the performance limit of single-walled carbon nanotube transistors. *Phys Rev Lett* **95**, 146805, doi: 10.1103/Physrevlett.95.146805 (2005).

39 Benedict, L. X., Louie, S. G. & Cohen, M. L. Heat capacity of carbon nanotubes. *Solid State Commun* **100**, 177-80, doi:Doi 10.1016/0038-1098(96)00386-9 (1996).

40 Santavicca, D. F., Chudow, J. D., Prober, D. E., Purewal, M. S. & Kim, P. Energy Loss of the Electron System in Individual Single-Walled Carbon Nanotubes. *Nano Lett* **10**, 4538-43, doi:Doi 10.1021/Nl1025002 (2010).

CHAPTER 6

Summary

6.1 General Summary

The key results of this research establish a foundation for optoelectronic research on individual carbon nanotubes (CNTs). This includes the design, construction, and principal operation of a home-built scanning photocurrent microscope; a new method for identifying CNT wall number; a new method for identifying CNT chirality; and the discovery a non-photovoltaic photocurrent generation mechanism in semiconducting CNTs.

The study of CNT optoelectronic properties in this work has been restricted to single-walled CNTs, avoiding more complicated absorption spectra and inter-shell interactions in multi-walled CNTs. Chapter 2 described a novel method to identify single-walled CNTs using atomic force microscopy (AFM). In that work, the high sensitivity of the AFM was used to measure force versus compression for individual CNTs. The height of a fully compressed single- and double-walled CNTs is inherently different and depends on the thickness of single-layer graphene, t. For the two species, single- and double-walled, the final heights should follow approximately with the wall number, $2t$ and $4t$, respectively. From modeling the force dependent compression we were able to extract an estimate of the bending modulus of single-layer graphene. Knowledge of compressed CNT heights has allowed us to tune our growth process for enhancing the percentage of single-walled CNTs.

In chapter 3, the basic operation and initial results of our home-built scanning photocurrent microscopy (SPCM) system are reported. As a test system, we studied both surface-based and suspended CNT FETs. First, the important difference in hysteresis between these two device types is demonstrated in this work. Hysteresis in device conductance as a function of the applied gate voltage is illustrated by taking consecutive SPCM images at a fixed, non-zero gate voltage. A slow drift in the effective gate voltage is revealed as changes in the polarity of the photocurrent as a function of time. These results show that it is impossible to hold a surface-bound device at a specific doping level. In contrast, the effect of hysteresis is significantly reduced in suspended devices due to moving the CNT away from the silicon oxide surface.

The second demonstration of our initial SPCM operation was spectral-resolution of CNT photoconductivity. With the suspended device held in the off state by the stable back gate, the wavelength dependence of the CNT photoresponse can be investigated. With an applied bias, charge carriers created in the CNT from light absorption add to the conductivity of the device. These photoconductivity measurements show peaks at certain wavelengths which correspond to the creation of excitons associated with the different band-to-band transitions in the CNT. The photoconductivity resonances of several devices are discussed in more detail in the subsequent chapter.

The suspended CNT FET device design is an excellent platform for studying the optoelectronics of CNTs. In addition to being free from hysteretic effects, the CNTs in these devices also have pristine lattices as evidenced by the absence of a defect peak in the Raman response. Chapter 4 reports the photoconductivity resonances measured from many suspended devices. Photoconductivity spectrums show two to three strong peaks that are assigned to combinations of the E_{33}, E_{44}, E_{55}, and E_{66} exciton transitions. The presence of additional satellite peaks are ascribed to phonon-sideband peaks. These smaller peaks lie approximately 200 meV above the main peaks, consistent with the energy of optical phonons in the CNT lattice. The strength of the photoresponse on resonance shows a strong dependence on the incident light polarization, with the peak response occurring with the polarization parallel to the CNT axis. The spectral positions of the peaks in photoconductivity can be used to identify the chirality of the CNT by comparing with existing spectral data.

The CNT photoconductivity resonances are most readily measured with the device in the off state. In this configuration the noise in the background “dark current" that scales with conductance is greatly reduced, improving the signal to noise ratio. Additionally, photocurrent that originates from illuminating the contacts is avoided. The source of the extraneous signal from electrode illumination is investigated in the last presented research project.

The source of the observed photocurrent signals at the CNT-metal junction has typically been attributed to photovoltaic effects wherein photoexcited carriers are swept away by built in electric fields. While this picture captures the photoresponse polarity as a function of gate voltage, it does not explain why the signals should extend microns away from the CNT-metal junction. The underlying photothermoelectric (PTE) nature of these long ranged signals is described in chapter 5 in addition to newly observed PTE effects originating within the CNT channel. Laser illumination of the electrodes establishes a temperature gradient across the device driving photovoltages with the same gate dependence as the Seebeck coefficient of large band gap CNTs which Small et al. previously measured. The photocurrent contribution from heating the metal is removed when the device is gated into the off state, consistent with the Seebeck coefficient falling to zero in the band gap. In the on state, PTE effects are present from heating the metal and also from locally heating the suspended CNT channel. The response from locally heating the CNT is isolated by polarization dependent imaging which removes the polarization insensitive contribution from the metal. Finally, from the photothermoelectric effect due to the CNT, the spatial profile of the Seebeck coefficient of the CNT can be estimated up to the resolution of the diffraction limited laser spot.

6.2 Future Work

The accomplishments of this work open the door for the next set of experiments exploring CNT optoelectronic properties to be undertaken by the Minot Group. The immediate next steps will probe how CNT photoconductivity changes with the surrounding dielectric environment. Optical absorption and energy relaxation pathways in CNTs are dependent on strong Coulomb interactions and as a result will depend on the surrounding dielectric environment.

Strong Coulomb interactions lead to exciton creation as the primary result of optical absorption which naturally inhibits photocurrent collection due to the high binding energy of these bound electron-hole pairs. At the same time, strong electron-electron scattering leads to relaxation pathways that can efficiently distribute absorbed energy among charge carriers rather than heating the lattice. Future experiments will coat CNTs in dielectric materials and attempt to determine how the reduction in exciton binding energy affects the collection efficiency of excited charge carriers. Medium term goals include experiments to measure individual CNT absorption coefficients and, combined with photocurrent measurements, the internal quantum efficiency. The final goal of this work is to probe the nature of the carrier multiplication in CNTs and its potential for next-generation solar cells.

In parallel with this work, modifications to the scanning photocurrent microscope will allow spatial modulation spectroscopy measurements of individual CNTs. These measurements can reveal the absolute CNT absorption cross-section which combined with the dielectric dependent photocurrent measurements will allow determination of the quantum efficiency of CNT based optoelectronic devices. Knowledge of the quantum efficiency will allow optimization of the carrier multiplication process through modification of the dielectric coating and pertinent device parameters such as channel length. The long term goals of this project aim to provide critical information for using low-dimensional materials in next generation solar cells and photodetectors.

BIBLIOGRAPHY

Ahn, Yeonghwan, James Dunning, and Jiwoong Park. "Scanning photocurrent imaging and electronic band studies in silicon nanowire field effect transistors." *Nano Letters* **5** (7):1367-70. (2005).

Ahn, Y. H., A. W. Tsen, B. Kim, Y. W. Park, and J. Park. "Photocurrent imaging of p-n junctions in ambipolar carbon nanotube transistors." *Nano Letters* **7** (11):3320-3323. (2007).

Alder, B. J., and R. H. Christian. "Behavior of Strongly Shocked Carbon." *Physical Review Letters* **7** (10):367-369. (1961).

Almaqwashi, Ali A., Joshua W. Kevek, Rachel M. Burton, Tristan DeBorde, and Ethan D. Minot. "Variable-force microscopy for advanced characterization of horizontally aligned carbon nanotubes." *Nanotechnology* **22** (27):275717-275717. (2011).

Amer, M. R., A. Bushmaker, and S. B. Cronin. "The Influence of Substrate in Determining the Band Gap of Metallic Carbon Nanotubes." *Nano Letters* **12** (9):4843-4847. (2012).

Avouris, Phaedon, and Jia Chen. "Nanotube electronics and optoelectronics." *Materials Today* **9** (10):46-54. (2006).

Avouris, P., M. Freitag, and V. Perebeinos. "Carbon-nanotube photonics and optoelectronics." *Nature Photonics* **2** (6):341-350. (2008).

Bachilo, S. M., M. S. Strano, C. Kittrell, R. H. Hauge, R. E. Smalley, and R. B. Weisman. "Structure-assigned optical spectra of single-walled carbon nanotubes." *Science* **298** (5602):2361-2366. (2002).

Baer, R., and E. Rabani. "Can Impact Excitation Explain Efficient Carrier Multiplication in Carbon Nanotube Photodiodes?" *Nano Letters* **10** (9):3277-3282. (2010).

Balasubramanian, Kannan, Marko Burghard, Klaus Kern, Matteo Scolari, and Alf Mews. "Photocurrent imaging of charge transport barriers in carbon nanotube devices." *Nano Letters* **5** (3):507-10. (2005).

Balasubramanian, K., Y. W. Fan, M. Burghard, K. Kern, M. Friedrich, U. Wannek, and A. Mews. "Photoelectronic transport imaging of individual semiconducting carbon nanotubes." *Applied Physics Letters* **84** (13):2400-2402. (2004).

Barkelid, M., G. A. Steele, and V. Zwiller. "Probing Optical Transitions in Individual Carbon Nanotubes Using Polarized Photocurrent Spectroscopy." *Nano Letters* **12** (11):5649-5653. (2012).

Benedict, L. X., S. G. Louie, and M. L. Cohen. "Heat capacity of carbon nanotubes." *Solid State Communications* **100** (3):177-180. (1996).

Berciaud, Stéphane, Christophe Voisin, Hugen Yan, Bhupesh Chandra, Robert Caldwell, Yuyao Shan, Louis E. Brus, James Hone, and Tony F. Heinz. "Excitons and high-order optical transitions in individual carbon nanotubes: A Rayleigh scattering spectroscopy study." *Physical Review B* **81** (4):041414-041414. (2010).

Blancon, Jean-Christophe, Matthieu Paillet, Huy Nam Tran, Xuan Tinh Than, Samuel Aberra Guebrou, Anthony Ayari, Alfonso San Miguel, Ngoc-Minh Phan, Ahmed-Azmi Zahab, Jean-Louis Sauvajol, Natalia Del Fatti, and Fabrice Vallée. "Direct measurement of the absolute absorption spectrum of individual semiconducting single-wall carbon nanotubes." *Nature communications* **4**:2542-2542. (2013).

Buchs, G., M. Barkelid, S. Bagiante, G. A. Steele, and V. Zwiller. "Imaging the formation of a p-n junction in a suspended carbon nanotube with scanning photocurrent microscopy." *Journal of Applied Physics* **110** (7):074308. (2011).

Buscema, M., M. Barkelid, V. Zwiller, H. S. J. van der Zant, G. A. Steele, and A. Castellanos-Gomez. "Large and Tunable Photothermoelectric Effect in Single-Layer MoS2." *Nano Letters* **13** (2):358-363. (2013).

Charlier, J. C. Eklund P. C. Zhu J. Ferrari A. C. *Carbon Nanotubes*. Vol. 111, *Topics in Applied Physics*. Berlin, Heidelberg: Springer Berlin Heidelberg. (2008).

Chen, J., V. Perebeinos, M. Freitag, J. Tsang, Q. Fu, J. Liu, and P. Avouris. "Bright infrared emission from electrically induced excitons in carbon nanotubes." *Science* **310** (5751):1171-1174. (2005).

Chiashi, S., Y. Murakami, Y. Miyauchi, and S. Maruyama. "Cold wall CVD generation of single-walled carbon nanotubes and in situ Raman scattering measurements of the growth stage." *Chemical Physics Letters* **386** (1-3):89-94. (2004).

Choi, S., J. Deslippe, R. B. Capaz, and S. G. Louie. "An Explicit Formula for Optical Oscillator Strength of Excitons in Semiconducting Single-Walled Carbon Nanotubes: Family Behavior." *Nano Letters* **13** (1):54-58. (2013).

Cleveland, J. P., B. Anczykowski, A. E. Schmid, and V. B. Elings. "Energy dissipation in tapping-mode atomic force microscopy." *Applied Physics Letters* **72** (20):2613-2613. (1998).

Cutler, M., and N. F. Mott. "Observation of Anderson Localization in an Electron Gas." *Physical Review* **181** (3):1336-&. (1969).

DeBorde, Tristan, Lee Aspitarte, Tal Sharf, Joshua W. Kevek, and Ethan D. Minot. "Photothermoelectric Effect in Suspended Semiconducting Carbon Nanotubes." *ACS Nano*. (2013).

DeBorde, T., J. W. Kevek, T. Sharf, J. L. Wardini, and Ethan D. Minot. 2011. A spectrally-tunable photocurrent microscope for characterizing nanoelectronic devices. Paper read at Nanotechnology (IEEE-NANO), 2011 11th IEEE Conference on, 15-18 Aug. 2011.

Dukovic, G., F. Wang, D. H. Song, M. Y. Sfeir, T. F. Heinz, and L. E. Brus. "Structural dependence of excitonic optical transitions and band-gap energies in carbon nanotubes." *Nano Letters* **5** (11):2314-2318. (2005).

Fraxedas, J., G. Rius, F. Pérez-Murano, and A. Verdaguer. "Determining radial breathing mode frequencies of single-walled carbon nanotubes with an atomic force microscope." *Europhysics Letters (EPL)* **78** (1):16001-16001. (2007).

Freitag, M., T. Low, and P. Avouris. "Increased Responsivity of Suspended Graphene Photodetectors." *Nano Letters* **13** (4):1644-1648. (2013).

Freitag, M., Y. Martin, J. A. Misewich, R. Martel, and P. H. Avouris. "Photoconductivity of single carbon nanotubes." *Nano Letters* **3** (8):1067-1071. (2003).

Freitag, M., J. C. Tsang, A. Bol, P. Avouris, D. N. Yuan, and J. Liu. "Scanning photovoltage microscopy of potential modulations in carbon nanotubes." *Applied Physics Letters* **91** (3). (2007).

Freitag, M., J. C. Tsang, A. Bol, D. N. Yuan, J. Liu, and P. Avouris. "Imaging of the schottky barriers and charge depletion in carbon nanotube transistors." *Nano Letters* **7** (7):2037-2042. (2007).

Gabor, N. M. "Impact Excitation and Electron-Hole Multiplication in Graphene and Carbon Nanotubes." *Acc Chem Res* **46** (6):1348-1357. (2013).

Gabor, Nathaniel M., Justin C. W. Song, Qiong Ma, Nityan L. Nair, Thiti Taychatanapat, Kenji Watanabe, Takashi Taniguchi, Leonid S. Levitov, and Pablo Jarillo-Herrero. "Hot carrier-assisted intrinsic photoresponse in graphene." *Science (New York, N.Y.)* **334** (6056):648-52. (2011).

Gabor, Nathaniel M., Zhaohui Zhong, Ken Bosnick, Jiwoong Park, and Paul L. McEuen. "Extremely efficient multiple electron-hole pair generation in carbon nanotube photodiodes." *Science (New York, N.Y.)* **325** (5946):1367-71. (2009).

Hertel, Tobias, Vasili Perebeinos, Jared Crochet, Katharina Arnold, Manfred Kappes, and Phaedon Avouris. "Intersubband decay of 1-D exciton resonances in carbon nanotubes." *Nano Letters* **8** (1):87-91. (2008).

Hsu, I. K., R. Kumar, A. Bushmaker, S. B. Cronin, M. T. Pettes, L. Shi, T. Brintlinger, M. S. Fuhrer, and J. Cumings. "Optical measurement of thermal transport in suspended carbon nanotubes." *Applied Physics Letters* **92** (6):063119. (2008).

Hutter, Jeffrey L., and John Bechhoefer. "Calibration of atomic-force microscope tips." *Review of Scientific Instruments* **64** (7):1868-1868. (1993).

Islam, M. F., D. E. Milkie, C. L. Kane, A. G. Yodh, and J. M. Kikkawa. "Direct measurement of the polarized optical absorption cross section of single-wall carbon nanotubes." *Physical Review Letters* **93** (3). (2004).

Joh, Daniel Y., Lihong H. Herman, Sang-Yong Ju, Jesse Kinder, Michael a Segal, Jeffreys N. Johnson, Garnet K. L. Chan, and Jiwoong Park. "On-chip Rayleigh imaging and spectroscopy of carbon nanotubes." *Nano Letters* **11** (1):1-7. (2011).

Joh, D. Y., J. Kinder, L. H. Herman, S. Y. Ju, M. A. Segal, J. N. Johnson, G. K. L. Chan, and J. Park. "Single-walled carbon nanotubes as excitonic optical wires." *Nature Nanotechnology* **6** (1):51-56. (2011).

Jorio, a, R. Saito, J. Hafner, C. Lieber, M. Hunter, T. McClure, G. Dresselhaus, and M. Dresselhaus. "Structural (n, m) Determination of Isolated Single-Wall Carbon Nanotubes by Resonant Raman Scattering." *Physical Review Letters* **86** (6):1118-1121. (2001).

Kataura, H., Y. Kumazawa, Y. Maniwa, I. Umezu, S. Suzuki, Y. Ohtsuka, and Y. Achiba. "Optical properties of single-wall carbon nanotubes." *Synthetic Metals* **103** (1):2555-2558. (1999).

Kiang, C. H., M. Endo, P. Ajayan, G. Dresselhaus, and M. Dresselhaus. "Size Effects in Carbon Nanotubes." *Physical Review Letters* **81** (9):1869-1872. (1998).

Kim, W., A. Javey, R. Tu, J. Cao, Q. Wang, and H. J. Dai. "Electrical contacts to carbon nanotubes down to 1 nm in diameter." *Applied Physics Letters* **87** (17):173101. (2005).

Kim, W., A. Javey, O. Vermesh, O. Wang, Y. M. Li, and H. J. Dai. "Hysteresis caused by water molecules in carbon nanotube field-effect transistors." *Nano Letters* **3** (2):193-198. (2003).

Kong, Jing, Hyongsok T. Soh, Alan M. Cassell, Calvin F. Quate, and Hongjie Dai. "Synthesis of individual single-walled carbon nanotubes on patterned silicon wafers." *Nature* **395**:1-4. (1998).

Kong, J., B. J. LeRoy, S. G. Lemay, and C. Dekker. "Integration of a gate electrode into carbon nanotube devices for scanning tunneling microscopy." *Applied Physics Letters* **86** (11):112106. (2005).

Kumamoto, Y., M. Yoshida, A. Ishii, A. Yokoyama, T. Shimada, and Y. K. Kato. "Spontaneous exciton dissociation in carbon nanotubes." (2013).

Lee, J. S., S. Ryu, K. Yoo, I. S. Choi, W. S. Yun, and J. Kim. "Origin of gate hysteresis in carbon nanotube field-effect transistors." *Journal of Physical Chemistry C* **111** (34):12504-12507. (2007).

Lee, J. U. "Band-gap renormalization in carbon nanotubes: Origin of the ideal diode behavior in carbon nanotube p-n structures." *Physical Review B* **75** (7):-. (2007).

Lee, J. U., P. J. Codella, and M. Pietrzykowski. "Direct probe of excitonic and continuum transitions in the photocurrent spectroscopy of individual carbon nanotube p-n diodes." *Applied Physics Letters* **90** (5):053103. (2007).

Lefebvre, J., Y. Homma, and P. Finnie. "Bright Band Gap Photoluminescence from Unprocessed Single-Walled Carbon Nanotubes." *Physical Review Letters* **90** (21):217401-217401. (2003).

Li, H. D., K. T. Yue, Z. L. Lian, Y. Zhan, L. X. Zhou, S. L. Zhang, Z. J. Shi, Z. N. Gu, B. B. Liu, R. S. Yang, H. B. Yang, G. T. Zou, Y. Zhang, and S. Iijima. "Temperature dependence of the Raman spectra of single-wall carbon nanotubes." *Applied Physics Letters* **76** (15):2053-2055. (2000).

Liu, Kaihui, Jack Deslippe, Fajun Xiao, Rodrigo B. Capaz, Xiaoping Hong, Shaul Aloni, Alex Zettl, Wenlong Wang, Xuedong Bai, Steven G. Louie, Enge Wang, and Feng Wang. "An atlas of carbon nanotube optical transitions." *Nature nanotechnology* **7** (5):325-9. (2012).

Liu, Kaihui, Xiaoping Hong, Qin Zhou, Chenhao Jin, Jinghua Li, Weiwei Zhou, Jie Liu, Enge Wang, Alex Zettl, and Feng Wang. "High-throughput optical imaging and spectroscopy of individual carbon nanotubes in devices." *Nature nanotechnology* **8** (12):917-22. (2013).

Ma, Ying-Zhong, Jens Stenger, Jorg Zimmermann, Sergei M. Bachilo, Richard E. Smalley, R. Bruce Weisman, and Graham R. Fleming. "Ultrafast carrier dynamics in single-walled carbon nanotubes probed by femtosecond spectroscopy." *The Journal of chemical physics* **120** (7):3368-73. (2004).

MacDonald, D. K. C. *Thermoelectricity: an introduction to the principles*. New York,: Wiley. (1962).

Malapanis, Argyrios, Vasili Perebeinos, Dhiraj Prasad Sinha, Everett Comfort, and Ji Ung Lee. "Quantum efficiency and capture cross section of first and second excitonic transitions of single-walled carbon nanotubes measured through photoconductivity." *Nano Letters* **13** (8):3531-8. (2013).

Manzoni, C., a Gambetta, E. Menna, M. Meneghetti, G. Lanzani, and G. Cerullo. "Intersubband Exciton Relaxation Dynamics in Single-Walled Carbon Nanotubes." *Physical Review Letters* **94** (20):207401-207401. (2005).

McEuen, P. L., and M. S. Fuhrer. "Single-walled carbon nanotube electronics." *IEEE Transactions On Nanotechnology* **1** (1):78-85. (2002).

Meyer, Jannik, Matthieu Paillet, Thierry Michel, Alain Moréac, Anita Neumann, Georg Duesberg, Siegmar Roth, and Jean-Louis Sauvajol. "Raman Modes of Index-Identified Freestanding Single-Walled Carbon Nanotubes." *Physical Review Letters* **95** (21):217401-217401. (2005).

Misewich, J. A., R. Martel, P. Avouris, J. C. Tsang, S. Heinze, and J. Tersoff. "Electrically induced optical emission from a carbon nanotube FET." *Science* **300** (5620):783-786. (2003).

Mohite, A., J. T. Lin, G. Sumanasekera, and B. W. Alphenaar. "Field-enhanced photocurrent spectroscopy of excitonic states in single-wall carbon nanotubes." *Nano Letters* **6** (7):1369-1373. (2006).

Moore, J. P., and R. S. Graves. "Absolute Seebeck Coefficient of Platinum from 80 to 340 K and Thermal and Electrical Conductivities of Lead from 80 to 400 K." *Journal of Applied Physics* **44** (3):1174-1178. (1973).

Mueller, T., F. N. A. Xia, and P. Avouris. "Graphene photodetectors for high-speed optical communications." *Nature Photonics* **4** (5):297-301. (2010).

Muoth, M., T. Helbling, L. Durrer, S. W. Lee, C. Roman, and C. Hierold. "Hysteresis-free operation of suspended carbon nanotube transistors." *Nature Nanotechnology* **5** (8):589-592. (2010).

Ohno, Yutaka, Shinya Iwasaki, Yoichi Murakami, Shigeru Kishimoto, Shigeo Maruyama, and Takashi Mizutani. "Excitonic transition energies in single-walled carbon nanotubes: Dependence on environmental dielectric constant." *Physica Status Solidi (B)* **244** (11):4002-4005. (2007).

Oliver, W. C., and G. M. Pharr. "Measurement of hardness and elastic modulus by instrumented indentation: Advances in understanding and refinements to methodology." *Journal of Materials Research* **19** (1):3-20. (2004).

Palaci, I., S. Fedrigo, H. Brune, C. Klinke, M. Chen, and E. Riedo. "Radial elasticity of multiwalled carbon nanotubes." *Physical Review Letters* **94**:175502-175502. (2005).

Park, Jiwoong, Y. H. Ahn, and Carlos Ruiz-Vargas. "Imaging of photocurrent generation and collection in single-layer graphene." *Nano Letters* **9** (5):1742-6. (2009).

Pedrotti, Frank L., and Leno S. Pedrotti. *Introduction to optics*. 2nd ed. Englewood Cliffs, N.J.: Prentice Hall. (1993).

Perebeinos, V., and P. Avouris. "Impact excitation by hot carriers in carbon nanotubes." *Physical Review B* **74** (12). (2006).

Perebeinos, V., J. Tersoff, and P. Avouris. "Scaling of excitons in carbon nanotubes." *Physical Review Letters* **92** (25). (2004).

Perebeinos, Vasili, J. Tersoff, and Phaedon Avouris. "Effect of Exciton-Phonon Coupling in the Calculated Optical Absorption of Carbon Nanotubes." *Physical Review Letters* **94** (2):027402-027402. (2005).

Pop, E., D. Mann, J. Cao, Q. Wang, K. E. Goodson, and H. J. Dai. "Negative differential conductance and hot phonons in suspended nanotube molecular wires." *Physical Review Letters* **95** (15):155505. (2005).

Pop, E., D. Mann, Q. Wang, K. E. Goodson, and H. J. Dai. "Thermal conductance of an individual single-wall carbon nanotube above room temperature." *Nano Letters* **6** (1):96-100. (2006).

Postma, H. W. C., A. Sellmeijer, and C. Dekker. "Manipulation and Imaging of Individual Single-Walled Carbon Nanotubes with an Atomic Force Microscope." *Advanced Materials* **12**:1299-1302. (2000).

Prisbrey, Landon, Tristan DeBorde, Ji Park, Yong, and Ethan D. Minot. "Controlling the Function of Carbon Nanotube Devices with Re-writable Charge Patterns." *Applied Physics Letters* **99**. (2011).

Qian, Dong, Gregory J. Wagner, Wing Kam Liu, Min-Feng Yu, and Rodney S. Ruoff. "Mechanics of carbon nanotubes." *Applied Mechanics Reviews* **55**:495-495. (2002).

Qiu, X. H., M. Freitag, V. Perebeinos, and P. Avouris. "Photoconductivity spectra of single-carbon nanotubes: Implications on the nature of their excited states." *Nano Letters* **5** (4):749-752. (2005).

Robertson, D., D. Brenner, and J. Mintmire. "Energetics of nanoscale graphitic tubules." *Physical Review B* **45** (21):12592-12595. (1992).

Saito, Riichiro, Gene Dresselhaus, and Mildred Dresselahus. *Physical Properties of Carbon Nanotubes*. (1998).

Saito, R., M. Fujita, G. Dresselhaus, and M. S. Dresselhaus. "Electronic structure of chiral graphene tubules." *Applied Physics Letters* **60** (18):2204-2204. (1992).

Samsonidze, Ge G., a R. Saito, D. a Jorio, E. M. a Pimenta, E. a G. Souza Filho, F. a Grüneis, D. G. Dresselhaus, and M. S. Dresselhausa. "The Concept of Cutting Lines in Carbon Nanotube Science." *Journal of Nanoscience and Nanotechnology* **3** (6):431-458. (2003).

Santavicca, D. F., J. D. Chudow, D. E. Prober, M. S. Purewal, and P. Kim. "Energy Loss of the Electron System in Individual Single-Walled Carbon Nanotubes." *Nano Letters* **10** (11):4538-4543. (2010).

Schaller, R., and V. Klimov. "High Efficiency Carrier Multiplication in PbSe Nanocrystals: Implications for Solar Energy Conversion." *Physical Review Letters* **92** (18):186601-186601. (2004).

Sfeir, Matthew Y., Feng Wang, Limin Huang, Chia-Chin Chuang, J. Hone, Stephen P. O'Brien, Tony F. Heinz, and Louis E. Brus. "Probing electronic transitions in individual carbon nanotubes by Rayleigh scattering." *Science (New York, N.Y.)* **306** (5701):1540-3. (2004).

Sharf, T., J. W. Kevek, T. DeBorde, J. L. Wardini, and E. D. Minot. "Origins of Charge Noise in Carbon Nanotube Field-Effect Transistor Biosensors." *Nano Letters* **12** (12):6380-6384. (2012).

Sharf, T., J. W. Kevek, and Ethan D. Minot. 2011. Fabrication of low-noise carbon nanotube field-effect transistor biosensors. Paper read at Nanotechnology (IEEE-NANO), 2011 11th IEEE Conference on, 15-18 Aug. 2011.

Shen, Weidian, Bin Jiang, Bao Han, and Si-shen Xie. "Investigation of the Radial Compression of Carbon Nanotubes with a Scanning Probe Microscope." *Physical Review Letters* **84** (16):3634-3637. (2000).

Shockley, William, and Hans J. Queisser. "Detailed Balance Limit of Efficiency of p-n Junction Solar Cells." *Journal of Applied Physics* **32** (3):510-510. (1961).

Small, J. P., K. M. Perez, and P. Kim. "Modulation of thermoelectric power of individual carbon nanotubes." *Physical Review Letters* **91** (25). (2003).

St-Antoine, B. C., D. Menard, and R. Martel. "Position Sensitive Photothermoelectric Effect in Suspended Single-Walled Carbon Nanotube Films." *Nano Letters* **9** (10):3503-3508. (2009).

Repeated Author. "Photothermoelectric effects in single-walled carbon nanotube films: Reinterpreting scanning photocurrent experiments." *Nano Research* **5** (2):73-81. (2012).

Tielrooij, K. J., J. C. W. Song, S. a Jensen, a Centeno, a Pesquera, a Zurutuza Elorza, M. Bonn, L. S. Levitov, and F. H. L. Koppens. "Photoexcitation cascade and multiple hot-carrier generation in graphene." *Nature Physics* **9** (4):248-252. (2013).

Verdenhalven, Eike, and Ermin Malić. "Excitonic absorption intensity of semiconducting and metallic carbon nanotubes." *Journal of physics. Condensed matter : an Institute of Physics journal* **25** (24):245302-245302. (2013).

Wallace, P. "The Band Theory of Graphite." *Physical Review* **71** (9):622-634. (1947).

Wang, Feng, Gordana Dukovic, Louis E. Brus, and Tony F. Heinz. "The optical resonances in carbon nanotubes arise from excitons." *Science (New York, N.Y.)* **308** (5723):838-841. (2005).

Wang, Hui-Yao, M. Zhao, and Scott X. Mao. "Radial moduli of individual single-walled carbon nanotubes with and without electric current flow." *Applied Physics Letters* **89** (21):211906-211906. (2006).

Wilder, Jeroen W. G., Liesbeth C. Venema, Andrew G. Rinzler, Richard E. Smalley, and Cees Dekker. "Electronic structure of atomically resolved carbon nanotubes." **391** (6662):59-62. (1998).

Xia, F. N., T. Mueller, R. Golizadeh-Mojarad, M. Freitag, Y. M. Lin, J. Tsang, V. Perebeinos, and P. Avouris. "Photocurrent Imaging and Efficient Photon Detection in a Graphene Transistor." *Nano Letters* **9** (3):1039-1044. (2009).

Xia, F. N., T. Mueller, Y. M. Lin, A. Valdes-Garcia, and P. Avouris. "Ultrafast graphene photodetector." *Nature Nanotechnology* **4** (12):839-843. (2009).

Xu, X. D., N. M. Gabor, J. S. Alden, A. M. van der Zande, and P. L. McEuen. "Photo-Thermoelectric Effect at a Graphene Interface Junction." *Nano Letters* **10** (2):562-566. (2010).

Yu, Min-Feng, Tomasz Kowalewski, and Rodney Ruoff. "Investigation of the Radial Deformability of Individual Carbon Nanotubes under Controlled Indentation Force." *Physical Review Letters* **85** (7):1456-1459. (2000).

Zhou, X. J., J. Y. Park, S. M. Huang, J. Liu, and P. L. McEuen. "Band structure, phonon scattering, and the performance limit of single-walled carbon nanotube transistors." *Physical Review Letters* **95** (14):146805. (2005).

Zuev, Y. M., W. Chang, and P. Kim. "Thermoelectric and Magnetothermoelectric Transport Measurements of Graphene." *Physical Review Letters* **102** (9):096807. (2009).

APPENDICES

Appendix A. Confocal Lens Pair for Scanning Microscopy

Raster scanning the focused laser spot in this work is accomplished with a pair of scan mirrors as opposed to using an x-y stage to move the sample across a fixed laser spot. The configuration where collimated laser light is sent directly from the scanning mirrors to the objective will suffer from a small scan area and inconsistent laser intensity. To achieve a large scan area and consistent incident intensity, two lenses are used to maintain the incident beam on the entrance of the objective.

Figure A.1 shows a schematic of the confocal lens pair in the scanning photocurrent microscope used in this research. The lens pair is positioned with overlapping focal planes and additionally the focal plane of Lens 1 is positioned with the point where the laser leaves the scan mirrors. The focal plane of Lens 2 overlaps with the entrance optic of the objective. If the focal lengths, *f*, of the lenses are unequal, the diameter, *d*, of the collimated laser beam will change. Focal lengths are chosen to ensure the back of the objective is slightly overfilled. The size of the final beam diameter, d_f, is related to the initial diameter, d_i, by the ratio of the focal lengths of the lens pair,

$$d_f = d_i \frac{f_2}{f_1}. \quad \text{(A1)}$$

With a properly aligned lens pair, raster scanned images can easily image typical source-drain electrode device geometries (~30 x 30 μm).

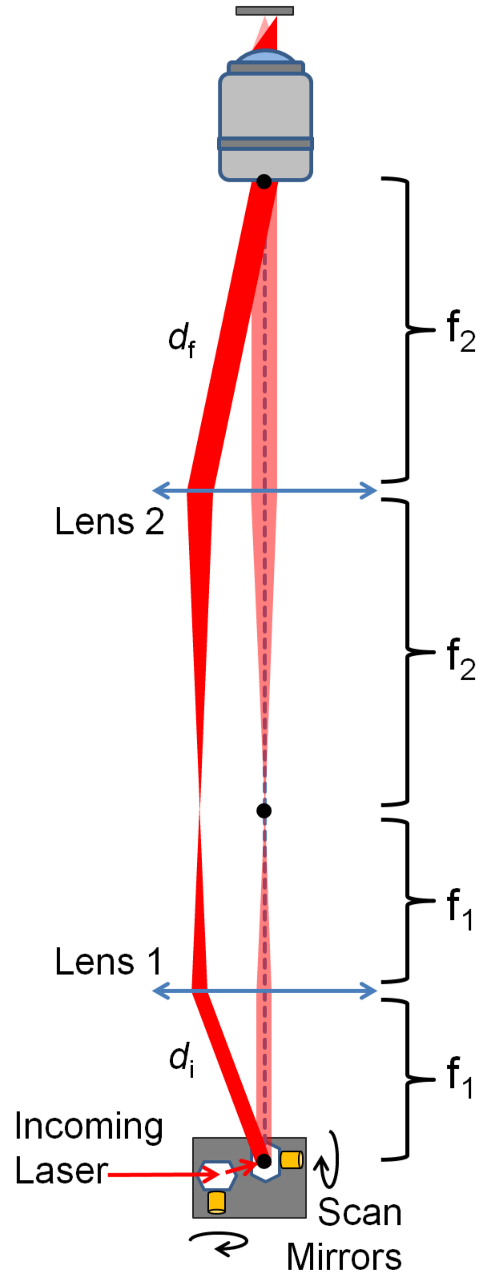

Figure A.1. Confocal lens pair. Schematic of lens pair used to maintain laser spot on objective entrance. The lens pair can also be used to change the size of the incident laser beam if $f_1 \neq f_2$.

Appendix B. Estimating Laser Spot from Reflection Image

The size of the focused laser spot is a critical factor in scanning photocurrent microscopy (SPCM). Data from the reflection images can be used to estimate the laser spot size in conjunction with an electrode feature of known size, e.g. the source-drain electrode separation, w_{sd}. Figure B.1 shows a schematic diagram the laser incident on the electrode edge and the corresponding reflection signal when the laser spot is raster scanned across the electrode geometry.

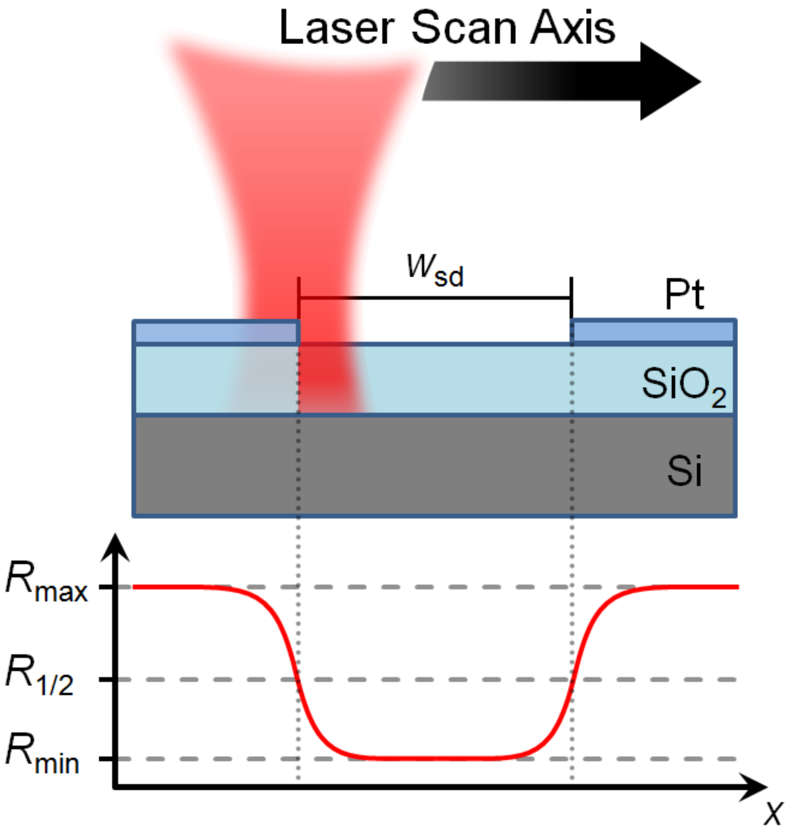

Figure B.1. Reflection schematic and image cross-section. Top panel shows the geometry of the incident focused laser spot on an electrode edge. Bottom panel shows a sketch of the corresponding reflection signal from raster scanning the laser across a source-drain electrode gap of width w_{sd}. Reflection signal graph shows max (min) values corresponding to the laser spot completely on (off) the electrode. $R_{\min}$ will be non-zero due to reflection from the silicon substrate. When a symmetric laser spot is centered on an electrode edge the reflection signal, $R_{1/2}$, will be 50% of $R_{\max}$-$R_{\min}$.

Assuming the laser beam intensity has a two-dimensional Gaussian profile, the full-width at half-maximum (fwhm) of the laser spot can be extracted from the reflection signal. To calibrate the size scale, the known distance w_{sd} is equal to the separation between the two $R_{1/2}$ points. Using this comparison, the image can be scaled from pixels to nm.

The fwhm of a 1d Gaussian is related to the standard deviation, σ, by,

$$fwhm = 2\sqrt{2\ln 2}\sigma . \quad \text{(B1)}$$

The reflection signal in Figure B.1 corresponds to the integration of the Gaussian laser profile in one dimension. For a normal distribution the area percentage enclosed by the fwhm is approximately 76%. Applied to the reflection cross-section, the fwhm of the laser spot is the distance between the points where the reflection signal is,

$$R(-x_{fwhm}) = 0.12(R_{\max} - R_{\min}) + R_{\min}, \ \& \quad \text{(B2.a)}$$

$$R(x_{fwhm}) = 0.88(R_{\max} - R_{\min}) + R_{\min}. \quad \text{(B2.b)}$$

The x-distance between the positions that satisfy equations B2.a and B2.b is equal to the fwhm of the laser spot.

Appendix C. Tunable Laser Source

The spectrally resolved measurements presented in this dissertation were achieved through the combination of a supercontinuum laser and a spectrometer acting as a bandpass filter. The laser source is a Fianium SC450-4 supercontinuum laser with a total power of 4 W which due to a nonlinear fiber, is spread across a large wavelength range (0.45 – 1.8 μm). The spectrometer is a

Czerny-Turner monochromator (Horiba, HR Micro) with a diffraction grating blazed at 500 nm and having 600 grooves/mm.

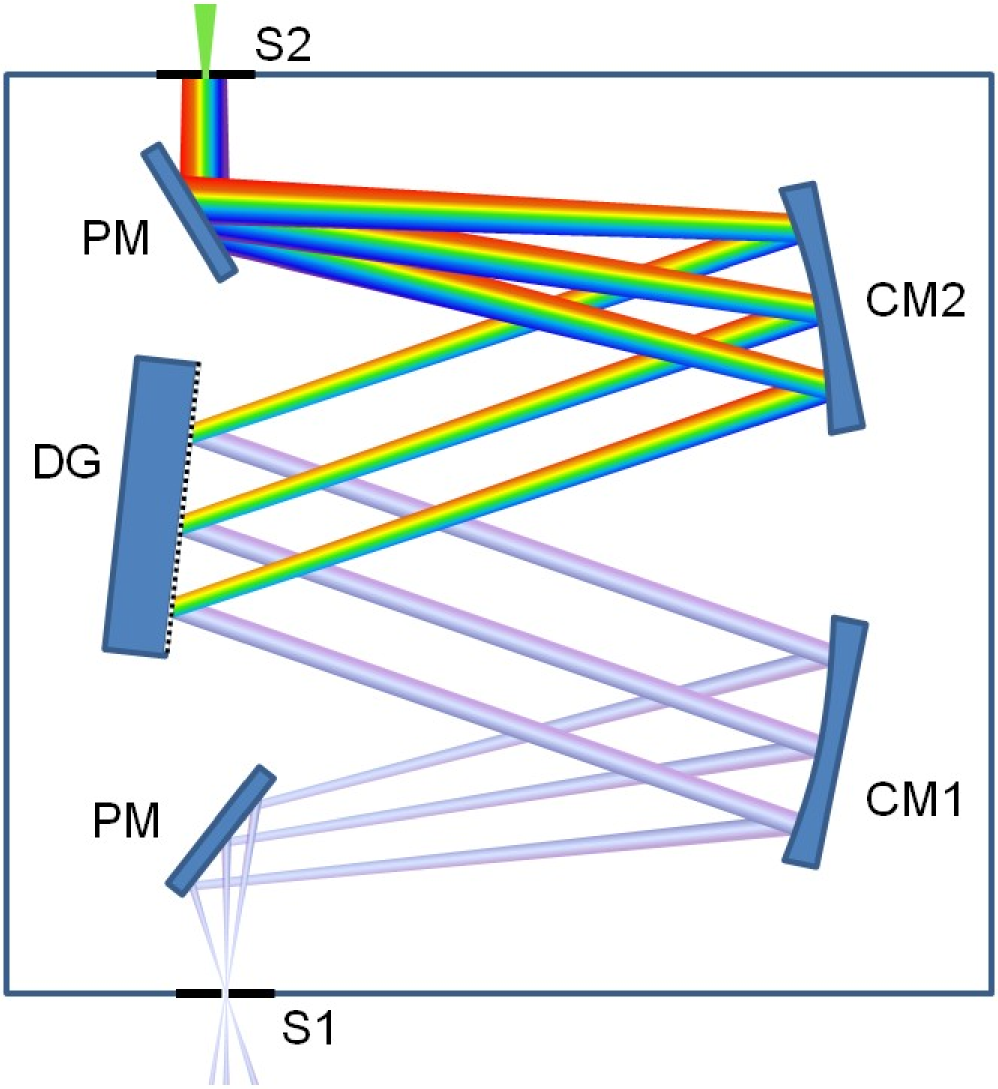

Figure C.1. Monochromator schematic. Incident supercontinuum laser light is initially focused on the entrance slit (S1). A plane mirror (PM) then directs light to the first curved mirror (CM1) which collimates light onto the diffraction grating (DG). The light is dispersed toward CM2 which refocuses light onto the exit slit (S2) only allowing a small wavelength bandwidth to exit.

Figure C.1 shows a schematic of a Czerny-Turner monochromator. Incident supercontinuum laser light is focused on the entrance slit (S1) and then directed to a curved mirror (CM1) via a plane mirror (PM). The focal length of the monochromator, *f*, is the optical path distance between S1 and CM1 (identical for CM2 and S2). Collimated light from CM1 is dispersed by the diffraction grating (DG) toward a second curved mirror that focuses the light on the exit slit (S2). The wavelength bandwidth leaving the system is controlled by the exit slit and depends on the linear dispersion of the monochromator.

The linear dispersion of the monochromator can be derived beginning with the grating equation,[1]

$$a(\sin\theta_i + \sin\theta_m) = m\lambda, \qquad \text{(C1)}$$

where a is the separation between grooves, θ_i and θ_m are the incident and diffracted ray angles, respectively, λ is the wavelength, and $m = 0, \pm1, \pm2, \dots$ is the diffraction order. The angular dispersion, D, of the grating is given by,

$$D = \frac{d\theta_m}{d\lambda} = \frac{a}{m\cos\theta_m}, \text{(C2)}$$

where the right hand side of eq. C2 is found from eq. C1. The linear dispersion, L, is found by combining the focal length of the monochromator and eq. C2.

$$L = fD. \qquad \text{(C3)}$$

An additional concern when using a monochromator is free spectral range. The output light from the monochromator is from the m = 1 diffraction order. From range of wavelengths input into the monochromator there will be a wavelength where the next higher order begins to overlap with the selected first order wavelength. To remove undesired wavelengths from higher orders additional filtering must be used. The free spectral range, F, can be calculated using,

$$F = \lambda_2 - \lambda_1 = \frac{\lambda_1}{m}, \qquad \text{(C4)}$$

where λ_1 is the shortest input wavelength and λ_2 is the longest output wavelength not overlapped by additional orders.

Appendix D. Electrode Photoresponse

In chapters 4 and 5, the polarization and wavelength dependence of the photoresponse when illuminating an individual carbon nanotube is investigated. However the same dependencies of the photoresponse when illuminating just the metal electrodes were not directly shown. Figure D.1a shows the wavelength dependent photoresponse while illuminating just the source electrode (Pt) of a CNT FET device. Figure D.1b shows the photoresponse as a function of the incident polarization angle. The measurement shows the metal has only little dependence in our wavelength range and no effective polarization dependence.

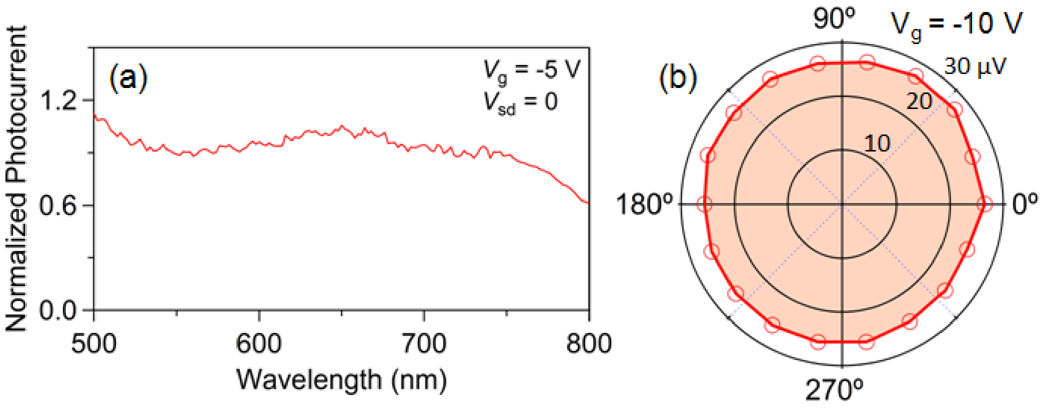

Figure D.1. CNT FET electrode photoresponse. (a) Wavelength dependence of photocurrent measured while illuminating the source electrode of a CNT FET device. (b) Photovoltage response measured while rotating the polarization of light (633 nm) incident on the same source electrode. Both measurements were taking while the device was in the off state.

Appendix E. Seebeck Coefficient: Mott Formula

Thermoelectric measurements of the Seebeck coefficient, S, for quasi-metallic CNTs[2] and graphene[3] have found good agreement with the Seebeck coefficient predicted by the Mott formula,[4]

$$S_{\mathrm{Mott}} = -\frac{\pi^2 k_B^2 T}{3|e|} \frac{1}{G} \frac{dG}{dV_g} \frac{dV_g}{dE}\bigg|_{E=E_F}, \qquad \text{(E1)}$$

where k_{B} is the Boltzmann constant, e is the electronic charge, T is the temperature, G is the conductance, V_{g} is the gate voltage, and E_{F} is the Fermi energy. Scanning photocurrent microscopy experiments on graphene based devices have also produced results well explained by the Mott formula.[5,6]

However, for large band gap CNTs, the Mott formula fails to predict the measured behavior.[2,7] This disagreement is not unexpected as eq. E1 requires the conductivity to not vary significantly near E_{F}.[8] Figure E.1 shows a comparison between the measured Seebeck coefficient (V_{oc} with ΔT = 1K) and the result of eq. E1 using the device conductance. The predicted Seebeck coefficient from the Mott formula is strikingly different from experiment and clearly fails to capture the measured dependence on V_{g}.

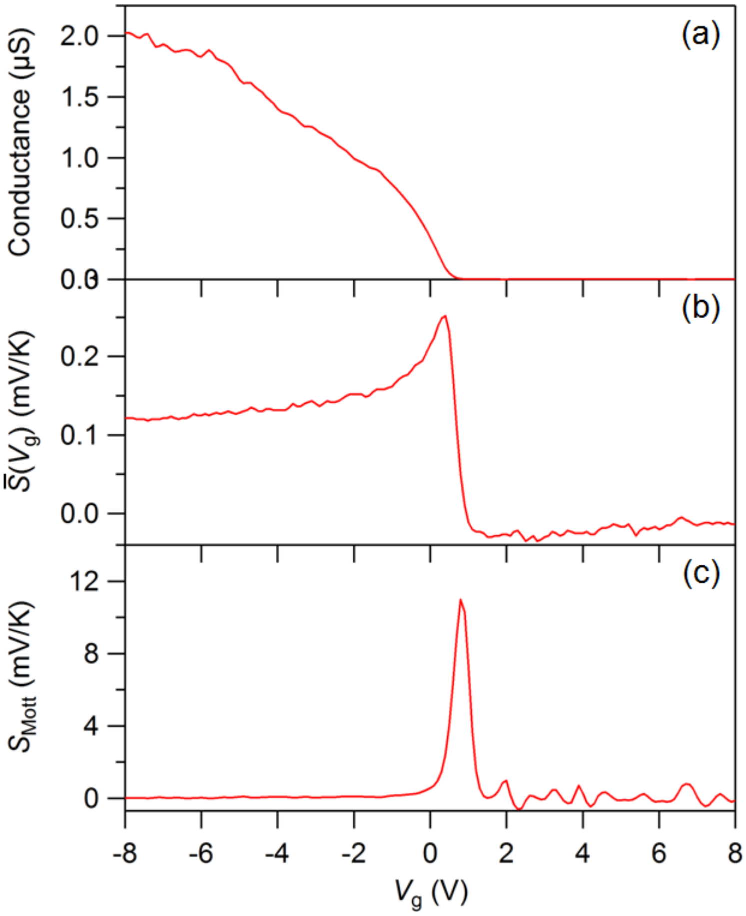

Figure E.1. CNT Seebeck coefficient. (a) Measured conductance of a large gap CNT FET device (b) Seebeck coefficient of the device in (a). Values of S are obtained from an open-circuit voltage measurement taken with a predicted $\Delta T = 1$ K. (c) Result of the Mott formula using the device conductance in (a) and a estimated gate coupling factor of ~ 0.05.

References

1 Pedrotti, F. L. & Pedrotti, L. S. *Introduction to optics*. 2nd edn, (Prentice Hall, 1993).

2 Small, J. P., Perez, K. M. & Kim, P. Modulation of thermoelectric power of individual carbon nanotubes. *Physical Review Letters* **91**, doi:Artn 256801 Doi 10.1103/Physrevlett.91.256801 (2003).

3 Zuev, Y. M., Chang, W. & Kim, P. Thermoelectric and Magnetothermoelectric Transport Measurements of Graphene. *Phys Rev Lett* **102**, 096807, doi:10.1103/Physrevlett.102.096807 (2009).

4 Cutler, M. & Mott, N. F. Observation of Anderson Localization in an Electron Gas. *Phys Rev* **181**, 1336-&, doi:DOI 10.1103/PhysRev.181.1336 (1969).

5 Xu, X. D., Gabor, N. M., Alden, J. S., van der Zande, A. M. & McEuen, P. L. Photo-Thermoelectric Effect at a Graphene Interface Junction. *Nano Lett* **10**, 562-6, doi:Doi 10.1021/Nl903451y (2010).

6 Gabor, N. M. *et al.* Hot carrier-assisted intrinsic photoresponse in graphene. *Science (New York, N.Y.)* **334**, 648-52, doi:10.1126/science.1211384 (2011).

7 DeBorde, T., Aspitarte, L., Sharf, T., Kevek, J. W. & Minot, E. D. Photothermoelectric Effect in Suspended Semiconducting Carbon Nanotubes. *ACS Nano*, doi:10.1021/nn403137a (2013).

8 MacDonald, D. K. C. *Thermoelectricity: an introduction to the principles*. (Wiley, 1962).